

ABSTRACT

Title of dissertation: EXTENSIONS OF THE KURAMOTO
MODEL: FROM SPIKING NEURONS
TO SWARMING DRONES

Sarthak Chandra
Doctor of Philosophy, 2020

Dissertation directed by: Professor Michelle Girvan
Department of Physics

The Kuramoto model (KM) was initially proposed by Yoshiki Kuramoto in 1975 to model the dynamics of large populations of weakly coupled phase oscillators. Since then, the KM has proved to be a paradigmatic model, demonstrating dynamics that are complex enough to model a wide variety of nontrivial phenomena while remaining simple enough for detailed mathematical analyses. However, as a result of the mathematical simplifications in the construction of the model, the utility of the KM is somewhat restricted in its usual form. In this thesis we discuss extensions of the KM that allow it to be utilized in a wide variety of physical and biological problems.

First, we discuss an extension of the KM that describes the dynamics of theta neurons, i.e., quadratic-integrate-and-fire neurons. In particular, we study networks of such neurons and derive a mean-field description of the collective neuronal dynamics and the effects of different network topologies on these dynamics. This mean-field description is achieved via an analytic dimensionality reduction of the

network dynamics that allows for an efficient characterization of the system attractors and their dependence not only on the degree distribution but also on the degree correlations.

Then, motivated by applications of the KM to the alignment of members in a two-dimensional swarm, we construct a Generalized Kuramoto Model (GKM) that extends the KM to arbitrary dimensions. Like the KM, the GKM in even dimensions continues to demonstrate a transition to coherence at a positive critical coupling strength. However, in odd dimensions the transition to coherence occurs discontinuously as the coupling strength is increased through 0. In contrast to the unique stable incoherent equilibrium for the KM, we find that for even dimensions larger than 2 the GKM displays a continuum of different possible pretransition incoherent equilibria, each with distinct stability properties, leading to a novel phenomenon, which we call ‘Instability-Mediated Resetting.’ To aid the analysis of such systems, we construct an exact dimensionality reduction technique with applicability to not only the GKM, but also other similar systems with high-dimensional agents beyond the GKM.

EXTENSIONS OF THE KURAMOTO MODEL:
FROM SPIKING NEURONS TO SWARMING DRONES

by

Sarthak Chandra

Dissertation submitted to the Faculty of the Graduate School of the
University of Maryland, College Park in partial fulfillment
of the requirements for the degree of
Doctor of Philosophy
2020

Advisory Committee:
Professor Michelle Girvan, Chair/Advisor
Professor Edward Ott, Co-Advisor
Professor Rajarshi Roy
Professor Thomas Antonsen
Professor Brian Hunt

© Copyright by
Sarthak Chandra
2020

Dedication

Dedicated to my parents and my brother, for their constant love and support.

Acknowledgments

First and foremost, I would like to thank my advisor, Dr. Michelle Girvan, and my co-advisor, Dr. Edward Ott, without whom this thesis would not have been possible.

Dr. Girvan has been incredibly helpful to me as a graduate advisor, by always being present to provide useful perspective and direction — not only within academic contexts, but also within broader professional spheres. Despite her busy schedule she has always been able to guide me, and I greatly appreciate all of the meetings and discussion that I have had with her. Her scientific overview of the problems at hand has always been very useful, and is a perspective I hope to gain with time.

I have greatly enjoyed working with Dr. Ott, whose scientific and mathematical skill has always been able to direct me towards new and compelling approaches towards interesting problems. All of the discussions I have had with him have been extremely insightful, and have led me to learn and appreciate a variety of new topics and ideas in physics and mathematics. I greatly appreciate all the discussion I have had with him over the years, which have been able to guide me in both academic and non-academic contexts.

I would also like to thank Dr. Thomas Antonsen, Dr. Rajarshi Roy, and Dr. Brian Hunt, with whom I have had the opportunity to work with and interact

with on several occasions on a variety of interesting projects and at various stages during my research. They have always been available for discussion and have played important roles in the research that I have accomplished over the last few years.

I am also thankful to my friends and fellow graduate students Jaideep Pathak, Sarah Burnett, Zhixin Lu and Alexander Wikner, who have always supported me through my research, and my time at the University of Maryland as a whole, with their unwavering support and help.

I am grateful to all of the staff in the physics and IREAP departments, particularly Jessica Crosby, Josiland Chambers and Nancy Boone.

I am extremely thankful to my parents, Sharad Singhal and Vandana Singhal for their love and support, who were the first to guide me in any sort of studies of science and mathematics; and if my parents were the first in this regard, then my brother, Shashwat Chandra is at a close second. I would not have been the researcher or the person that I am today if not for his constant support and guidance.

There are several friends whom I am very close to, and to whom I am deeply indebted to for all of the support they have given me through the years: Anurag Sahay, Anushka Jha, Iffat Siddiqui, Pratik Rath, Pratik Somani, Prateek Sahu, Shwetha Srinivasan, and Supranta Boruah.

I would also like to thank my close friends at College Park: Abhinav Deshpande, Ankan Bansal, Faez Ahmed, Kiran Burra, Lovlesh Kaushik, Saurabh Saxena and Shashank Ganesh, who have been nothing short of family to me during my time here.

There have been far too many marvelous people who have had a role to play

in my research over the last few years — and this section is too narrow to contain all of their names; I apologize to all of those whose support I have not been able to acknowledge here.

Table of Contents

Dedication	ii
Acknowledgements	iii
Table of Contents	vi
List of Tables	ix
List of Figures	x
Chapter 1: Introduction	1
1.1 Overview	1
1.2 Modeling the Network Dynamics of Pulse-Coupled Neurons	5
1.3 Continuous versus Discontinuous Transitions in the D -Dimensional Generalized Kuramoto Model: Odd D is Different	6
1.4 Observing Microscopic Transitions from Macroscopic Bursts: Instability- Mediated Resetting in the Incoherent Regime of the D -dimensional Generalized Kuramoto Model	7
1.5 Complexity Reduction Ansatz for Systems of Interacting Orientable Agents: Beyond The Kuramoto Model	8
Chapter 2: Modeling the Network Dynamics of Pulse-Coupled Neurons	10
2.1 Introduction	11
2.2 The model	13
2.3 Mean Field Formulation	14
2.4 Dimension Reduction	16
2.5 Numerical simulations and results	23
2.5.1 Fixed points	25
2.5.2 Limit Cycles	34
2.5.3 Effect of Assortativity	35
2.6 Conclusion	38
Chapter 3: Continuous versus Discontinuous Transitions in the D -Dimensional Generalized Kuramoto Model: Odd D is Different	40
3.1 Introduction	40
3.1.1 Background	40
3.1.2 Main Result	43

3.1.3	Relation to Statistical Physics Models	44
3.2	Model Description	45
3.3	Dynamics and Equilibria	54
3.3.1	Coherent states for $D = 3$	56
3.3.2	Incoherent states for $D = 3$	66
3.3.3	Phase transition in even dimensions	73
3.4	Model variant: Extended-body agents in three dimensions	78
3.5	Discussion and conclusions	89
Chapter 4: Observing Microscopic Transitions from Macroscopic Bursts: Instability-Mediated Resetting in the Incoherent Regime of the D -dimensional Generalized Kuramoto Model		93
4.1	Introduction	94
4.1.1	Background	94
4.1.2	The Rotation Rates \mathbf{W}_i	97
4.1.3	The $N \rightarrow \infty$ limit and the multiplicity of incoherent equilibria	98
4.1.4	The Dynamical phase transition	99
4.1.5	Linear Stability of the incoherent equilibria	101
4.1.6	Instability-Mediated Resetting (IMR)	102
4.1.7	Main points of this chapter	103
4.2	Incoherent Equilibria	104
4.3	Stability of incoherent equilibria	110
4.4	Macroscopic bursts and Instability-Mediated Resetting	126
4.4.1	Macroscopic bursts of coherence	129
4.4.2	Instability-Mediated Resetting	131
4.4.3	Resetting due to finite size	136
4.5	Conclusions	139
Chapter 5: Complexity Reduction Ansatz for Systems of Interacting Orientable Agents: Beyond The Kuramoto Model		141
5.1	Introduction	142
5.2	Generalizing Kuramoto-like Agents to Higher Dimensions	144
5.3	Analytic Solution in the Limit of Large Systems	147
5.4	Example Systems	150
5.4.1	The Kuramoto Model Generalized to Higher Dimensions	150
5.4.2	Applications of Eq. (5.15) to previous results on the Generalized Kuramoto model	154
5.4.3	Other Examples	160
5.5	Discussion and Conclusions	162
Chapter 6: Conclusions		165
Appendix A: Additional proofs pertinent to Chapter 3		169
A.1	Equation for fixed points of agents	169
A.2	Simplification of continuity equation	171

A.3 Critical coupling constant for even dimensions	174
Appendix B: Additional proof pertinent to Chapter 5	179
B.1 Proof of Eq. (5.15)	179
Bibliography	181

List of Tables

4.1	Expressions for $h(0)$ and numerical values of $K_c^{(-)}$, $K_c^{(u)}$ and $K_c^{(+)}$ for $D = 2, 4, 6$ and 8 . The expression for $h(0)$ is obtained from Chapter 3, and the values of the various critical coupling strengths are obtained from Eq. (4.66)	125
-----	---	-----

List of Figures

2.1	The dynamics of the theta neuron undergo an SNIC (Saddle node on an Invariant Cycle) bifurcation at $\eta = 0$. For negative η the neuron lies in a rest state, with a threshold for excitation, and for positive η the oscillator undergoes periodic spiking.	15
2.2	The effect of varying levels of interpolation on the calculated results for the trajectories of $\bar{R}(t)$ in the complex plane starting from an initial condition of $\bar{R}(t) = 0$ and ending at a fixed point attractor for $K = 3$ in a network with neutral assortativity, with $\eta_0 = -2$ and $\Delta = 0.1$. Calculation of the order parameter dynamics is robust to a large range in the level of interpolation. Using as few as 10% of the total available degrees and interpolating the remaining 90% give results close to the calculation without interpolation. In the rest of this chapter we employ a 10% interpolation level in all our mean field calculations. The black arc is a segment of the unit circle $ \bar{R}(t) = 1$.	24
2.3	(a): Fixed points of $R(t)$ observed in networks with neutral assortativity, $\eta_0 = -2$ and $\Delta = 0.1$, for three values of the coupling strength K . Fixed points in the PR state ($K = 1$) and the AF state ($K = 6$) are marked in the complex plane. The fixed point at an intermediate value of K is also marked.(b),(c),(d): Time series of the cosine of the phase of 5 randomly chosen neurons demonstrates that in the PR phase almost all neurons are in a resting state, and as the system approaches the AF state, more nodes transition to an oscillating, excited state.The thick dashed line corresponds to the position of the fixed point of the order parameter for the corresponding value of K .	26
2.4	Comparison of $ \hat{b}(k_{in}) $ from the reduced system of equations and the time average of $ R(k_{in}) $ from the full system, Eq. (2.26), for a network with neutral assortativity ($c = 0$), $\eta_0 = -2$, and $\Delta = 0.1$ at $K = 3$. The dynamics under these parameters were simulated in a network with 5000 nodes, and the network was allowed to relax to a fixed point. Nodes were divided into classes according to their in-degree to calculate the time averaged effective order parameter for each class, which is shown in blue, with the error bars denoting the root mean squared time fluctuation of the order parameter for that class. The time fluctuations are due to the finite number of nodes in each class. (See text for details.)	30

2.5	A sweeping value of K was used to observe the change in phase from the PR state to the AF state. Hysteresis was observed on the network with a highly skewed degree distribution (a) as well as a corresponding Erdős-Rényi network having the same size and the same average degree (b). For the full network, at each value of K the mean of the order parameter after ignoring the transients have been marked as triangles. A close match is observed with the fixed points as computed from mean field equations directly (see text for details). Hysteresis is observed for $3.25 \lesssim K \lesssim 4$ in the network with the highly skewed degree distribution (a), and is observed for $3 \lesssim K \lesssim 7.25$ in the corresponding Erdős-Rényi network (Note the difference in scales for the x-axis in both plots). An apparent crossing of the fixed point curve is seen in (b), which is an artifact of the non-self-intersecting \bar{R} curve lying in the two dimensional complex space, which has been projected onto the real axis in this plot.	33
2.6	Comparison of the limit cycle attractor for $\bar{R}(t)$ in the complex plane across varying degree distributions in a network with neutral assortativity ($c = 0$) with $\eta_0 = 10.75$, $\Delta = 0.5$ and $K = -9$. The highly skewed network (blue solid curve) has a degree distribution according to Eq. (2.25), the Erdős-Rényi network (green dashed curve) has a Poissonian degree distribution, and the regular network (red dotted curve) has a delta function degree distribution. The black circle is the unit circle $ \bar{R} =1$	36
2.7	For the parameters $\eta_0 = 4$, $\Delta = 0.5$ and $K = -4.8$, in a network with neutral assortativity ($c = 0$), the system lies in an SF state (as in (b)). Varying the assortativity in either direction ($c = \pm 2.5$, corresponding to $r \approx \pm 0.198$) causes the limit cycles to be replaced by a fixed point instead (as in (a),(c)). The behavior predicted by the mean field theory is in agreement with the simulations of the full network.	37
3.1	Phase transitions for the standard two-dimensional Kuramoto model from theory, shown as the black dashed curve, and for the Kuramoto model generalized to three dimensions as calculated from the theory in Eq. (3.18), shown as the solid red curve. Note the continuous transition in the two-dimensional Kuramoto model at a critical coupling of $K_c > 0$, and the discontinuous transition of the three-dimensional Kuramoto model at $K_c = 0$. The blue dotted line represents the maximum possible value of coherence, corresponding to $ \rho =1$	46
3.2	Illustration showing that $[\sigma_j - (\sigma_j \cdot \sigma_i)\sigma_i] = \hat{\theta}_i \sin(\theta_j - \theta_i)$, where $\hat{\theta}_i$ is a unit vector in the direction of increasing θ_i	47
3.3	σ_i precesses around $\hat{\omega}_i$ with an angular frequency of ω_i for $K = 0$ with $D = 3$	50

3.4	(a) Phase transitions for the generalized Kuramoto model for $D = 2$ (red plus signs), 4 (blue inverted triangles), 6 (green triangles) and 8 (magenta stars) dimensions, numerical observations for $N = 10^5$. (b) Phase transitions for the Kuramoto model generalized to $D = 3$ (red plus signs), 5 (blue inverted triangles), 7 (green triangles) and 9 (magenta stars) dimensions, numerical observations for $N = 10^4$. $\Delta = 1$ in each. The theoretical predictions from Eqs. (3.42) and (3.44) for the critical coupling strength for even dimensions has been shown in correspondingly colored arrows on the x -axis in (a). For a discussion on the slight mismatch between the theory and the numerical results, see Sec. 3.3.3. We expect this mismatch to decrease with increasing N . The theoretical estimates from Eq. (3.13) for the magnitude of the discontinuity, i.e., $ \rho $ at $K \rightarrow 0^+$ are shown in correspondingly colored arrows on the y -axis in (b). Note the close match between the theoretical result for the discontinuity, and the numerical observation for $ \rho $ at $K = 0.2$	55
3.5	Orientations of each of the $N = 5 \cdot 10^3$ agents at time $T = 0$, $T = 500$ and $T = 50000$. We visualize the orientations by plotting the endpoints of the orientation vectors on the sphere \mathcal{S} . The sphere is then mapped onto a rectangle using an area-preserving transformation. We choose the z -axis along ρ , and arbitrarily choose mutually orthogonal x and y axes. θ then represents the angle measured from the z -axis ($\cos \theta = \hat{\rho} \cdot \sigma$), and ϕ represents the azimuthal angle measured anti-clockwise from the x -axis. The agent state vectors are initialized with a uniform distribution on the sphere, and evolved with a coupling constant $K = 0.1$. Note how all of the agents tend to uniformly distribute themselves on one hemisphere.	60
3.6	Phase transition for Kuramoto model generalized to three dimensions. The solid (dashed) black curve represents the derived stable (unstable) fixed points for the order parameter, and the red plus sign markers represent numerical results from a simulation with $N = 10^4$ agents and $\Delta = 1$	62
3.7	$N = 1000$ agents were simulated with a coupling strength of $K = -2$. Histograms of $z_i = \sigma_i \cdot \hat{\omega}_i$ have been plotted at $T = 0$ (in blue, corresponding to the initial condition having σ_i uniformly spread on \mathcal{S}), and after $T = 1.25 \cdot 10^5$ time units (in red). Note how the distributions concentrate at 1 and -1 for large T . In the insets, we show plots of z_i as a function of time for 50 randomly chosen agents.	70
3.8	Illustration of an extended-body agent. Unlike the agents in the generalized Kuramoto model Eq. (3.2), we assume that the state of an extended-body agent cannot be described by a single unit vector σ . Rather, the pair of vectors σ and η together describe the orientation and state of the agent. The direction of agent velocity is assumed to be along the direction σ as earlier. The unit vector ν is defined as $\nu = \sigma \times \eta$	80

3.9	Phase transition for interacting three-dimensional extended-body agents described by Eqs. (3.56) – (3.58). The dynamics of individual agents in this system have been constructed to satisfy constraints imposed by extended-body dynamics, and are <i>not</i> equivalent to the dynamics of the generalized Kuramoto model described in Sec.3.3. Despite this, we continue to observe a discontinuous jump in the asymptotic steady-state value of $ \rho $ as K is increased through 0.	85
4.1	Dynamical Phase Transition for the Generalized Kuramoto model for $D = 2$ (green stars), 4 (orange triangles), 6 (magenta squares) and 8 (blue diamonds) dimensions. The $ \rho $ values indicated by the plotted markers are obtained by choosing the values of $\sigma_i(t = 0)$ and \mathbf{W}_i for each of the $N = 10^5$ agents randomly (where the probability distribution of $\sigma_i(0)$ is isotropic in direction and that of \mathbf{W}_i is as given in Sec. 4.2) and then integrating Eq. (4.2) from each such initial condition until $ \rho(t) $ attains a steady value. These steady state values attained appeared to be independent of this choice of initial condition. The theoretical predictions from Chapter 3 for the critical coupling strength, $K_c^{(+)}$, above which stable $ \rho > 0$ steady states exist are indicated by correspondingly colored vertical arrows on the x -axis.	100
4.2	$K_c(q)$ vs q for the case of the minimally stable distribution (shown in green, labelled $K_c^{(min)}(q)$) corresponding to Eq. (4.64) and the maximally stable distribution (shown in purple, labelled $K_c^{(max)}(q)$) corresponding to Eq. (4.65) for $D = 4$. Note that $K_c(q)$ is always bounded by $1/[\pi h(q)]$ (shown as the red dashed curve) and $2/[\pi h(q)]$ (shown as the orange dashed curve) as indicated in Eq. (4.59). The critical coupling strength for the onset of instability, K_c for a given distribution is given by the minimum value attained by $K_c(q)$, which for $K_c^{(min)}(q)$ and $K_c^{(max)}(q)$ is at $q = 0$. ($K_c^{(max)}(q)$ appears to be approximately minimized at $q \approx 2.12$, corresponding to a value of $K_c(q) = 2.141$. The true minima however is at $q = 0$, corresponding to $K_c(q) = 2.128$)	124

- 4.3 Representative plots demonstrating the short-lived macroscopic burst of coherence and the resulting IMR. (a) The magnitude of the order parameter (orange solid curve) and $\langle C_{min} \rangle$ (blue dashed curve) as a function of time for a system setup with a minimally stable distribution corresponding to $\langle C_{min} \rangle = 0$ and evolved with $K = 1.4$. Note the sharp rise and fall of $|\rho|$, i.e. the macroscopic burst of coherence, accompanied by the increase of the value of $\langle C_{min} \rangle$ (i.e., IMR). This results in an increase of the critical coupling constant for instability onset of the new incoherent distribution. Panels (b) and (c) show the order parameter evolution beginning with the distribution function at the last time-step of (a) but with K increased to $K = 1.6$ and 2.0 respectively. The presence of a macroscopic burst of $|\rho|$ in (c) and not in (b) indicates that K_c has been reset to a value between 1.6 and 2.0. In panel (d) $|\rho|_{max}$ indicates the largest value of $|\rho|$ for systems initialized similar to (b) or (c) following a discontinuous increase of the coupling constant to a value K plotted on the horizontal axis. $|\rho|_{max}$ is macroscopically observable (i.e., distinguishable from finite- N -induced fluctuations) for bursts of $|\rho|$, and approximately 0 for incoherent steady-state distributions without any such burst. Hence (d) indicates that, by the end of the simulation in panel (a), due to IMR the critical coupling strength has been reset to $K_c \approx 1.75$. See text for more details. 128
- 4.4 Transitions demonstrating the results derived in Eq. (4.66) for a system with $N = 10^6$. For the minimally stable distribution (red circles), the uniform σ distribution (blue triangles), and the maximally stable distribution (green stars), the system is evolved for various values of K . The maximum value attained by $|\rho(t)|$ over a short evolution is shown as a function of K . For incoherent steady-state distributions that undergo stable evolution at a given value of K , $|\rho|_{max}$ is approximately zero, whereas instability of incoherent steady-state distributions results in a short-lived burst of coherence, resulting in a larger value of $|\rho|_{max}$. The theoretical predictions for the transitions to instability are shown in the respective colors using vertical dashed lines, and agree well with the numerical results. (Note that for $K > K_c^{(+)}$, $|\rho|_{max}$ corresponds to the stable state of $|\rho| > 0$ shown in Fig. 4.1 as opposed to the peak value during these short bursts.) 133

- 4.5 Evolution of $|\boldsymbol{\rho}(t)|$ for a system having $N = 10^6$ initialized at a minimally stable incoherent steady-state distribution with slow temporally linear increase in K shown in orange, and a sliding average shown in red. The temporal increase of K is linear in time and is indicated by the horizontal axis at the top of the figure panel. The vertical dashed lines correspond to $K_c^{(-)}$ and $K_c^{(+)}$. For $K \leq K_c^{(-)}$ the initialized steady-state distribution is stable and hence $|\boldsymbol{\rho}|$ maintains a value close to zero. For $K_c^{(-)} < K < K_c^{(+)}$ the system demonstrates enhanced fluctuations of $|\boldsymbol{\rho}|$ about increased, nonzero values that are apparently sustained by the continuous increase of K . For $K \geq K_c^{(+)}$ no incoherent distribution is stable, and $|\boldsymbol{\rho}|$ attains a larger value similar to Fig. 4.1 135
- 4.6 Slow finite- N -induced evolution of the incoherent steady-state distributions for (a) $N = 10^3$ and (b) $N = 10^4$. Note the significantly longer timescales shown here as compared with the Fig. 4.3. $|\boldsymbol{\rho}|$ is shown as the orange curve, and $\langle C_{min} \rangle$ is shown as the blue dashed curve. Further, note the larger timescale for (b) as compared with (a). In both cases the system was initialized to a minimally stable incoherent steady-state distribution with $\langle C_{min} \rangle = 0$. $|\boldsymbol{\rho}|$ remains approximately zero, indicating that the system remains in \mathcal{M} , but the gradual increase in $\langle C_{min} \rangle$ indicates the change in distribution on \mathcal{M} . The final distribution achieved after long time evolution is a maximally stable distribution. 137

5.1	(a),(b): Comparison between the dynamics of the magnitude of the order parameter, $ \mathbf{z} $, as a function of time via full system modeling of the generalized Kuramoto model with $D = 3$ (Eq. (5.2) for $\boldsymbol{\rho}$ given by Eq. (5.19)) using $N = 5000$ agents shown in black, with the modeling of the reduced differential equation Eq.(5.15) plotted as the orange dashed line. $K = 2$ for both figures. (a) is the case of homogenous agents, i.e., $G(\mathbf{W}) = \delta(\mathbf{W} - \mathbf{W}_0)$. (b) is the case of heterogeneous agents, where the distribution $G(\mathbf{W})$ is nonsingular and chosen as described in the main text. Only $N_{\mathbf{W}} = 500$ Monte-Carlo samples were required to produce the curve for the reduced system of equations, representing the $N \rightarrow \infty$ limit of the full system, approximated by the noisy curve generated using $N = 5000$ agents for the full system. (c) demonstrates similar agreement for the case of heterogeneous agents in $D = 4$, where the system is evolved at $K = 1.7$ from the uniform incoherent distribution as the initial condition. $N = N_{\mathbf{W}} = 10^6$ was used for numerical integration of the two curves. Note how the reduced equations capture the transient behavior of the Instability-Mediated Resetting phenomenon (introduced in Chapter4). Since the initial finite-size noise is different in the two cases, in order to make the curves for the full system and the reduced equations lie on each other, we shift them in time to align them. See text for further details of initial conditions used.	155
5.2	A simulation of the phase transition to coherence via numerical integration of Eq. (5.2) for $\boldsymbol{\rho}$ given by Eq. (5.19) representing the full system dynamics with $N = 5000$ (shown in the black triangular markers), and via numerical integration of Eq. (5.15) representing the dynamics on the invariant manifold with $N_{\mathbf{W}} = 500$ (shown as the orange inverted triangles) for $D = 3$. For each value of K , the system is evolved until $ \boldsymbol{\rho} $ reaches an equilibrium. Note the close agreement between the time asymptotic values of $ \boldsymbol{\rho} $ at all values of K . The distribution $G(\mathbf{W})$ was chosen as described earlier for heterogeneous agents.	156
A.1	The shaded regions (in blue, green and orange) correspond to the domain Γ in which $\sum_k 1/\mu_k^2 > 1$ for the case of $D = 4$ ($\Lambda = 2$) in the $\{\mu_1, \mu_2\}$ -space. The subdomain Γ_0 , shown in blue, is the part of Γ inside the circle of radius L ; and the subdomains Γ_i are the parts of the domain Γ that lie outside Γ_0 which do not contain the μ_i axis (Γ_1 is shown in orange, and Γ_2 in green). The width of the strips in Γ far away from the origin is 1, hence the volume of the subdomain Γ_0 will scale as $\mathcal{O}(L^{\Lambda-1})$ for large L	175

Chapter 1: Introduction

1.1 Overview

In his very first paper [1], shortly before starting graduate school, Winfree asked the question “What special phenomena can we expect to arise from rhythmic interaction of whole populations of periodic processes?” Winfree formulated this problem via interactions between large populations of limit cycle oscillators, whose dynamics he attempted to simplify for the case of near-identical oscillators with weak coupling. Under this setup, he argued that one can characterize the state of each oscillator via only their phase along the limit cycle, i.e., each entity of the population can be described as a ‘phase oscillator’. While he could not derive a complete mathematical analysis of the system, he used a mixture of numerical and mathematical analysis to observe the presence of a phase transition to synchronization in the system.

Kuramoto, in 1975, motivated by some previous work of his on chemical instabilities, wrote down the following equations to model a community exhibiting

mutual synchronization [2]

$$\frac{d\theta_j}{dt} = \omega_j + \frac{K}{N} \sum_{k=1}^N \sin(\theta_k - \theta_j), \quad (1.1)$$

where θ_i represents the phase angle of the i^{th} oscillator, ω_i is its natural frequency of oscillation, and K is the coupling strength between oscillators. The natural frequencies are usually assumed to be drawn from a unimodal probability distribution, $g(\omega)$, characterizing how similar individual oscillators are. While Kuramoto only briefly noted in 1975 that his model exhibits the kinds of phase transitions Winfree and earlier described, he later [3] demonstrated that these equations arise naturally from Winfree's setup after further simplifications and assumptions regarding the nature of the phase oscillators being considered.

Since this initial work, the Kuramoto model and its generalizations have since been used to study synchronization behavior in a wide variety of systems, modeling biological problems such as the behavior of cardiac pacemaker cells [4], synchronization in large groups of flashing fireflies [5, 6], circadian rhythms [7, 8], and neuronal synchronization [9], as well as problems in physics and engineering such as synchronization of power-grid networks [10, 11], superconducting Josephson junctions [12], atomic physics [13], and neutrino oscillation [14], among others; Kuramoto himself has remarked that he has been surprised at such physical systems following his model [15].

Given this wide applicability of the Kuramoto model to systems that are not immediately apparent as phase oscillators, in this thesis we will often refer to the

individual entities of the populations as ‘agents’.

To describe the collective dynamics of the entire population, a complex order parameter $\rho = |\rho|e^{i\psi}$ is defined as

$$\rho = \frac{1}{N} \sum_{k=1}^N e^{i\theta_k}. \quad (1.2)$$

This order parameter can be interpreted as a single quantity that characterizes the state of synchronization in the system; $|\rho|$ measures the magnitude of phase coherence in the system, and ψ measures the average phase in the system. In terms of this order parameter, we can rewrite Eq. (1.1) as

$$\frac{d\theta_j}{dt} = \omega_j + K \operatorname{Im} [\rho e^{-i\theta_j}] = \omega_j + K|\rho|\sin(\psi - \theta_j). \quad (1.3)$$

In terms of this expression, we can see that the Kuramoto model essentially models an interplay between the collective dynamics of the system, ρ (which is usually some mean field quantity, such as in Eq. (1.2)), and the individualistic tendency of each agent, ω_j . Using the above equations, under the additional assumption that $g(\omega)$ was a Lorentzian distribution, Kuramoto [2] showed that a continuous phase transition to coherence occurs at a critical coupling strength

$$K_c = \frac{2}{\pi g(0)}. \quad (1.4)$$

One can relax the assumption that $g(\omega)$ is Lorentzian for the above result to hold — it is sufficient that $g(\omega)$ is unimodal, symmetric about its mean and continuous

(for a proof of more general versions of this result, see Chapters 3 and 4).

In the decades that followed, there have been a large number of interesting mathematical results treating the Kuramoto model (see Refs. [9,16,17] for reviews). A seminal contribution to this subject was made in 2008 by Ott and Antonsen [18], where they discovered that the dynamics of the Kuramoto model admit a low dimensional invariant manifold in the infinite population size limit. This result was further refined in the next two years [19,20] where it was shown under a set of weak assumptions that this invariant manifold is attracting. Thus, for problems where this infinite size limit was relevant, it was shown to be sufficient to study the dynamics of the population on the invariant manifold, a significantly simpler problem due to the low dimensionality of the manifold.

A surprising discovery of these papers was that this attracting invariant manifold exists for not only the Kuramoto model as stated in Eq. (1.1), but to the wider class of models given by Eq. (1.3), where ρ need not be given by Eq. (1.2) and can be a more general function of the individual agent phases. This allowed the ‘Ott-Antonsen’ (OA) method to be immediately applicable to several problems that could be modeled via this form of an extension to the Kuramoto model [12,21–26].

One particular instance of this extension to the Kuramoto model is the ‘theta neuron’ model, which describes the dynamics of quadratic-integrate-and-fire neurons [22]. This particular model is the main focus of interest of Chapter 2, where we discuss how the OA method can be applied to networks of such theta neurons. Studying the dynamics of this system on the underlying invariant manifold allows us to efficiently analyze the dynamics of such networks of neurons.

By the construction of our setup thus far, our attention has been restricted to problems where the state of each agent is described by a single scalar angle. Thus, the Kuramoto model can be thought of as describing the collective dynamics of points that lie on the unit circle. Motivated by this observation, and the application of the Kuramoto model to classical XY spins [27–30] and herding animals [31–33], in Chapter 3 we construct a generalization of the Kuramoto model to arbitrary dimensions. This generalization is the primary object of our focus in Chapters 3, 4 and 5. In particular, Chapters 3 and 4 describe the wide range of novel dynamical phenomena displayed by this generalization, and Chapter 5 discusses how the OA method can be extended to this generalized system.

The remainder of this thesis is organized into the following chapters:

1.2 Modeling the Network Dynamics of Pulse-Coupled Neurons

In this chapter, we derive a mean-field approximation for the macroscopic dynamics of large networks of pulse-coupled theta neurons in order to study the effects of different network degree distributions, as well as degree correlations (assortativity). Using the Ott-Antonsen ansatz [18], we obtain a reduced system of ordinary differential equations describing the mean-field dynamics, with significantly lower dimensionality compared with the complete set of dynamical equations for the system. We find that, for sufficiently large networks and degrees, the dynamical behavior of the reduced system agrees well with that of the full network. This dimensional reduction allows for an efficient characterization of system phase transitions and

attractors. For networks with tightly peaked degree distributions, the macroscopic behavior closely resembles that of fully connected networks previously studied by others. In contrast, networks with highly skewed degree distributions exhibit different macroscopic dynamics due to the emergence of degree dependent behavior of different oscillators. For nonassortative networks (i.e., networks without degree correlations) we observe the presence of a synchronously firing phase that can be suppressed by the presence of either assortativity or disassortativity in the network. We show that the results derived here can be used to analyze the effects of network topology on macroscopic behavior in neuronal networks in a computationally efficient fashion. This work was published as Ref. [34]

1.3 Continuous versus Discontinuous Transitions in the D -Dimensional Generalized Kuramoto Model: Odd D is Different

The Kuramoto model has been used and generalized for a wide range of applications involving the collective behavior of large heterogeneous groups of dynamical units whose states are characterized by a scalar angle variable. One such application in which we are interested is the alignment of orientation vectors among members of a swarm. Despite being commonly used for this purpose, the Kuramoto model can only describe swarms in 2 dimensions, and hence the results obtained do not apply to the often relevant situation of swarms in 3 dimensions. Partly based on this motivation, as well as on relevance to the classical, mean-field, zero-temperature Heisenberg model with quenched site disorder, in this chapter we study the Ku-

ramoto model generalized to D dimensions. We show that in the important case of 3 dimensions, as well as for any odd number of dimensions, the D -dimensional generalized Kuramoto model for heterogeneous units has dynamics that are remarkably different from the dynamics in 2 dimensions. In particular, for odd D the transition to coherence occurs discontinuously as the inter-unit coupling constant K is increased through zero, as opposed to the $D = 2$ case (and, as we show, also the case of even D) for which the transition to coherence occurs continuously as K increases through a *positive* critical value K_c . We also demonstrate the qualitative applicability of our results to related models constructed specifically to capture swarming and flocking dynamics in three dimensions. This work was published as Ref. [35].

1.4 Observing Microscopic Transitions from Macroscopic Bursts: Instability-Mediated Resetting in the Incoherent Regime of the D -dimensional Generalized Kuramoto Model

In the previous chapter it was shown that, for even (but not odd) D , similar to the original Kuramoto model ($D = 2$), there exists a continuous dynamical phase transition from incoherence to coherence of the time asymptotic attracting state (time $t \rightarrow \infty$) as the coupling parameter K increases through a critical value which we denote $K_c^{(+)} > 0$. We consider this transition from the point of view of the stability of an incoherent state, where an incoherent state is defined as one for which the $N \rightarrow \infty$ distribution function is time-independent and the macroscopic order parameter is zero. In contrast with $D = 2$, for even $D > 2$ there is an infinity

of possible incoherent equilibria, each of which becomes unstable with increasing K at a different point $K = K_c$. Although there are incoherent equilibria for which $K_c = K_c^{(+)}$, there are also incoherent equilibria with a range of possible K_c values below $K_c^{(+)}$, $(K_c^{(+)}/2) \leq K_c < K_c^{(+)}$. How can the possible instability of incoherent states arising at $K = K_c < K_c^{(+)}$ be reconciled with the previous finding that, at large time ($t \rightarrow \infty$), the state is always incoherent unless $K > K_c^{(+)}$? We find, for a given incoherent equilibrium, that, if K is rapidly increased from $K < K_c$ to $K_c < K < K_c^{(+)}$, due to the instability, a short, macroscopic burst of coherence is observed, in which the coherence initially grows exponentially, but then reaches a maximum, past which it decays back into incoherence. Furthermore, after this decay, we observe that the equilibrium has been reset to a new equilibrium whose K_c value exceeds that of the increased K . Thus this process, which we call ‘Instability-Mediated Resetting,’ leads to an increase in the effective K_c with continuously increasing K , until the equilibrium has been effectively set to one for which $K_c \approx K_c^{(+)}$. Thus Instability-Mediated Resetting leads to a unique critical point of the $t \rightarrow \infty$ time asymptotic state ($K = K_c^{(+)}$) in spite of the existence of an infinity of possible pretransition incoherent states. This work was published as Ref. [36].

1.5 Complexity Reduction Ansatz for Systems of Interacting Orientable Agents: Beyond The Kuramoto Model

Previous results have shown that a large class of complex systems consisting of many interacting heterogeneous phase oscillators exhibit an attracting invariant

manifold. This result has enabled reduced analytic system descriptions from which all the long term dynamics of these systems can be calculated. Although very useful, these previous results are limited by the restriction that the individual interacting system components have one-dimensional dynamics, with states described by a single, scalar, angle-like variable (e.g., the Kuramoto model). In this chapter we consider a generalization to an appropriate class of coupled agents with higher-dimensional dynamics. For this generalized class of model systems we demonstrate that the dynamics again contain an invariant manifold, hence enabling previously inaccessible analysis and improved numerical study, allowing a similar simplified description of these systems. We also discuss examples illustrating the potential utility of our results for a wide range of interesting situations. This work was published as Ref. [\[37\]](#)

Chapter 2: Modeling the Network Dynamics of Pulse-Coupled Neurons

In April 2013, the U.S. President announced ‘The Brain Initiative,’ an extensive, long range plan of scientific research on human brain function. Computer modeling of brain neural dynamics is an important component of this long-term overall effort. A barrier to such modeling is the practical limit on computer resources given the enormous number of neurons in the human brain ($\sim 10^{11}$). Our work addresses this problem by developing a method for obtaining low dimensional macroscopic descriptions for functional groups consisting of many neurons. Specifically, we formulate a mean-field approximation to investigate macroscopic network effects on the dynamics of large systems of pulse-coupled neurons and use the ansatz of Ott and Antonsen to derive a reduced system of ordinary differential equations describing the dynamics. We find that solutions of the reduced system agree with those of the full network. This dimensional reduction allows for more efficient characterization of system phase transitions and attractors. Our results show the utility of these dimensional reduction techniques for analyzing the effects of network topology on macroscopic behavior in neuronal networks.

2.1 Introduction

Networks of coupled oscillators have been shown to have a wide variety of biological, physical and engineering applications [10, 11, 22, 25, 38–46]. In modelling the dynamics of such networks, simulating the microscopic behavior at each node can be a computationally intensive task, especially when the network is extremely large. In this regard, we note that the dimension reduction analyses in Refs. [18–20] has recently proved to be very effective and has been used to derive the macroscopic behavior of large systems of coupled dynamical units in a variety of settings [25, 44, 47–52]. In particular, Refs. [22, 25, 44, 45] consider networks with globally coupled neurons and use these dimension reduction techniques to analyze the macroscopic behavior of the systems.

In 1986, Ermentrout and Kopell [53] introduced the theta neuron model. Their work, along with later studies by Ermentrout [54] and by Izhikevich [55], established the applicability of the theta neuron model for studying networks of Class I excitable neurons (as defined by Hodgkin, [56] i.e., those neurons whose activity lies near the transition between a resting state and a state of periodic spiking, and can exhibit spiking with arbitrarily low frequencies).

Previous studies modeling networks of theta neurons [22, 48, 52, 57] have generally been restricted to particular classes of network topologies. In this chapter we study the macroscopic dynamics of networks of pulse coupled theta neurons on networks with fairly general topologies including arbitrary degree distributions and correlations between the degrees of nodes at opposite ends of a link, resulting in so-

called ‘assortativity’ or ‘disassortativity’ [58]. Assortativity (disassortativity) occurs when network nodes connect preferentially to those with similar (different) degrees. We note that, studies [59–63] have shown the biological relevance of assortativity. Motivated by the results of Restrepo and Ott [47] on networks of Kuramoto oscillators, we use a mean field approach in conjunction with the analytical techniques developed by Ott and Antonsen [18–20] to study the behavior of pulse coupled theta neurons on networks with arbitrary degree distributions and assortativity. We obtain a reduced system of equations describing the mean-field dynamics of the system, with lower dimensionality compared with the complete set of dynamical equations for the system. This allows us to examine the behavior of the network under various conditions in a computationally efficient fashion. We primarily use the example of a highly skewed degree distribution as an application of the obtained dynamical equations for the order parameter and observe the existence of a partially resting phase, an asynchronously firing phase, and a synchronously firing phase that is sensitive to the presence of assortativity or disassortativity in the network. We also demonstrate that, in contrast to networks with sharply peaked degree distributions, networks with highly skewed degree distributions exhibit different macroscopic dynamics due to the emergence of degree dependent behavior of different oscillators.

The remainder of this chapter is organized as follows. In Sec. 5.2 we describe the model of pulse coupled theta neurons used on an arbitrary network. In Sec. 2.3 we setup a mean field description of the behavior on the network, and then (Sec. 2.4) show how the methods developed by Ott and Antonsen [18–20] can be used to write a low dimensional set of equations describing the dynamics of the mean field

order parameter. In Sec. 2.5 we then use this low dimensional system to describe the behavior of the system under different parameters and network topologies. Section 2.6 concludes the chapter with further discussion and summary of the main result.

2.2 The model

The theta neuron model encodes the dynamics of a single neuron in isolation as follows,

$$\dot{\theta} = (1 - \cos \theta) + (1 + \cos \theta)\eta, \quad (2.1)$$

where θ represents the neuron's state and the parameter η specifies its excitability. The dynamics can be visualized as a point traveling around the unit circle (Fig. 2.1). A neuronal spike is said to occur each time the phase angle of the neuron, θ , crosses the leftmost point at $\theta = \pi$. When $\eta < 0$, there are two zeros of the right hand side of Eq. (2.1), representing a stable rest state (solid circle in Fig. 2.1(a)) and an unstable equilibrium (open circle in Fig. 2.1(a)). Thus, starting from a typical initial condition, the state of the neuron goes towards the stable equilibrium at the rest state represented by the filled circle. A resting neuron will spike if an external force pushes its state (i.e. the angle θ) from the rest state past the unstable equilibrium (termed as the 'spiking threshold'). As η is increased above 0, the neuron exhibits a Saddle Node bifurcation on an Invariant Cycle (SNIC). In this case there are no fixed points (i.e. no zeros of the right hand side of Eq. (2.1)), and the neuron now fires periodically, as shown in Fig. 2.1(c). Note that the neuron does not move at the same rate along the entire circle, and may go faster or slower around $\theta = \pi$

dependent on whether η is less than or greater than 1, respectively (eg. see the plot of $(1 - \cos \theta)$ versus time in Fig. 2.1(c)).

The theta neuron model can be extended from a single neuron in isolation to networks of neurons. We consider a system of N theta neurons coupled together in a general network via pulse-like synaptic signals, I_i , to each neuron i :

$$\dot{\theta}_i = (1 - \cos \theta_i) + (1 + \cos \theta_i)[\eta_i + I_i], \quad (2.2)$$

$$I_i = \frac{K}{\langle k \rangle} \sum_{j=1}^N A_{ij} P_n(\theta_j), \quad (2.3)$$

where A_{ij} is the adjacency matrix of a network; $A_{ij} = 1$ if there is a directed edge from node j to node i , and $A_{ij} = 0$ otherwise. The average degree is then given by $\langle k \rangle = \sum_{i,j} A_{ij} / N$. $P_n(\theta) = d_n(1 - \cos \theta)^n$ represents the pulse-like synapse, whose sharpness is controlled by the integer parameter n . The normalization constant d_n is determined so that $\int_0^{2\pi} P_n d\theta = 2\pi$, giving $d_n = 2^n(n!)^2 / (2n)!$. Note that in the case of a fully connected network, where $A_{ij} = 1$ for all i and j , this model reduces to that of Luke et al. [22]

2.3 Mean Field Formulation

We consider the limit of many neurons, $N \gg 1$, and assume the network is randomly generated from a given degree distribution $P(\mathbf{k})$ (normalized such that $\sum_{\mathbf{k}} P(\mathbf{k}) = N$), where \mathbf{k} , the node degree, represents a two-vector of the in-degree

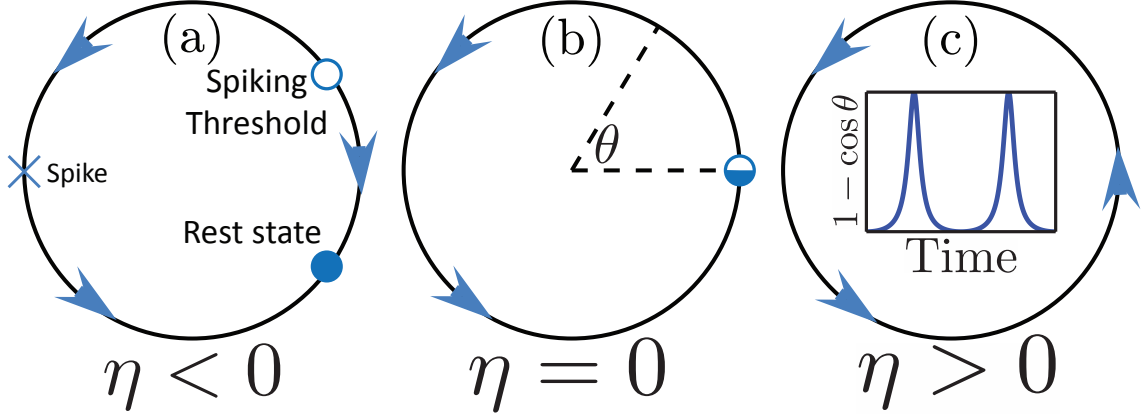


Figure 2.1: The dynamics of the theta neuron undergo an SNIC (Saddle node on an Invariant Cycle) bifurcation at $\eta = 0$. For negative η the neuron lies in a rest state, with a threshold for excitation, and for positive η the oscillator undergoes periodic spiking.

and the out-degree, (k_{in}, k_{out}) . Additionally, we consider an assortativity function $a(\mathbf{k}' \rightarrow \mathbf{k})$, which specifies the probability of a link from a node of degree \mathbf{k}' to one of degree \mathbf{k} . In this $N \rightarrow \infty$ limit, we assume that the state of the neurons can be represented by a continuous probability distribution, $f(\theta, \eta | \mathbf{k}, t)$, such that $f(\theta, \eta | \mathbf{k}, t) d\theta d\eta$ is the probability that a node of degree \mathbf{k} has an excitability parameter in the range $[\eta, \eta + d\eta]$ and a phase angle in the range $[\theta, \theta + d\theta]$ at time t . Since we are assuming that the excitability parameters do not vary with time, we define $g(\eta | \mathbf{k}) = \int f d\theta$, which is the time independent distribution of the excitability parameters η_i in the network for a randomly chosen node of degree \mathbf{k} .

In order to describe the synchronization behavior of this system, we define the order parameter to be,¹

¹Some authors, such as Restrepo and Ott [47] define the order parameter differently so as to be weighted with the out-degree at each node, i.e., $R(t) = \sum_{i=1}^N \sum_{j=1}^N A_{ij} e^{i\theta_j} / \left(\sum_{i=1}^N \sum_{j=1}^N A_{ij} \right)$

$$R(t) = \frac{1}{N} \sum_{j=1}^N e^{i\theta_j}. \quad (2.4)$$

As in previous work by Restrepo and Ott [47], we hypothesize that in networks with large nodal degrees, the order parameter can be well approximated via a mean field order parameter, defined by a continuum version of Eq. (2.4),

$$\bar{R}(t) = \frac{1}{N} \sum_{\mathbf{k}'} P(\mathbf{k}') \int \int f(\theta', \eta' | \mathbf{k}', t) e^{i\theta'} d\theta' d\eta'. \quad (2.5)$$

Additionally, the distribution f is constrained by the continuity equation,

$$\frac{\partial f}{\partial t} + \frac{\partial}{\partial \theta} (v_\theta f) = 0, \quad (2.6)$$

where v_θ is the continuous version of the right hand side of Eq. (2.2),

$$v_\theta = (1 - \cos \theta) + (1 + \cos \theta) \left[\eta + d_n \frac{K}{\langle k \rangle} \sum_{\mathbf{k}'} P(\mathbf{k}') a(\mathbf{k}' \rightarrow \mathbf{k}) \right. \\ \left. \times \int \int f(\theta', \eta' | \mathbf{k}', t) (1 - \cos \theta')^n d\theta' d\eta' \right]. \quad (2.7)$$

2.4 Dimension Reduction

Employing the dimensional reduction method of Ott and Antonsen [18–20], and following its previous application to the theta neuron [22], we assume that f is

given by the Fourier expansion,

$$f(\theta, \eta|\mathbf{k}, t) = \frac{g(\eta|\mathbf{k})}{2\pi} \left\{ 1 + \sum_{p=1}^{\infty} [b(\eta, \mathbf{k}, t)^p e^{-ip\theta} + b^*(\eta, \mathbf{k}, t)^p e^{ip\theta}] \right\}. \quad (2.8)$$

We then use the binomial theorem to expand the pulse function $P_n(\theta)$ using

$$d_n(1 - \cos \theta)^n = A_0 + \sum_{p=1}^n A_p [e^{ip\theta} + e^{-ip\theta}], \quad (2.9)$$

where

$$A_p = \frac{(n!)^2}{(n+p)!(n-p)!}. \quad (2.10)$$

If we now assume a Lorentz distribution of the excitability parameters,

$$g(\eta|\mathbf{k}) = \frac{1}{\pi} \frac{\Delta(\mathbf{k})}{[\eta - \eta_0(\mathbf{k})]^2 + \Delta^2(\mathbf{k})}, \quad (2.11)$$

we obtain

$$\int \int f(\theta', \eta'|\mathbf{k}, t) e^{ip\theta} d\theta' d\eta' = \begin{cases} \hat{b}(\mathbf{k}, t)^p, & p > 0 \\ 1, & p = 0 \\ \hat{b}^*(\mathbf{k}, t)^{|p|}, & p < 0, \end{cases} \quad (2.12)$$

with $\hat{b}(\mathbf{k}, t) \equiv b(\eta_0(\mathbf{k}) + i\Delta(\mathbf{k}), \mathbf{k}, t)$. This now allows us to rewrite v_θ in terms of $\hat{b}(\mathbf{k}, t)$ as

$$v_\theta = g e^{i\theta} + h + g^* e^{-i\theta}, \quad (2.13)$$

where

$$g = -\frac{1}{2}\left(1 - \eta - \frac{K}{\langle k \rangle} H_n(\mathbf{k}, t)\right), \quad h = 1 + \eta + \frac{K}{\langle k \rangle} H_n(\mathbf{k}, t), \quad (2.14)$$

and

$$H_n(\mathbf{k}, t) = \sum_{\mathbf{k}'} \left\{ P(\mathbf{k}') a(\mathbf{k}' \rightarrow \mathbf{k}) \times \left[A_0 + \sum_{p=1}^n A_p (\hat{b}(\mathbf{k}', t)^p + \hat{b}^*(\mathbf{k}', t)^p) \right] \right\}. \quad (2.15)$$

Substituting the phase velocity Eq. (2.13) and the Ott-Antonsen ansatz Eq. (2.8) into the continuity equation (2.6), we find that $b(\eta, \mathbf{k}, t)$ satisfies:

$$\frac{\partial b}{\partial t} = i(gb^2 + hb + g^*). \quad (2.16)$$

Inserting the forms for g and h from Eq. (2.14) and (2.15) into this expression, and evaluating each quantity at the pole, $\eta = \eta_0(\mathbf{k}) + i\Delta(\mathbf{k})$, we obtain a reduced system of equations for $\hat{b}(\mathbf{k}, t)$ describing the mean field dynamics of the neuronal network,

$$\begin{aligned} \frac{\partial \hat{b}(\mathbf{k}, t)}{\partial t} = & -i \frac{(\hat{b}(\mathbf{k}, t) - 1)^2}{2} \\ & + \frac{(\hat{b}(\mathbf{k}, t) + 1)^2}{2} \left\{ -\Delta(\mathbf{k}) + i\eta_0(\mathbf{k}) + i \frac{K}{\langle k \rangle} \sum_{\mathbf{k}'} P(\mathbf{k}') a(\mathbf{k}' \rightarrow \mathbf{k}) \right. \\ & \left. \times \left[A_0 + \sum_{p=1}^n A_p (\hat{b}(\mathbf{k}', t)^p + \hat{b}^*(\mathbf{k}', t)^p) \right] \right\}. \end{aligned} \quad (2.17)$$

The mean field order parameter, $\bar{R}(t)$ can now be written in terms of $\hat{b}(\mathbf{k}, t)$. Using the assumed form for $f(\theta, \eta|\mathbf{k}, t)$, we can evaluate the integrals in Eq. (2.5) using

Cauchy's residue theorem to obtain

$$\bar{R}(t) = \frac{1}{N} \sum_{\mathbf{k}} P(\mathbf{k}) \hat{b}(\mathbf{k}, t). \quad (2.18)$$

For the discussion in this chapter, we will restrict the assortativity function to be of the form used previously by Restrepo and Ott [47]

$$a(\mathbf{k}' \rightarrow \mathbf{k}) = h(a_{\mathbf{k}' \rightarrow \mathbf{k}}), \quad (2.19)$$

where $h(x) = \min(\max(x, 0), 1)$ is defined to ensure that $a(\mathbf{k}' \rightarrow \mathbf{k})$ is a valid probability (i.e. $0 \leq a(\mathbf{k}' \rightarrow \mathbf{k}) \leq 1$), and

$$a_{\mathbf{k}' \rightarrow \mathbf{k}} = \frac{k'_{out} k_{in}}{N \langle k \rangle} \left[1 + c \left(\frac{k'_{in} - \langle k \rangle}{k'_{out}} \right) \left(\frac{k_{out} - \langle k \rangle}{k_{in}} \right) \right], \quad (2.20)$$

where c is a parameter used to vary the network assortativity (with $c > 0$ and $c < 0$ corresponding to assortative and disassortative networks, respectively). In networks with neutral assortativity ($c = 0$), the probability of forming a link between two nodes is simply proportional to the out-degree of the source node and the in-degree of the target node.

The in-out Pearson assortativity coefficient, r , is a statistic used to characterize the overall assortativity of a network, and is defined [64] as

$$r = \frac{\sum_e [(k'_{in} - \langle k \rangle)(k_{out} - \langle k \rangle)]}{\sqrt{\sum_e (k'_{in} - \langle k \rangle)^2} \sqrt{\sum_e (k_{out} - \langle k \rangle)^2}}, \quad (2.21)$$

where \sum_e is the sum over all edges connecting a node of degree \mathbf{k}' to a node of degree \mathbf{k} .² Assuming that $a(\mathbf{k}' \rightarrow \mathbf{k}) = a_{\mathbf{k}' \rightarrow \mathbf{k}}$, and that the in and out degree distributions are independent, we can relate the assortativity coefficient to the parameter c as

$$r = \frac{c}{\langle k \rangle^2} \sqrt{(\langle k_{in}^2 \rangle - \langle k \rangle^2)(\langle k_{out}^2 \rangle - \langle k \rangle^2)}, \quad (2.22)$$

which can be seen by noting that the sum of a quantity $Q(\mathbf{k}, \mathbf{k}')$, defined on each edge connecting a node of degree \mathbf{k}' to a node of degree \mathbf{k} , over edges in our mean field formulation would be given by $\sum_e Q(\mathbf{k}, \mathbf{k}') = \sum_{\mathbf{k}} \sum_{\mathbf{k}'} P(\mathbf{k}') a(\mathbf{k}' \rightarrow \mathbf{k}) P(\mathbf{k}) Q(\mathbf{k}, \mathbf{k}')$.

The expression for the assortativity coefficient as a function of c , Eq. (2.22), is unbounded, while the Pearson assortativity is by definition bounded between -1 and 1 . This difference arises because, for sufficiently large c , the assortativity function given in Eq. (2.20) is not a probability. However, for the network parameters used in our numerical example below, we find that Eq. (2.22) is very accurate for $|c| \leq 2.5$, corresponding to an assortativity range, $|r| \lesssim 0.198$.

If we assume the excitability parameters are drawn from a degree independent distribution ($g(\eta|\mathbf{k}) \equiv g(\eta)$) and the \hat{b} 's are given \mathbf{k} independent identical initial conditions, $\hat{b}(\mathbf{k}, 0) \equiv \hat{b}(0)$, then there are a few notable cases in which particular degree distributions and our chosen assortativity function Eq. (2.20) allow for further dimensional reduction. For networks with a delta-function degree distribution, $P(\mathbf{k}) = \delta_{k_{in}, k} \delta_{k_{out}, k}$, the Eq. (2.17) reduces to a single equation describing the mean field dynamics,

²For another, often useful, definition of a coefficient quantitatively characterizing the assortativity or disassortativity of a network see Ref. [65]

$$\frac{\partial \hat{b}(t)}{\partial t} = -i \frac{(\hat{b}(t) - 1)^2}{2} + \frac{(\hat{b}(t) + 1)^2}{2} \left\{ -\Delta + i\eta_0 + iK \left[A_0 + \sum_{p=1}^n A_p (\hat{b}(t)^p + \hat{b}^*(t)^p) \right] \right\}. \quad (2.23)$$

We note that this equation is identical to earlier results for a fully connected network [22]. Thus, networks with only a single allowed degree have identical asymptotic dynamics to a fully connected network. This result is consistent with analogous results by Barlev et al [49] for a network of Kuramoto oscillators. More generally, if the network has fixed in-degree, $P(\mathbf{k}) = P(k_{out})\delta_{k_{in},k}$, the system is similarly reduced to the single dynamical equation, Eq. (2.23). On the other hand, if the out-degree is fixed, $P(\mathbf{k}) = P(k_{in})\delta_{k_{out},k}$, then dynamics of $\hat{b}(\mathbf{k}, t)$ is independent of k_{out} , further reducing the dimensionality of the problem.

Reduction efficiency

Equation (2.17) represents a reduction of the original system of N theta neurons to a system with as many equations as there are \mathbf{k} values in the support of the degree distribution $P(\mathbf{k})$. We denote this quantity by $M_{\mathbf{k}}$, which, in the case of independent in and out-degree distributions, is equal to $M_{in} \times M_{out}$, where M_{in} and M_{out} are the number of possible in-degrees and out-degrees respectively. In general, simulating the full network, Eq. (2.2), requires $\mathcal{O}(N^2)$ floating point operations per time step. Using the form of the assortativity function given in Eq. (2.20) the sum over \mathbf{k}' in the reduced system of equations can be split into two sums, each independent of \mathbf{k} ,

$$\frac{k_{in}}{N\langle k \rangle} \sum_{\mathbf{k}'} P(\mathbf{k}') k'_{out} \mathcal{A} + c \frac{k_{out} - \langle k \rangle}{N\langle k \rangle} \sum_{\mathbf{k}'} P(\mathbf{k}') (k'_{in} - \langle k \rangle) \mathcal{A}. \quad (2.24)$$

where $\mathcal{A} = A_0 + \sum_{p=1}^n A_p \left(\hat{b}(\mathbf{k}', t)^p + \hat{b}^*(\mathbf{k}', t)^p \right)$. Since the two sums in Eq. (2.24) are independent of \mathbf{k} , each must be calculated only once per simulation iteration. Thus, simulating the reduced system Eq. (2.17) only requires $\mathcal{O}(M_{\mathbf{k}})$ floating point operations per time step — $M_{\mathbf{k}}$ operations performed once for each of these two sums and $M_{\mathbf{k}}$ operations for each of the $\hat{b}(\mathbf{k}, t)$ equations. In many cases, $M_{\mathbf{k}} \ll N^2$, so that simulating Eq. (2.17) is significantly more efficient than simulating the full network. Furthermore, if c is set to 0, which is the case of networks with neutral assortativity, then $\hat{b}(\mathbf{k}, t)$ will have no dependence on k_{out} , and hence the overall problem is reduced to M_{in} independent equations, allowing even greater computational efficiency.

Since $\hat{b}(\mathbf{k}', t)$, $P(\mathbf{k}')$, and $a(\mathbf{k}' \rightarrow \mathbf{k})$ are each smoothly varying functions, we can achieve further dimensional reduction by interpolating the summand in Eq. (2.17) using a coarse-grained grid of \mathbf{k} values. In particular, Eq. (2.17) is not solved for $\hat{b}(\mathbf{k}, t)$ for all of the $M_{\mathbf{k}}$ values of \mathbf{k} , but only for the small subset of \mathbf{k} values that lie on the coarse-grained grid in \mathbf{k} -space. The summands on the right hand side of Eq. (2.17) at \mathbf{k} values not on the grid are approximated by a bilinear interpolation of the values at the surrounding chosen \mathbf{k} values. To perform the bilinear interpolation, we first interpolate linearly between neighboring grid values in one direction. The value of the summand at a given \mathbf{k} value is then approximated by linearly interpolating in the other direction between values estimated with the

previous linear interpolation. We find that using as few as 10% of the network degrees yield very accurate results, while an even coarser interpolation still produces the same qualitative behavior as can be seen in Fig. 2.2.

2.5 Numerical simulations and results

In the following examples, we consider a directed network of $N = 5000$ nodes, with in and out degrees chosen from independent, identical highly skewed distributions. In particular, we use a truncated power law distribution given by

$$P(k) = \begin{cases} 0 & \text{if } k < k_{min} \\ Ak^{-\gamma} & \text{if } k_{min} \leq k < k_{max} \\ 0 & \text{if } k_{max} \leq k. \end{cases} \quad (2.25)$$

The exponent of the power law component, γ , was set to 3, and k_{min} and k_{max} were set to 750 and 2000, respectively. As mentioned earlier, the normalization constant A is chosen to make $\sum_{\mathbf{k}} P(\mathbf{k}) = N$. We will also set the parameter n controlling the sharpness of the synaptic pulse to 2 for all examples considered, and will use an interpolation level of 10% for all calculations using the reduced system of equations for the mean field theory (cf. Fig. 2.2).

From numerical simulations of the reduced equations, (2.17), we find that the long term dynamics of the order parameter can be broadly classified into one of three phases – (1) the partially resting (PR) phase; (2) the asynchronously firing (AF) phase; and (3) the synchronously firing (SF) phase. The PR phase and the

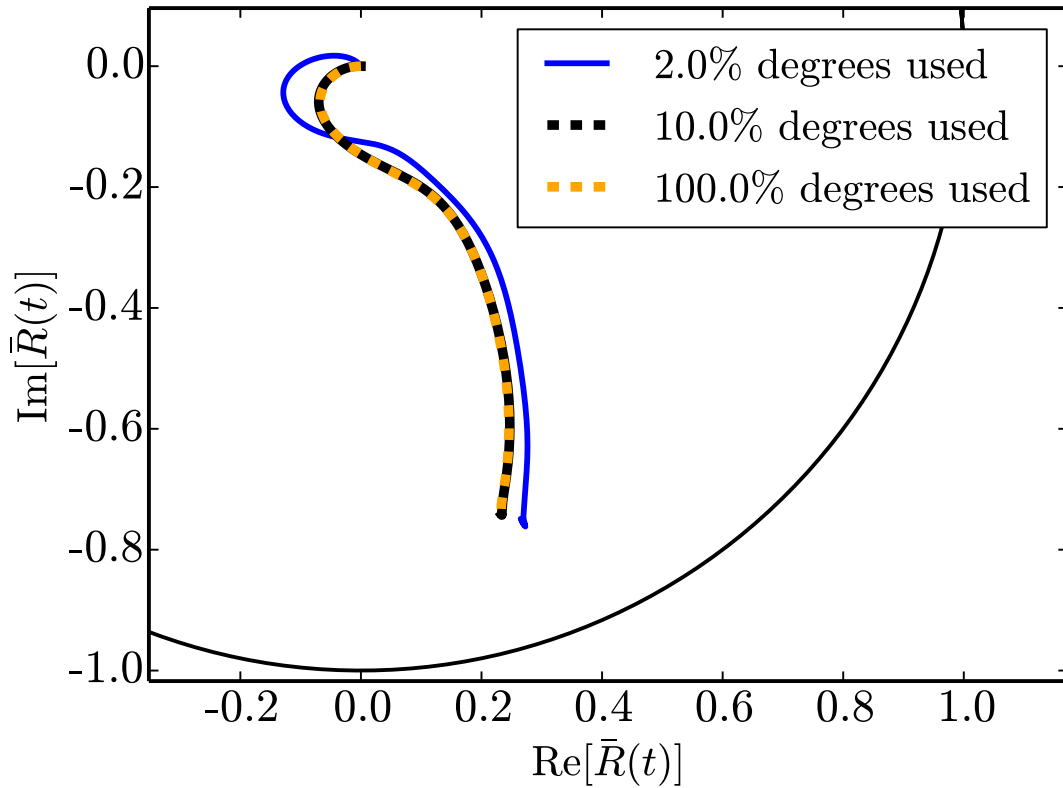


Figure 2.2: The effect of varying levels of interpolation on the calculated results for the trajectories of $\bar{R}(t)$ in the complex plane starting from an initial condition of $\bar{R}(t) = 0$ and ending at a fixed point attractor for $K = 3$ in a network with neutral assortativity, with $\eta_0 = -2$ and $\Delta = 0.1$. Calculation of the order parameter dynamics is robust to a large range in the level of interpolation. Using as few as 10% of the total available degrees and interpolating the remaining 90% give results close to the calculation without interpolation. In the rest of this chapter we employ a 10% interpolation level in all our mean field calculations. The black arc is a segment of the unit circle $|\bar{R}(t)| = 1$.

AF phase appear as fixed points in the dynamics of the order parameter, whereas the SF phase appears as a limit cycle of the order parameter.

2.5.1 Fixed points

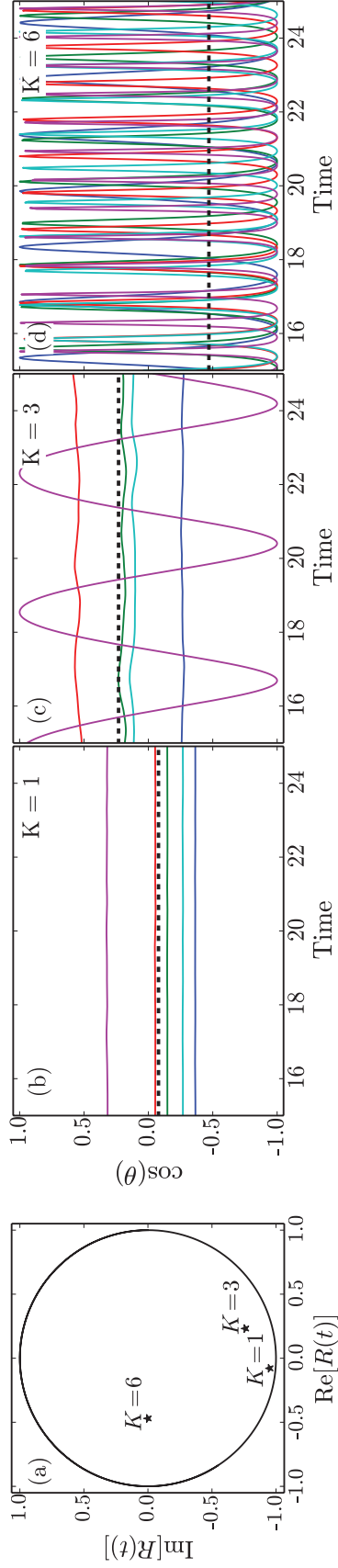


Figure 2.3: (a): Fixed points of $R(t)$ observed in networks with neutral assortativity, $\eta_0 = -2$ and $\Delta = 0.1$, for three values of the coupling strength K . Fixed points in the PR state ($K = 1$) and the AF state ($K = 6$) are marked in the complex plane. The fixed point at an intermediate value of K is also marked. (b), (c), (d): Time series of the cosine of the phase of 5 randomly chosen neurons demonstrates that in the PR phase almost all neurons are in a resting state, and as the system approaches the AF state, more nodes transition to an oscillating, excited state. The thick dashed line corresponds to the position of the fixed point of the order parameter for the corresponding value of K .

As a particular example to illustrate the different types of fixed points, we look at a network with neutral assortativity ($c = 0$) having excitability parameters distributed according to a Lorentzian distribution with mean $\eta_0 = -2$ and width $\Delta = 0.1$ (Fig. 2.3).

When the network is in the PR phase, the order parameter goes to a fixed point that lies near the edge of the unit circle $|\bar{R}| = 1$. In this phase, most of the individual neurons in the network are independently in their resting states, in a fashion similar to Fig. 2.1(a). This corresponds to the case of $K = 1$ in Fig. 2.3(a), in which the fixed point is located near the edge of the unit circle marked in black. Further, the time series of a few randomly chosen neurons (Fig. 2.3(b)) demonstrates that almost all of the neurons are in a resting state. While there may be a small number of neurons that are in the spiking phase due to the spread in the distribution of values of excitability parameters, η , these do not have any significant effect on the full order parameter of the system.

As we increase the coupling constant K , the system transitions to the asynchronously firing (AF) phase, in which the order parameter goes to a fixed point located near the center of the unit circle. In this phase, most of the individual neurons in the network are asynchronously firing, in a fashion similar to Fig. 2.1(c). This can be seen in the case of $K = 6$ in Fig. 2.3(c) which shows that almost all of the neurons are in a recurrent spiking state. Note that even though the neurons are spiking *asynchronously*, i.e., their firing times are independent of one another,³

³this definition of asynchronous spiking is consistent with remarks by other authors [66, 67], wherein asynchronous states have been defined as states in which at each neuron the term coupling it to the other neurons in the network is independent of time, as is observed in the cases of fixed points.

the fixed point of the order parameter is not at $\bar{R} = 0$. This is because the angular velocity of an individual neuron is not constant along the circle, thus in the average over the ensemble of neurons a bias is present towards the direction for which the angular velocity of neurons is minimized. As discussed in Sec. 5.2, this may occur at either $\theta = 0$ or at $\theta = \pi$, dependent on how large the excitability parameter is for the neuron.

We now examine the transition from the PR phase to the AF phase. Microscopically, in the PR phase, almost all of the neurons are individually in a resting phase, whereas in the AF phase almost all neurons are in the spiking state. To examine the behavior at an intermediate point, we look at the fixed point for the case of $K = 3$, as shown in Fig. 2.3(c). At this intermediate value of the coupling constant, a fraction of the neurons are in the spiking state. In particular, the nodes that begin to spike first are those which have larger in-degrees. This is demonstrated in Fig. 2.4, in which we examine $\hat{b}(\mathbf{k})$ at the fixed point for $K = 3$. Since we are looking at a network with neutral assortativity ($c = 0$), Eq. (2.24) implies that the sum only depends on the out-degree through a common multiplicative factor. Thus \hat{b} is only plotted as a function of k_{in} . Analogously, for the fixed point of the dynamics on the full network, the range of degrees from k_{min} to k_{max} is divided uniformly into several intervals, and for each interval we find a partial order parameter, calculated such that the average in Eq. (2.4) is only performed over those nodes

whose in-degree lie within that interval, i.e.,

$$R(k_{in}, t) = \frac{1}{||\mathcal{N}||} \sum_{j \in \mathcal{N}} e^{i\theta_j}, \quad (2.26)$$

where \mathcal{N} is the set of nodes having an in-degree within one of the intervals of the range of degrees, $||\mathcal{N}||$ is the number of nodes in the set, and k_{in} is the average in-degree of nodes within that set.

In addition, we find that the transition from the PR phase to the AF phase occurs via a hysteretic process mediated by saddle node bifurcations. To illustrate this, we evolved the dynamics of the full network in a step wise fashion by increasing the coupling constant K in small increments of 0.2, and allowing the system to relax to an equilibrium before the next increment (Fig. 2.5(a)). We also compare this with the analogous hysteresis curve observed for the evolution of the system dynamics on an Erdős-Rényi network having the same size and average degree as the highly skewed degree distribution being considered (Fig. 2.5(b)). While the hysteretic region begins at around the same value of the coupling constant, K , for both network topologies, we find that for the case of the Erdős-Rényi network, which has a sharply peaked degree distribution, the range in K that allows hysteresis ($3 \lesssim K \lesssim 7.25$) is significantly larger than the corresponding range for the network with the highly skewed degree distribution ($3.25 \lesssim K \lesssim 4$).

To compare with the simulation of the dynamics on the full network, we also calculate the fixed points of the mean field equations Eq. (2.17). While the fixed points cannot be readily determined analytically, we can efficiently compute them

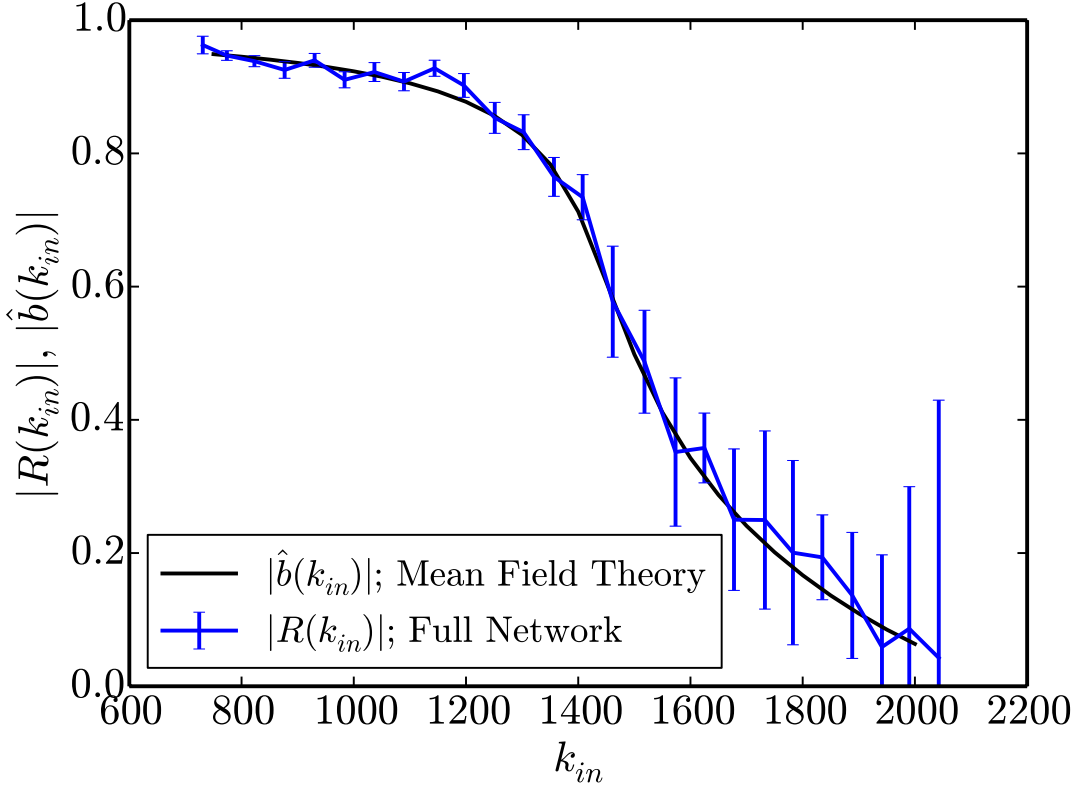


Figure 2.4: Comparison of $|\hat{b}(k_{in})|$ from the reduced system of equations and the time average of $|R(k_{in})|$ from the full system, Eq. (2.26), for a network with neutral assortativity ($c = 0$), $\eta_0 = -2$, and $\Delta = 0.1$ at $K = 3$. The dynamics under these parameters were simulated in a network with 5000 nodes, and the network was allowed to relax to a fixed point. Nodes were divided into classes according to their in-degree to calculate the time averaged effective order parameter for each class, which is shown in blue, with the error bars denoting the root mean squared time fluctuation of the order parameter for that class. The time fluctuations are due to the finite number of nodes in each class. (See text for details.)

via a numerical calculation. Setting $\partial \hat{b}(\mathbf{k}, t)/\partial t = 0$ for the fixed points, we find that the equilibrium $\hat{b}(\mathbf{k})$ satisfy,

$$\hat{b}_{\pm}(\mathbf{k}) = \frac{1 \pm z(\mathbf{k})}{1 \mp z(\mathbf{k})}, \quad (2.27)$$

where

$$iz^2(\mathbf{k}) = -\Delta + i\eta_0 + i \frac{K}{\langle k \rangle} \sum_{\mathbf{k}'} P(\mathbf{k}') a(\mathbf{k}' \rightarrow \mathbf{k}) \times \left[A_0 + \sum_{p=1}^n A_p (\hat{b}(\mathbf{k}', t)^p + \hat{b}^*(\mathbf{k}', t)^p) \right], \quad (2.28)$$

and the sign is chosen to ensure $|\hat{b}(\mathbf{k})| \leq 1$. Using our form of the assortativity function Eq. (2.20), we may again split the above sum into two parts as in Eq. (2.24). Thus we may rewrite Eq. (2.28) as

$$iz^2(\mathbf{k}) = -\Delta + i\eta_0 + ik_{in}X + i(k_{out} - \langle k \rangle)Y, \quad (2.29)$$

where X and Y are given by,

$$X = \frac{K}{N\langle k \rangle^2} \sum_{\mathbf{k}'} P(\mathbf{k}') k'_{out} \left[A_0 + \sum_{p=1}^n A_p (\hat{b}(\mathbf{k}', t)^p + \hat{b}^*(\mathbf{k}', t)^p) \right] \quad (2.30a)$$

$$Y = \frac{K}{N\langle k \rangle^2} \sum_{\mathbf{k}'} P(\mathbf{k}') (k'_{in} - \langle k \rangle) \left[A_0 + \sum_{p=1}^n A_p (\hat{b}(\mathbf{k}', t)^p + \hat{b}^*(\mathbf{k}', t)^p) \right]. \quad (2.30b)$$

These simplifications allow for efficient calculation of the system fixed points. Choosing initial values, X_0 and Y_0 , we calculate the associated $z(\mathbf{k})$ and $\hat{b}(\mathbf{k})$ using Eq. (2.29) and Eq. (2.27), and then recalculate new values, X_1 and Y_1 using Eq. (2.30). For fixed points of the reduced equations $\delta X = X_1 - X_0$ and $\delta Y = Y_1 - Y_0$ are

both zero. We calculate δX and δY for several different initial values at regularly spaced intervals for X_0 and Y_0 , and identify the fixed points as the points where $\delta X = \delta Y = 0$. The interpolation procedure described earlier can also be applied to this calculation to further increase efficiency. For the nonassortative case ($c = 0$), $Y = 0$ always, so identifying the fixed points in this case only requires calculating the variation in the single parameter X . We use this method to evaluate the fixed points of the reduced equations for the range of K over which hysteresis was observed, and find close agreement between the results of this fixed point analysis and the direct evolution of the full network (Fig. 2.5).

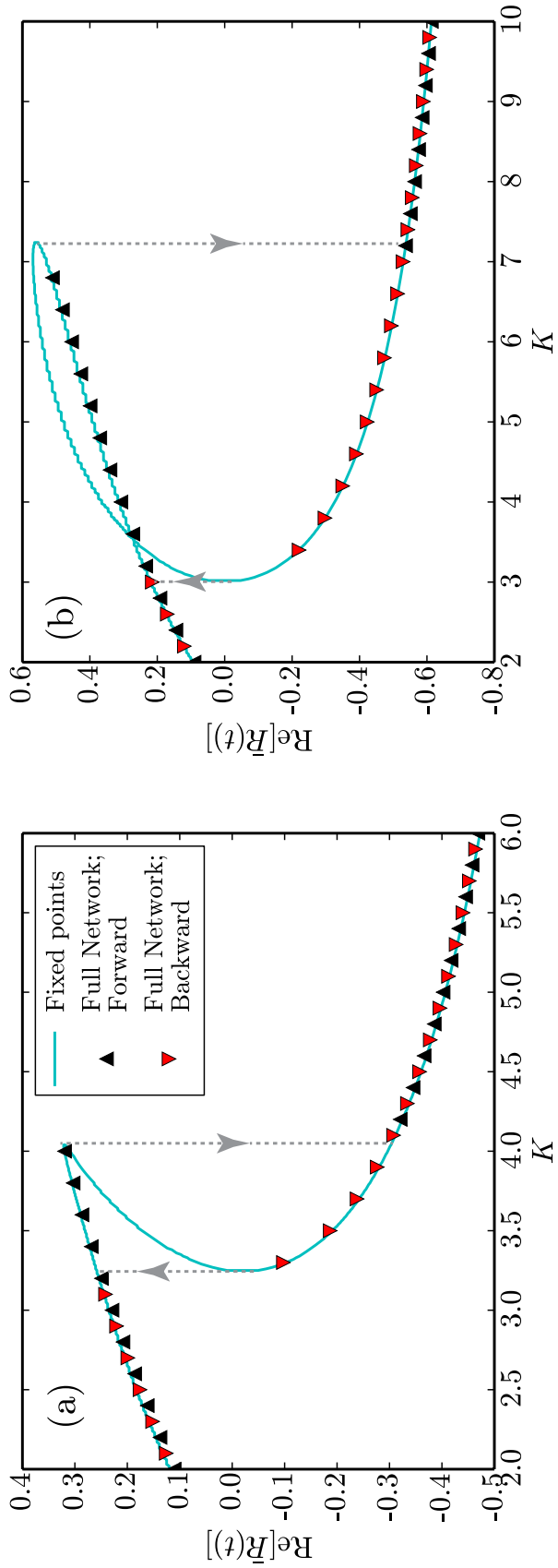


Figure 2.5: A sweeping value of K was used to observe the change in phase from the PR state to the AF state. Hysteresis was observed on the network with a highly skewed degree distribution (a) as well as a corresponding Erdős-Rényi network having the same size and the same average degree (b). For the full network, at each value of K the mean of the order parameter after ignoring the transients have been marked as triangles. A close match is observed with the fixed points as computed from mean field equations directly (see text for details). Hysteresis is observed for $3.25 \lesssim K \lesssim 4$ in the network with the highly skewed degree distribution (a), and is observed for $3 \lesssim K \lesssim 7.25$ in the corresponding Erdős-Rényi network (Note the difference in scales for the x-axis in both plots). An apparent crossing of the fixed point curve is seen in (b), which is an artifact of the non-self-intersecting \bar{R} curve lying in the two dimensional complex space, which has been projected onto the real axis in this plot.

2.5.2 Limit Cycles

As a representative example of limit cycles of $\bar{R}(t)$, we consider a network with neutral assortativity with excitability parameters η distributed as a Lorentzian with mean $\eta_0 = 10.75$ and width $\Delta = 0.5$, and with a coupling constant $K = -9$. In the SF phase, the order parameter goes to a limit cycle in the complex plane. In this phase, a majority of the neurons are synchronously in a spiking state. Plots for such limit cycles are shown in Fig. 2.6, in which we plot the trajectory of the order parameter in the complex plane (after removing transients) for a network with the highly skewed degree distribution given in Eq. (2.25) (blue solid curve), a corresponding Erdős-Rényi network having a Poissonian degree distribution (green dashed curve), and a regular network having a delta function degree distribution (i.e. $P(\mathbf{k}) = \delta_{k_{in},k} \delta_{k_{out},k}$) (red dotted curve), each having the same average degree of 1090. As seen earlier in Eq. (2.23), a network with a delta function degree distribution has mean field dynamics identical to those of a fully connected network, and the corresponding limit cycle in Fig. 2.6 is identical to the limit cycle obtained at these parameters for the fully connected network by Luke et al. [22] In comparison with the limit cycles that are observed for the case of the regular network or the Erdős-Rényi network, the limit cycles in networks with highly skewed degree distributions were diminished in size, due to the large variation in nodal behavior as a function of degree. Nodes with smaller in-degrees were observed to predominantly be in the spiking phase, with high synchronization and a larger limit cycle for the partial order parameter, whereas nodes with larger in-degrees were in the resting phase. Due

to this differentiation of behavior with degree, the averaged full order parameter exhibits a limit cycle that is somewhat reduced in size when compared with the results for a fully connected network by Luke et al [22]. However, we see that the limit cycles for the Erdős-Rényi network are similar in shape and structure to the limit cycles obtained for the regular network, as would be expected in accordance with the discussion in Sec. 2.4, since the Poissonian degree distribution for the Erdős-Rényi network is sharply peaked about the average degree and hence cannot admit a large variation of behavior with nodal degree. As the average degree, $\langle k \rangle$ increases, the red and green curves converge because the Poisson degree distribution appropriate for an Erdős-Rényi network approaches a delta function.

2.5.3 Effect of Assortativity

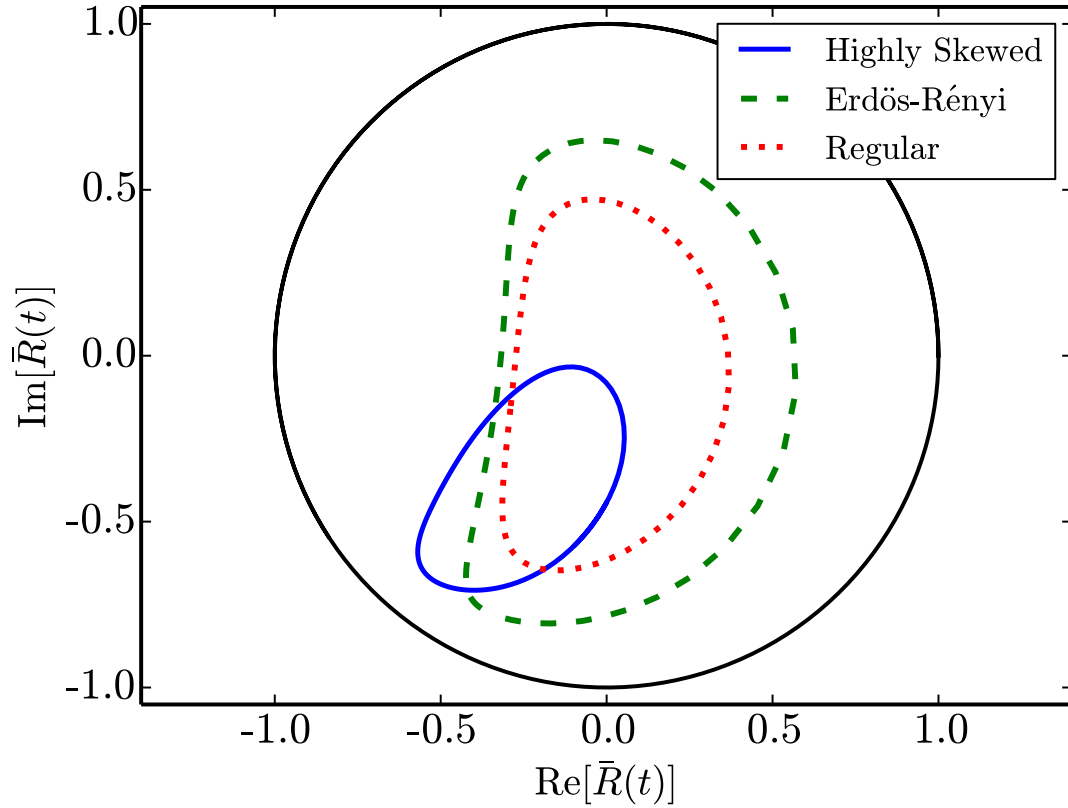


Figure 2.6: Comparison of the limit cycle attractor for $\bar{R}(t)$ in the complex plane across varying degree distributions in a network with neutral assortativity ($c = 0$) with $\eta_0 = 10.75$, $\Delta = 0.5$ and $K = -9$. The highly skewed network (blue solid curve) has a degree distribution according to Eq. (2.25), the Erdős-Rényi network (green dashed curve) has a Poissonian degree distribution, and the regular network (red dotted curve) has a delta function degree distribution. The black circle is the unit circle $|\bar{R}|=1$

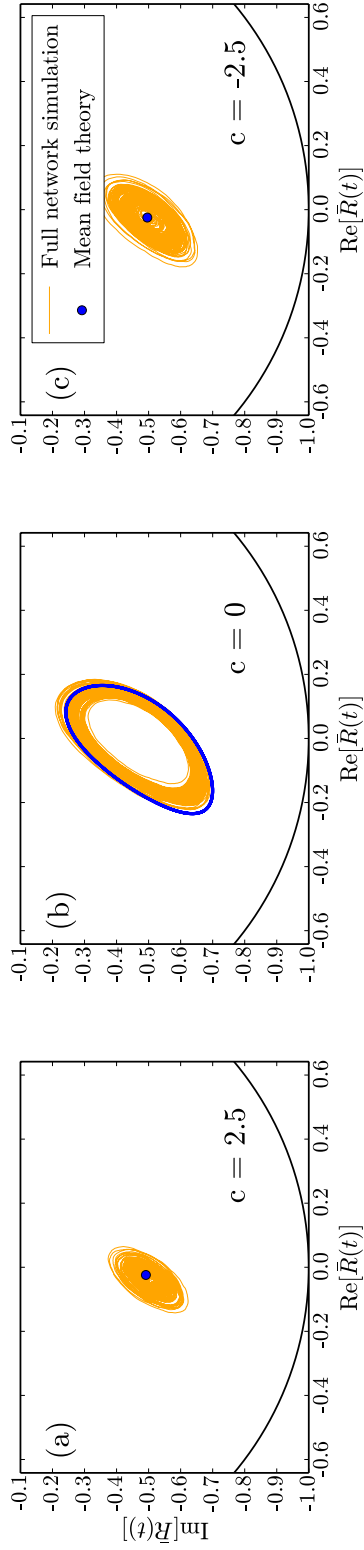


Figure 2.7: For the parameters $\eta_0 = 4$, $\Delta = 0.5$ and $K = -4.8$, in a network with neutral assortativity ($c = 0$), the system lies in an SF state (as in (b)). Varying the assortativity in either direction ($c = \pm 2.5$, corresponding to $r \approx \pm 0.198$) causes the limit cycles to be replaced by a fixed point instead (as in (a),(c)). The behavior predicted by the mean field theory is in agreement with the simulations of the full network.

We now consider the effect of assortativity on the limit cycle dynamics of the order parameter in the network. While limit cycle behavior exists in networks with neutral assortativity ($c = 0$), introduction of assortativity or disassortativity in the network can cause the limit cycle attractor to transform to a fixed point attractor (AF like state) via a Hopf bifurcation. This is demonstrated in Fig. 2.7, in which we show that varying c away from zero to ± 2.5 (corresponding to Pearson assortativity coefficients of $r \approx \pm 0.198$) is sufficient to cause the Hopf bifurcation and send the system to a fixed point attractor. The fixed points for the order parameters in these networks exhibit relatively large amounts of finite N induced noise as seen from the size of the clouds surrounding the fixed point position calculated from the reduced system.

2.6 Conclusion

Using a mean field approximation, in conjunction with the Ott-Antonsen ansatz, we obtained a reduced system of equations that successfully model the macroscopic order parameter dynamics of a large network of theta neurons. This reduced system of equations allows us to examine the effects of varying the network parameters and the network topology (in terms of degree distributions, as well as degree correlations) in a computationally efficient fashion. The order parameter of the network is used for describing the macroscopic behavior of the network of theta neurons, whose attractors can be of various types. In particular, we find resting states, asynchronously firing states and synchronously firing states, the first two of

which appear as a fixed point for the order parameter (Fig. 2.3), while the third appears as a limit cycle for the order parameter (Fig. 2.6). We also used the reduced system of equations to observe the effect of varying the assortativity in the system and demonstrated that a synchronously firing phase was only present for networks with neutral or small assortativity, and the addition of moderate amounts of assortativity or disassortativity to the network causes the system to go to an asynchronously firing state instead (Fig. 2.7). Further, for networks with highly skewed degree distributions, we find that nodes with different values of their degrees admit a large variation of behavior (Fig. 2.4), a phenomenon not possible in networks with all-to-all connectivity. In all cases close agreement was observed between the order parameter dynamics as predicted by the reduced system of equations (Eq. 2.17), and as calculated by evolution of the full system of equations Eq. (2.2).

Chapter 3: Continuous versus Discontinuous Transitions in the D -Dimensional Generalized Kuramoto Model: Odd D is Different

3.1 Introduction

3.1.1 Background

Collective behavior in large populations of interacting elements has been a subject of intense study in physical, social, biological and technological systems [10, 11, 39, 40, 43, 44, 68–70]. An important, frequently encountered example is the case of interacting phase oscillators, i.e., coupling between elements whose state is characterized by a point on a unit circle. In 1967 Winfree first systematically studied the dynamics of a population of weakly coupled phase oscillators [1]. A few years later [2], Kuramoto presented a simplified version of the Winfree model which he solved in the limit of $N \rightarrow \infty$, where N is the number of oscillators. This model, now known as the Kuramoto model, is

$$\frac{d\theta_i}{dt} = \omega_i + \frac{K}{N} \sum_{j=1}^N \sin(\theta_j - \theta_i), \quad (3.1)$$

where θ_i represents the phase angle of the i^{th} oscillator, ω_i is its natural frequency of oscillation (which we will also refer to as the natural rotation), and K is the coupling strength between oscillators. Typically the ω_i are chosen randomly from some unimodal distribution with a finite spread Δ , and $N \gg 1$ (the case of interest in this chapter) is often considered. In the $N \rightarrow \infty$ limit Kuramoto was able to show the presence of a continuous phase transition between asynchronous and partially synchronous states of the system [2, 3].

The Kuramoto model and its generalizations have since been used to study synchronization behavior in a wide variety of systems, modeling biological problems such as the behavior of cardiac pacemaker cells [4], synchronization in large groups of flashing fireflies [5, 6], circadian rhythms [7, 8], and neuronal synchronization [9], as well as problems in physics and engineering such as synchronization of power-grid networks [10, 11], superconducting Josephson junctions [12], atomic physics [13], and neutrino oscillation [14], among others. Another class of applications of the Kuramoto model has been modeling the alignment of unit vectors representing the direction of motion of interacting members of a swarm or flock of moving agents in two dimensions [31–33]. Alternately, one can think of such unit vectors as characterizing the opinion of an individual in a group of interacting individuals [71]. In this later case, alignment of unit vectors can be viewed as modeling the evolution toward social consensus.

The aforementioned studies all describe the alignment of agents via a single scalar variable θ_i , which characterizes the alignment state of the individual coupled units. However, for several of the above cited applications alignment in higher-

dimensional spaces is important, and this is the subject of this chapter. For example, the problem of alignment of velocity vectors in a flock of birds, a school of fish, or a swarm of flying drones is more realistically set up in three-dimensional space, whereas the alignment of opinion dynamics of a population could in general be multidimensional depending on the characteristics of the opinions considered. With such examples in mind, Olfati-Saber [71] introduced a higher-dimensional generalization of the Kuramoto model without the presence of any individual natural rotation [analogous to the ω_i term in Eq. (4.1)]. (In 2013, Zhu [72] considered the equivalent case of identical natural rotations for each agent.) The choice of the generalization in Refs. [71, 72] maintains the form of the coupling between two agents in all dimensions, i.e., in D dimensions the state of each agent is taken to be a D -dimensional unit vector, and the coupling between two agents is proportional to the sine of the angle between their unit vectors¹. Network characteristics leading to complete alignment were discussed; however, no complete stability analysis of the system was presented. In this chapter we consider globally coupled systems, with a spread of the individual natural rotations of each unit, which follows from the generalization of the spread in the natural frequencies of the standard Kuramoto model. These natural rotations act as constant biases to the states of the agents. In particular, for a given swarming agent, the natural rotation term can be thought of as a systematic error in the dynamics of the agent, which causes the agent to drift away from traveling in purely a straight line. We motivate the form natural rotation

¹For generalizations of the Kuramoto model wherein agent states are represented by elements of a Lie group, see Refs. [73, 74].

term in the context of flocking and swarming in $D = 3$ in Sec. 3.4. In assuming these natural rotations we set up a model more general than the one that has been studied by previous authors, leading to new and interesting results.

3.1.2 Main Result

A key point in this chapter is the remarkable difference between the standard two-dimensional Kuramoto model and its generalizations to 3 dimensions (and also to odd values of $D \geq 5$). A striking example of this is the nature of the transition from the incoherent state to the partially aligned state. As previously noted, the two-dimensional Kuramoto model, in the limit of infinite system size, was shown by Kuramoto [2,3] to exhibit a continuous phase transition to coherence with increasing coupling strength K . This is represented by the dashed curve in Fig. 3.1, where the horizontal axis is the coupling strength, K , and the vertical axis represents the ‘order parameter’ [Sec. 3.2, defined in Eq. (3.5)], which is a measure of the coherence (or degree of synchronization). The exact shape of this curve can be derived analytically [16], and it can be shown that this phase transition to synchrony is effectively a low-dimensional bifurcation [18]. The three-dimensional Kuramoto model, on the other hand, exhibits a *discontinuous phase transition as we increase the coupling strength through zero* (solid curve in Fig. 3.1): For negative values of the coupling strength (indicative of repulsive interactions between agents), the agents tend to a completely incoherent state (defined by an ‘order parameter’ with zero magnitude), and as we increase the coupling strength through zero, there is a

discontinuous jump of the coherence as measured by the order parameter. Further, we find that this discontinuous phase transition occurs nonhysteretically.

3.1.3 Relation to Statistical Physics Models

It is interesting to note that if the time-independent frequencies ω_i in Eq. (4.1) are replaced by independent, zero-mean, white noise of uniform strength, then the statistical equilibria and phase transitions of the Kuramoto model are the same as those of the mean-field classical XY model, which describes the interactions of classical two-dimensional spins with global coupling [27–30]. In this case, the strength of the white noise corresponds to the temperature, and the magnitude of the coherence corresponds to the magnetization. Thus the Kuramoto model can be thought of as the mean-field XY model with thermal noise replaced by quenched randomness (the randomly chosen time-independent frequencies ω_i). Specifically, the mean-field XY model and the Kuramoto model yield similar behavior [9, 28] in that they both show a continuous (‘second order’) transition as the coupling constant increases through a critical value $K_c > 0$ (which, for the Kuramoto model, increases with the spread Δ in the distribution of the natural frequencies, while, for the XY model, K_c increases with temperature). A surprising result of this chapter is that, when these models are extended to three dimensions, the two-dimensional qualitative similarity of the behavior for the cases of the quenched randomness and thermal noise versions of the XY model no longer applies: As mentioned above, the three-dimensional Kuramoto model with quenched disorder shows a discontinuous (‘first order’) phase transition

at a zero coupling strength. Independent of the magnitude of the spread in the rotations comprising the quenched disorder, the three-dimensional Kuramoto model always shows partial alignment for $K > 0$. Since in the three-dimensional model the coupling between any two agents is identical to the two-dimensional case, i.e., proportional to the sine of the angle between the unit vectors $\boldsymbol{\sigma}_i$ of the two agents, this model also describes the interactions of classical three-dimensional spins with global coupling, i.e., the mean-field classical Heisenberg model. If this quenched disorder in terms of the spread of natural rotations were to correspond with the a temporally noisy disordered system, then allowing for larger spread would correspond to higher temperatures and larger noise. However, at finite positive temperature the classical Heisenberg model, like the XY model, has a continuous phase transition at a positive critical coupling strength K_c [75]. Thus, in contrast to the two-dimensional case, for these problems in three dimensions there is a qualitative difference between temperature and quenched disorder.

3.2 Model Description

In order to see how the Kuramoto model can be generalized to higher dimensions [71, 72], we note that Eq. (4.1) for θ_i can be rewritten (see Fig. 3.2 and its caption) in terms of the evolution of a collection of N two-dimensional unit vectors, $\boldsymbol{\sigma}_i$ with (x, y) components $(\cos \theta_i, \sin \theta_i)$:

$$\frac{d\boldsymbol{\sigma}_i}{dt} = \frac{K}{N} \sum_{j=1}^N [\boldsymbol{\sigma}_j - (\boldsymbol{\sigma}_j \cdot \boldsymbol{\sigma}_i) \boldsymbol{\sigma}_i] + \mathbf{W}_i \boldsymbol{\sigma}_i, \quad (3.2)$$

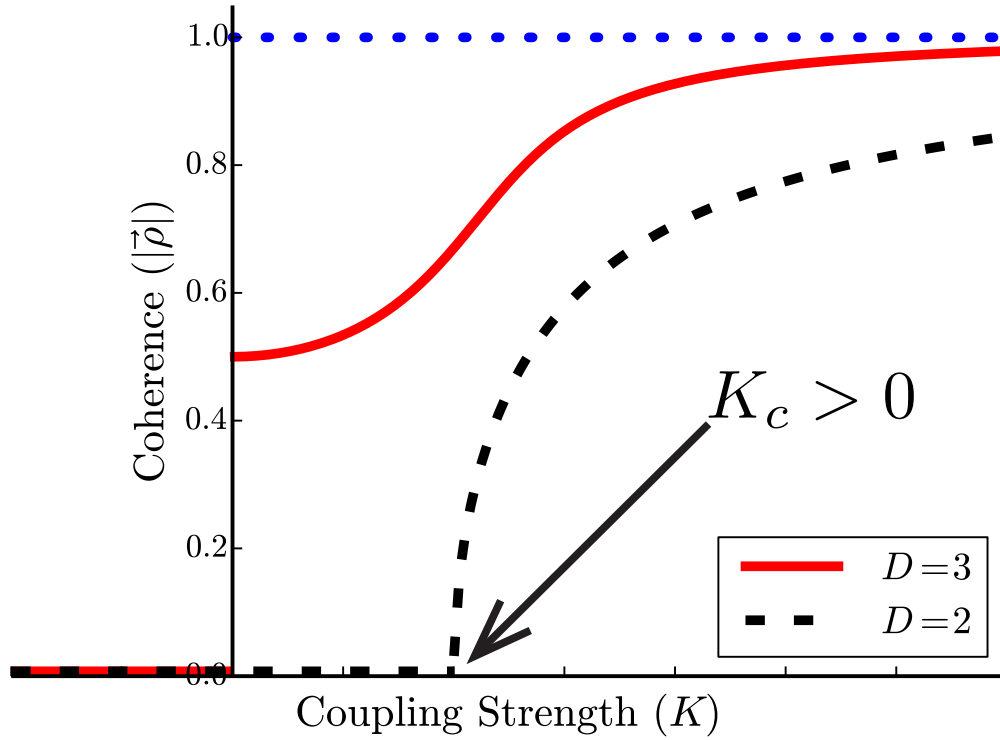


Figure 3.1: Phase transitions for the standard two-dimensional Kuramoto model from theory, shown as the black dashed curve, and for the Kuramoto model generalized to three dimensions as calculated from the theory in Eq. (3.18), shown as the solid red curve. Note the continuous transition in the two-dimensional Kuramoto model at a critical coupling of $K_c > 0$, and the discontinuous transition of the three-dimensional Kuramoto model at $K_c = 0$. The blue dotted line represents the maximum possible value of coherence, corresponding to $|\boldsymbol{\rho}| = 1$.

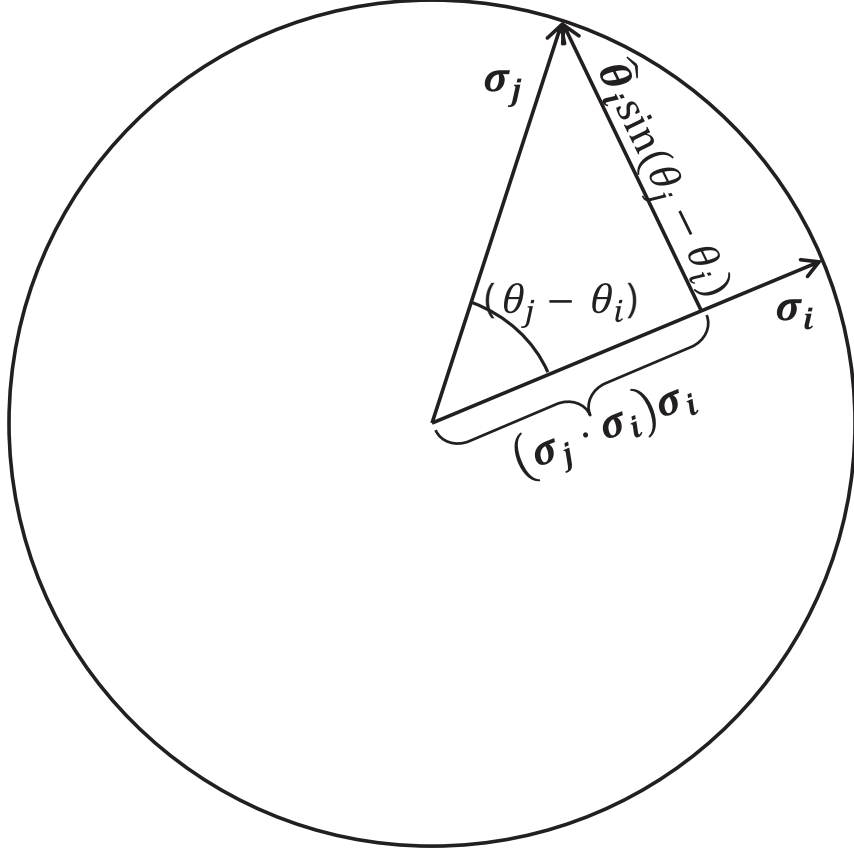


Figure 3.2: Illustration showing that $[\sigma_j - (\sigma_j \cdot \sigma_i)\sigma_i] = \hat{\theta}_i \sin(\theta_j - \theta_i)$, where $\hat{\theta}_i$ is a unit vector in the direction of increasing θ_i .

where

$$\mathbf{W}_i = \begin{pmatrix} 0 & \omega_i \\ -\omega_i & 0 \end{pmatrix}. \quad (3.3)$$

From this point of view the natural generalization of the Kuramoto problem, Eq. (4.1), to D dimensions is to consider Eq. (3.2), but now with σ_i being a unit vector in D dimensions and \mathbf{W}_i being a real $D \times D$ antisymmetric matrix. Thus, unlike the standard Kuramoto model where the state of an agent is described by a single scalar variable θ_i , the state of each agent in this generalized Kuramoto model is completely described by a D -dimensional unit vector σ_i .

Each \mathbf{W}_i term can be thought of as a constant bias to the dynamics of σ_i . In

the uncoupled dynamics, $d\boldsymbol{\sigma}_i/dt = \mathbf{W}_i\boldsymbol{\sigma}_i$, each agent is acted on by a constant linear operator, which causes each agent to move along the surface of the unit sphere \mathcal{S} . For example, in the context of swarms or flocks, it is natural to assume that each agent, in the absence of coupling ($K = 0$), has some imperfection that causes it to deviate away from the ideal of straight-line steady motion ($d\boldsymbol{\sigma}_i/dt = 0$). Antisymmetry of \mathbf{W}_i is imposed so as to ensure that the state vectors $\boldsymbol{\sigma}_i$ are unit vectors at all times.

For example, $D = 3$, as discussed above, is of particular interest. In this case the term $\mathbf{W}_i\boldsymbol{\sigma}_i$ can be represented as

$$\mathbf{W}_i\boldsymbol{\sigma}_i = \boldsymbol{\omega}_i \times \boldsymbol{\sigma}_i, \quad \boldsymbol{\omega}_i = \omega_i \hat{\boldsymbol{\omega}}_i, \quad \omega_i = |\boldsymbol{\omega}_i|, \quad \hat{\boldsymbol{\omega}}_i = \boldsymbol{\omega}_i/|\boldsymbol{\omega}_i|, \quad (3.4)$$

where $\boldsymbol{\omega}_i$ is referred to as the rotation vector; see Fig. 3.3 which schematically represents the solution of Eq. (3.2) for the case $K = 0$ and $D = 3$, in which $\boldsymbol{\sigma}_i$ is shown precessing around the vector $\hat{\boldsymbol{\omega}}_i = \boldsymbol{\omega}_i/|\boldsymbol{\omega}_i|$ at the rate $\omega_i = |\boldsymbol{\omega}_i|$. (Here, and later in this chapter, we use the notation $|\mathbf{v}|$ to represent the Euclidean norm of the vector \mathbf{v}) Note that the dot product of the right-hand side of Eq. (3.2) with $\boldsymbol{\sigma}_i$ is identically zero in all dimensions D , implying that $d|\boldsymbol{\sigma}_i|/dt = 0$, consistent with $\boldsymbol{\sigma}_i$ being a unit vector.

In the context of the spin models discussed earlier in Sec. 3.1.3, for positive K , the first term in Eq. (3.2) corresponds to the interaction term between individual spins, with each pair of spins tending to align themselves parallel to each other. This term leads to macroscopic magnetization in the system of spins. The second term in Eq. (3.2), $\mathbf{W}_i\boldsymbol{\sigma}_i$, corresponds to the quenched disorder discussed in Sec.

3.1.3 which inhibits coherence among the spins.

In the context of flocking models, each $\boldsymbol{\sigma}_i$ is interpreted as the unit vector along the velocity vector for the i^{th} agent. It is also assumed that the state of the agent is completely described by $\boldsymbol{\sigma}_i$, i.e., the agent is effectively axisymmetric about $\boldsymbol{\sigma}_i$. For positive K , the summation term in Eq. (3.2) corresponds to all-to-all communication between agents in the flock, with each agent tending to align itself with each of the other agents. This term promotes coherence within the flock. The second term, $\mathbf{W}_i \boldsymbol{\sigma}_i$, corresponds to a simple dispersing term causing decorrelation of the agent orientations $\boldsymbol{\sigma}_i$. In particular, if we wish to consider the addition of a dispersal term that maintains the norm of $\boldsymbol{\sigma}_i$, and for simplicity is assumed to be time independent and linear, then it must be of the form $\mathbf{W}_i \boldsymbol{\sigma}_i$ for some antisymmetric matrix \mathbf{W}_i .

In the context of swarms and flocks of three-dimensional agents, further motivation and justification for the form of the dispersing term $\mathbf{W}_i \boldsymbol{\sigma}_i$ is presented in Sec. 3.4. In particular, in order to support the possible generality of our main result (exemplified in Fig. 3.1), in Sec. 3.4 we consider another model, different from the generalized Kuramoto model Eq. (3.2), and show that our result also applies to this other model.

To better understand the dynamics of the generalized, D -dimensional Kuramoto model, we define an ‘order parameter’, $\boldsymbol{\rho}$, that is analogous to the Kuramoto order parameter, $N^{-1} \sum_j \exp(i\theta_j)$, used to analyze the system of Eq. (3.2) and is

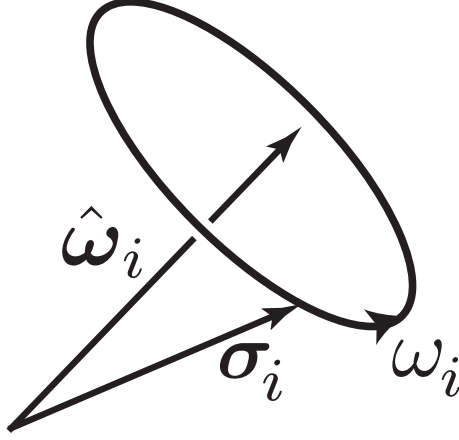


Figure 3.3: σ_i precesses around $\hat{\omega}_i$ with an angular frequency of ω_i for $K = 0$ with $D = 3$.

equivalent to it for $D = 2$:

$$\rho = \frac{1}{N} \sum_{i=1}^N \sigma_i. \quad (3.5)$$

Like the Kuramoto order parameter, $|\rho| = 1$ corresponds to the system being a completely coherent state, $\sigma_i = \sigma_j$ for all i, j ; while $|\rho| = 0$ corresponds to an incoherent state. Using this order parameter, we can rewrite Eq. (3.2) as

$$\frac{d\sigma_i}{dt} = K[\rho - (\rho \cdot \sigma_i)\sigma_i] + \mathbf{W}_i \sigma_i. \quad (3.6)$$

It can be seen in the above equation that the dynamics of each agent is determined by the two terms on the right-hand side. The first term (i.e., the term proportional to K) represents a global coupling of each agent to all the other agents through the order parameter. For positive K , this term attracts the state of each agent, σ_i , towards the average orientation of the full population, characterized by the direction of ρ ; whereas for negative K , this term causes dispersal of the system agents away from coherence, with each agent moving away from the average orientation of the

agents. The second term also gives dispersing dynamics, with each individual agent having distinct individual dynamics when uncoupled from the other agents in the system.

To completely specify the setup of the system, we need to specify the choice of the N natural rotations in Eq. (3.6). In the case of the standard $D = 2$ Kuramoto model, Eq. (4.1), the natural rotations are added in the form of individual distinct natural frequencies ω_i for each individual agent. Assuming that the natural frequency of each agent is independently picked randomly according to a fixed unimodal distribution $g(\omega)$, the change in coordinates, $\theta_i \rightarrow \theta_i + \omega_0 t$, effectively reduces the natural frequency of each agent by any constant ω_0 . Thus the mean of the distribution $g(\omega)$ can be set to 0 without loss of generality. In the unit vector formulation of the $D = 2$ Kuramoto model, this is equivalent to the change of variables $\boldsymbol{\sigma}_i \rightarrow e^{\mathbf{W}_0 t} \boldsymbol{\sigma}_i$, where

$$\mathbf{W}_0 = \begin{pmatrix} 0 & \omega_0 \\ -\omega_0 & 0 \end{pmatrix}.$$

The new equation after the change of variables has the rotation matrix shifted as $\mathbf{W}_i \rightarrow e^{\mathbf{W}_0 t} \mathbf{W}_i e^{-\mathbf{W}_0 t} - \mathbf{W}_0$. In the case of $D = 2$, the matrices $e^{\mathbf{W}_0 t}$ and \mathbf{W}_i commute, and hence the change is equivalent to the time-independent transformation $\mathbf{W}_i \rightarrow \mathbf{W}_i - \mathbf{W}_0$, allowing us to shift the mean of the distribution to any arbitrary quantity. For $D > 2$, however, commutation of antisymmetric matrices or rotation matrices does not generally apply (i.e., the rotation group in $D > 2$ is nonabelian),

and hence this change of coordinates does not yield an equivalent model with a change of rotation matrices. Thus for $D > 2$ the mean of this distribution cannot be simply shifted as in $D = 2$.

In general, for D dimensions, we specify the distribution over the space of antisymmetric matrices that we use to choose the individual \mathbf{W}_i for each agent i . We denote this distribution by $G(\mathbf{W})$, which is analogous to the distribution $g(\omega)$ in the case of $D = 2$. In this chapter, we restrict the choice of $G(\mathbf{W})$ as follows: we choose each of the upper-triangular elements of \mathbf{W} independently from a normal distribution with zero mean and a standard deviation of Δ . The lower-triangular elements are then set according to the constraint that \mathbf{W} is an antisymmetric matrix. This particular choice of $G(\mathbf{W})$ corresponds to an ensemble of antisymmetric matrices that has zero mean, and is invariant to rotations (choosing an anisotropic distribution, such as shifting the mean of the upper-triangular elements, or choosing the upper-triangular elements from normal distributions with unequal variance does not appear to change the qualitative results illustrated in Fig. 3.1). Hence, due to the rotational symmetry, $|\boldsymbol{\rho}| = 0$ will be a solution to our system (note that this solution may be stable or unstable). Further, we also note that Eq. (3.2) is invariant to the transformation $t \rightarrow \Delta \times t$, $K \rightarrow K/\Delta$ and $\mathbf{W} \rightarrow \mathbf{W}/\Delta$, and hence, without loss of generality, we set Δ to be unity for the remainder of this chapter.

For future reference, it is useful to point out the following facts that apply to any real antisymmetric matrix \mathbf{A} (such as \mathbf{W}_i):

- (i) Since $i\mathbf{A}$ is Hermitian, the real part of all the eigenvalues of \mathbf{A} is zero. Hence

all nonzero eigenvalues will be purely imaginary or zero.

- (ii) If λ is an eigenvalue of \mathbf{A} , then so is $-\lambda$.
- (iii) If D is odd, then \mathbf{A} must have at least one zero eigenvalue [implied by (ii)].

Further, the corresponding eigenvector is real.

For example, following Eq. (3.2) we have noted that for $D = 3$ we can express $\mathbf{W}_j \boldsymbol{\sigma}_j$ in the form $\boldsymbol{\omega}_j \times \boldsymbol{\sigma}_j$, with $\boldsymbol{\omega}_j = \omega_j \hat{\boldsymbol{\omega}}_j$. In terms of the above discussion, $\hat{\boldsymbol{\omega}}_j$ is the real eigenvector corresponding to the zero eigenvalue of the 3×3 matrix \mathbf{W}_j ($\mathbf{W}_j \hat{\boldsymbol{\omega}}_j = 0$), and $\pm i\omega_j$ are the nonzero eigenvalues of \mathbf{W}_j .

As discussed earlier, for $D = 3$ we can now represent the second term on the right-hand side of Eq. (3.6) as a cross product, giving

$$\frac{d\boldsymbol{\sigma}_i}{dt} = K[\boldsymbol{\rho} - (\boldsymbol{\rho} \cdot \boldsymbol{\sigma}_i)\boldsymbol{\sigma}_i] + \boldsymbol{\omega}_i \times \boldsymbol{\sigma}_i. \quad (3.7)$$

Given the choice of the distribution $G(\mathbf{W})$ made above, we can write the distribution of the natural rotations of individual agents as $G(\boldsymbol{\omega}) = g(\omega)U(\hat{\boldsymbol{\omega}})$, where $\boldsymbol{\omega} = \omega \hat{\boldsymbol{\omega}}$, with $\omega = |\boldsymbol{\omega}|$ and $\hat{\boldsymbol{\omega}} = \boldsymbol{\omega}/\omega$. The distribution of rotation directions, $U(\hat{\boldsymbol{\omega}})$ is then isotropic, and independent of the distribution of rotation magnitudes, and the distribution of magnitudes is $g(\omega) = \sqrt{2}\omega^2 \exp[-\omega^2/(2\Delta^2)]/(\pi^{3/2}\Delta^3)$. This choice of the distribution $G(\boldsymbol{\omega})$ sets the mean of the distribution to always be 0. In numerically simulating this system, we observe that the order parameter always goes to a fixed point, similar to the case of the standard Kuramoto model with zero mean of the distribution of frequencies.

3.3 Dynamics and Equilibria

To map out the interplay between the tendency to align and the natural rotation of the individual units [i.e. the two opposing tendencies represented by the two terms on the right-hand side of Eq. (3.2)], we plot numerically obtained phase transition diagrams for $D = 2 - 9$ (see Fig. 3.4). For large N and varying values of the coupling strength K , we allow the system to reach its time asymptotic equilibrium, and then we plot the magnitude of the order parameter at equilibrium as a function of K . We note that the results in Fig. 3.4 apply for all the random initial realizations of the distributions of the individual states σ_i that we have tested.

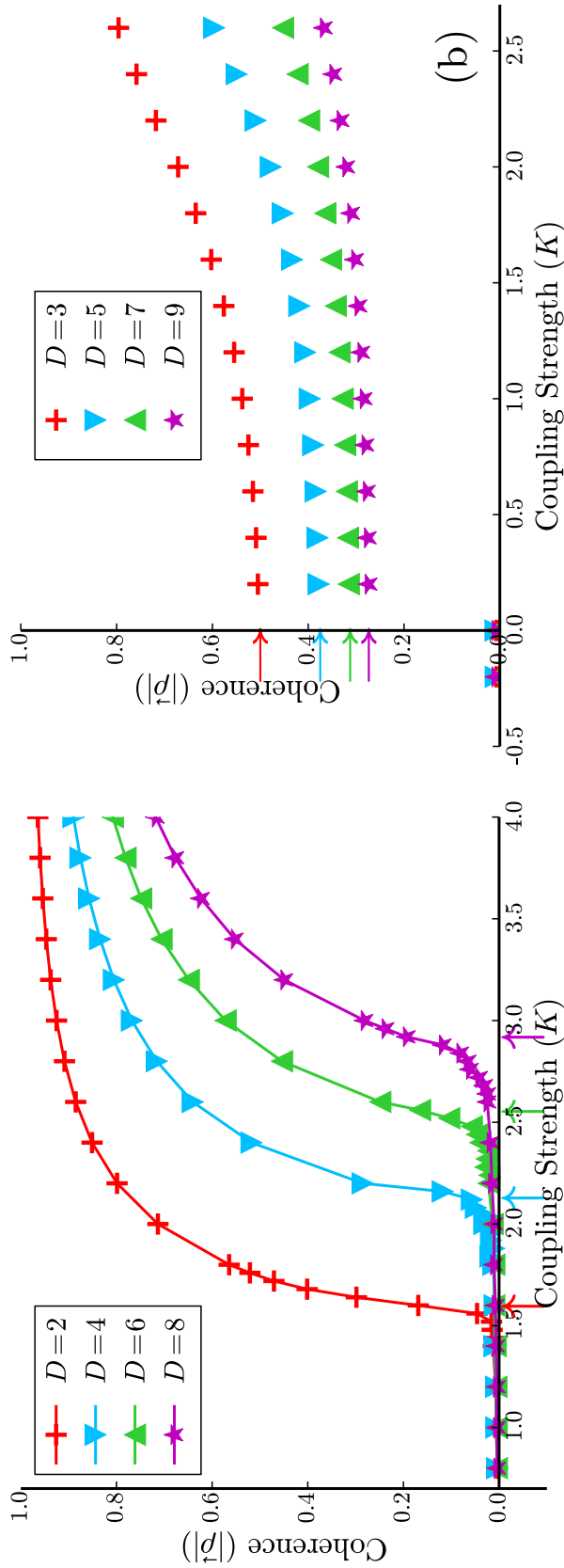


Figure 3.4: (a) Phase transitions for the generalized Kuramoto model for $D = 2$ (red plus signs), 4 (blue inverted triangles), 6 (green triangles) and 8 (magenta stars) dimensions, numerical observations for $N = 10^5$. (b) Phase transitions for the Kuramoto model generalized to $D = 3$ (red plus signs), 5 (blue inverted triangles), 7 (green triangles) and 9 (magenta stars) dimensions, numerical observations for $N = 10^4$. $\Delta = 1$ in each. The theoretical predictions from Eqs. (3.42) and (3.44) for the critical coupling strength for even dimensions has been shown in correspondingly colored arrows on the x -axis in (a). For a discussion on the slight mismatch between the theory and the numerical results, see Sec. 3.3.3. We expect this mismatch to decrease with increasing N . The theoretical estimates from Eq. (3.13) for the magnitude of the discontinuity, i.e., $|\rho|$ at $K \rightarrow 0^+$ are shown in correspondingly colored arrows on the y -axis in (b). Note the close match between the theoretical result for the discontinuity, and the numerical observation for $|\rho|$ at $K = 0.2$.

As would be expected from the earlier discussion, in the case of negative coupling, i.e., $K < 0$, the system of agents goes to a state which is incoherent, $|\boldsymbol{\rho}| \approx 0$. For even D , as in the $D = 2$ Kuramoto model (Fig. 3.4), there exists a positive critical coupling constant $K_c > 0$. In contrast, for odd D , coherence begins at $K = 0$, i.e., $K_c = 0$. Moreover, in contrast to the even D case where the transition is continuous (‘second order’), for odd D the transition is a discontinuous jump from $|\boldsymbol{\rho}| = 0$ in $K < 0$ to $|\boldsymbol{\rho}| > 0$ for $K \rightarrow 0^+$, past which $|\boldsymbol{\rho}|$ increases continuously with increasing K , asymptoting at $|\boldsymbol{\rho}| = 1$ as $K \rightarrow \infty$. For example, for $D = 3$ we find that $|\boldsymbol{\rho}| = 0.5$ at $K = 0^+$, and this result (as we shall subsequently show) is independent of the distribution $g(\omega)$. Furthermore, we find that this discontinuous transition is nonhysteretic. To better understand these observed phenomena, we now present a mathematical analysis of this system.

3.3.1 Coherent states for $D = 3$

We first focus on the case of a positive coupling constant K in three dimensions. We seek fixed points of the order parameter. To study these analytically we first solve for fixed points of the agents, assuming that the order parameter is at a fixed point with positive magnitude. We hence solve

$$0 = K[\boldsymbol{\rho} - (\boldsymbol{\rho} \cdot \boldsymbol{\sigma}_i^F)\boldsymbol{\sigma}_i^F] + \boldsymbol{\omega}_i \times \boldsymbol{\sigma}_i^F \quad (3.8)$$

for $\boldsymbol{\sigma}_i^F$. The superscript F indicates that the agent is at a fixed point. Given a spherically symmetric distribution of rotation vectors, we can choose the direction

of the order parameter $\boldsymbol{\rho}$ arbitrarily. The magnitude of the order parameter must be chosen to be self consistent given the orientation of the agents, according to Eq. (3.5). We define a quantity $\mu_i = \omega_i / (K|\boldsymbol{\rho}|)$ to rewrite the above equation as

$$0 = [\hat{\boldsymbol{\rho}} - (\hat{\boldsymbol{\rho}} \cdot \boldsymbol{\sigma}_i^F) \boldsymbol{\sigma}_i^F] + \mu_i (\hat{\boldsymbol{\omega}}_i \times \boldsymbol{\sigma}_i^F), \quad (3.9)$$

where $\hat{\boldsymbol{\rho}} = \boldsymbol{\rho} / |\boldsymbol{\rho}|$ is a unit vector in the direction of $\boldsymbol{\rho}$. This vector equation can be solved (see Appendix A.1) to obtain

$$\hat{\boldsymbol{\rho}} \cdot \boldsymbol{\sigma}_i^F = \pm \sqrt{\frac{(1 - \mu_i^2) + \sqrt{(\mu_i^2 - 1)^2 + 4\mu_i^2(\hat{\boldsymbol{\rho}} \cdot \hat{\boldsymbol{\omega}}_i)^2}}{2}}, \quad (3.10)$$

and in terms of $\hat{\boldsymbol{\rho}} \cdot \boldsymbol{\sigma}_i^F$

$$\boldsymbol{\sigma}_i^F = \frac{1}{1 + \xi_i^2 \mu_i^2} [\mu_i (\hat{\boldsymbol{\omega}}_i \times \hat{\boldsymbol{\rho}}) + \xi_i \mu_i^2 \hat{\boldsymbol{\omega}}_i + t_i \hat{\boldsymbol{\rho}}] \quad (3.11)$$

where $t_i = \hat{\boldsymbol{\rho}} \cdot \boldsymbol{\sigma}_i^F$, and $\xi_i = \hat{\boldsymbol{\rho}} \cdot \hat{\boldsymbol{\omega}}_i / \hat{\boldsymbol{\rho}} \cdot \boldsymbol{\sigma}_i^F$.

From Eq. (3.10) we observe that there are two fixed points for each agent, one in the same hemisphere as the order parameter vector (corresponding to $\hat{\boldsymbol{\rho}} \cdot \boldsymbol{\sigma}_i^F > 0$), and the other in the opposite hemisphere (corresponding to $\hat{\boldsymbol{\rho}} \cdot \boldsymbol{\sigma}_i^F < 0$). Importantly, we also observe that there is a fixed point solution $\boldsymbol{\sigma}_i^F$ for any given $\boldsymbol{\omega}_i$, $\boldsymbol{\rho}$ and K . Do these solutions correspond to a stable or unstable fixed points? Given a steady-state solution with all agents at one of their fixed points, for some $\boldsymbol{\rho}$ such that $|\boldsymbol{\rho}| > 0$, we consider a perturbation $\boldsymbol{\epsilon}_i$ to the i^{th} agent. Assuming that $\boldsymbol{\sigma}_i(t) = \boldsymbol{\sigma}_i^F + \boldsymbol{\epsilon}_i(t)$, we

linearize Eq. (3.7) for small ϵ_i to obtain

$$\frac{d|\epsilon_i(t)|}{dt} = -K(\boldsymbol{\rho} \cdot \boldsymbol{\sigma}_i^F)|\epsilon_i(t)|, \quad (3.12)$$

where we have used $\epsilon_i \cdot \boldsymbol{\sigma}_i^F = 0$ so that the perturbed $\boldsymbol{\sigma}_i$ remains a unit vector. Thus we see that the stability of the fixed point $\boldsymbol{\sigma}_i^F$ depends on the sign of $\boldsymbol{\rho} \cdot \boldsymbol{\sigma}_i^F$, with positive (negative) $\boldsymbol{\rho} \cdot \boldsymbol{\sigma}_i^F$ implying a stable (an unstable) fixed point. Since for each agent $\boldsymbol{\sigma}_i$ there are two solutions for $\boldsymbol{\sigma}_i^F$ with opposing signs of $\boldsymbol{\rho} \cdot \boldsymbol{\sigma}_i^F$ according to Eq. (3.10), each agent has a stable fixed point and an unstable fixed point. We assume that each agent will approach its stable fixed point.

This behavior is in contrast to the two-dimensional Kuramoto model, where the proportion of agents in the entrained population increases continuously from 0 as we increase K beyond K_c . (This fundamental difference is due to the previously noted fact that \mathbf{W}_i for odd D always has zero as one of its eigenvalues.) To understand the presence of the discontinuous phase transition, we first look at the case of small coupling, such that $0 < K \ll \Delta$. By ignoring the first term on the right-hand side of Eq. (3.8), or by considering the limit of $\mu_i \rightarrow \infty$ in Eqs. (3.10) and (3.11), we see that $\boldsymbol{\sigma}_i^F = \pm \hat{\boldsymbol{\omega}}_i$. Since the stable fixed points corresponds to $\boldsymbol{\rho} \cdot \boldsymbol{\sigma}_i^F > 0$, each agent will go to a stable fixed point given by $[\text{sgn}(\boldsymbol{\rho} \cdot \hat{\boldsymbol{\omega}}_i)]\hat{\boldsymbol{\omega}}_i$. Note that this location of the fixed point on the unit sphere is independent of the magnitude of the agent's rotation vector, and depends only on the orientation of the rotation vector. Since the distribution of rotation vectors was chosen such that the distribution of directions $U(\hat{\boldsymbol{\omega}})$ was uniform on the unit sphere, the fixed points $\text{sgn}(\boldsymbol{\rho} \cdot \hat{\boldsymbol{\omega}}_i)\hat{\boldsymbol{\omega}}_i$ will

be a set of uniformly distributed points over the hemisphere, $\boldsymbol{\rho} \cdot \boldsymbol{\sigma} > 0$, of unit radius. This is demonstrated in Fig. 3.5, where we illustrate the orientations of $N = 5 \cdot 10^3$ agents at a fixed time for a coupling strength $K = 0.1$. In this plot, we have mapped the endpoints of the orientation vectors $\boldsymbol{\sigma}_i$ on the unit sphere \mathcal{S} to a rectangle via an area-preserving transformation (see Fig. 3.5 caption for details). At the initial time, corresponding to an initial uniform distribution on \mathcal{S} , the agents are uniformly distributed on the rectangle, whereas after $T = 50000$ time units it can be seen that the agents are uniformly distributed over only the upper half of the rectangle, corresponding to the hemisphere $\boldsymbol{\rho} \cdot \boldsymbol{\sigma} > 0$ of \mathcal{S} .

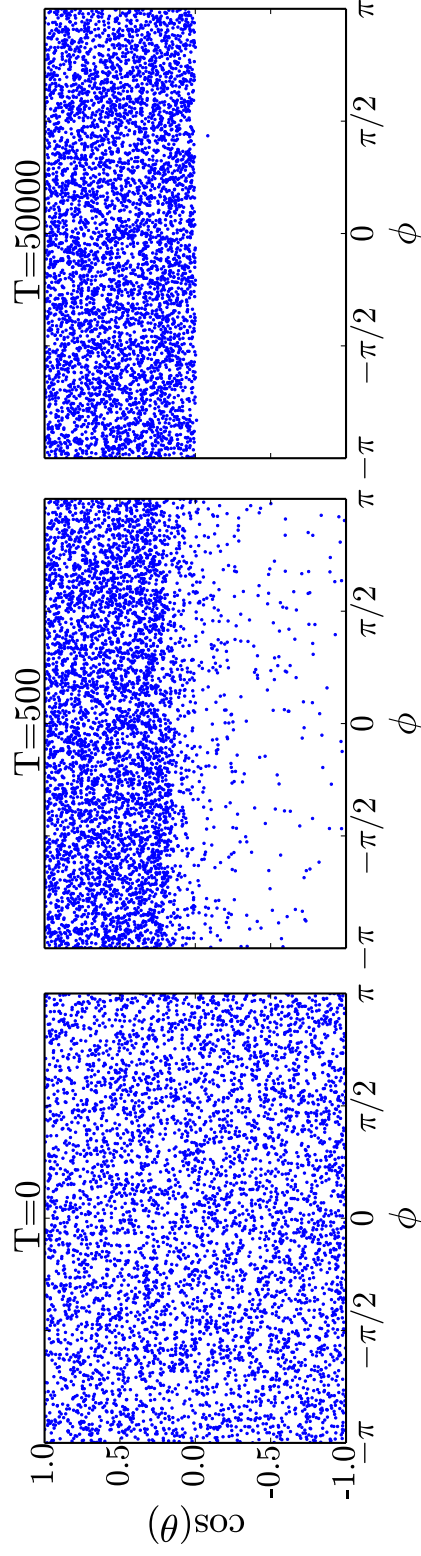


Figure 3.5: Orientations of each of the $N = 5 \cdot 10^3$ agents at time $T = 0$, $T = 500$ and $T = 50000$. We visualize the orientations by plotting the endpoints of the orientation vectors on the sphere \mathcal{S} . The sphere is then mapped onto a rectangle using an area-preserving transformation. We choose the z -axis along $\boldsymbol{\rho}$, and arbitrarily choose mutually orthogonal x and y axes. θ then represents the angle measured from the z -axis ($\cos\theta = \hat{\boldsymbol{\rho}} \cdot \boldsymbol{\sigma}$), and ϕ represents the azimuthal angle measured anti-clockwise from the x -axis. The agent state vectors are initialized with a uniform distribution on the sphere, and evolved with a coupling constant $K = 0.1$. Note how all of the agents tend to uniformly distribute themselves on one hemisphere.

As discussed earlier, the magnitude of the order parameter must be consistent with the orientations of the agents, according to Eq. (3.5). Thus, being the average of the orientations of all the agents, the order parameter will have $|\boldsymbol{\rho}| = 1/2$, since the centroid of a hemisphere is located at a distance of half of the radius from the center of the sphere.

This result is independent of the choice of the distribution $g(\omega)$, provided the rotation vector directions are isotropically distributed. As discussed earlier, negative values of coupling result in the system going to an incoherent state, with $|\boldsymbol{\rho}| = 0$, while here we see that for small positive coupling the order parameter attains a value of $|\boldsymbol{\rho}| = 0.5$. This result naturally generalizes to higher odd dimensions. As for the case of $D = 3$, let $\hat{\boldsymbol{\omega}}_i$ be the real eigenvector corresponding to the zero eigenvalue of the $D \times D$ matrix \mathbf{W}_i . In the limit of $0 < K \ll \Delta$, we can again ignore the first term on the right-hand of Eq. (3.2). Solving for fixed points, we set $d\boldsymbol{\sigma}_i/dt = 0$, and hence the fixed point solutions will be given by $\mathbf{W}_i \boldsymbol{\sigma}_i^F = 0$, or $\boldsymbol{\sigma}_i^F = \pm \hat{\boldsymbol{\omega}}_i$. Following the same analysis as performed above for $D = 3$, we reach the conclusion that for small positive K , the agents will go to fixed points given by $\text{sgn}(\boldsymbol{\rho} \cdot \hat{\boldsymbol{\omega}}_i) \hat{\boldsymbol{\omega}}_i$. Hence the magnitude of $\boldsymbol{\rho}$ at $K = 0^+$ will be given by the position of the centroid of a uniform hemisphere in D dimensions:

$$|\boldsymbol{\rho}(K \rightarrow 0^+)| = \frac{2\Gamma(D/2)}{(D-1)\sqrt{\pi}\Gamma[(D-1)/2]}. \quad (3.13)$$

This matches well with numerical results shown in Fig. 3.4 (b), where the colored arrows indicate the theory predictions according to Eq. (3.13). Note the close

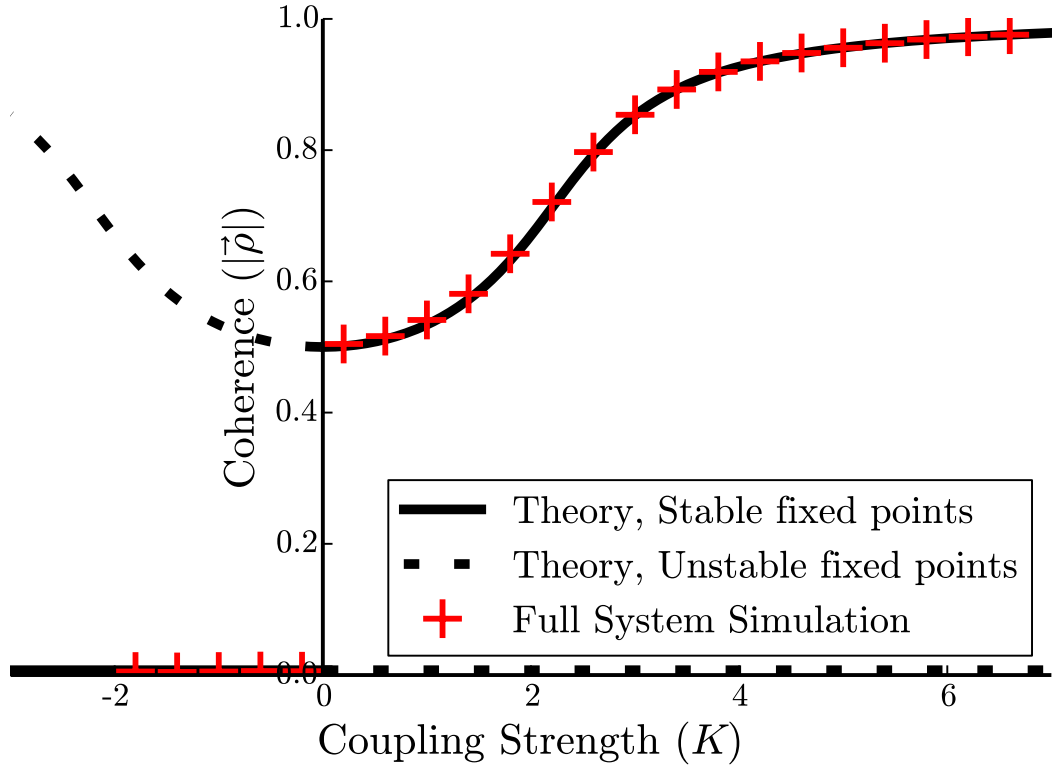


Figure 3.6: Phase transition for Kuramoto model generalized to three dimensions. The solid (dashed) black curve represents the derived stable (unstable) fixed points for the order parameter, and the red plus sign markers represent numerical results from a simulation with $N = 10^4$ agents and $\Delta = 1$.

agreement with the prediction of the magnitude of ρ indicated by these arrows at $K = 0$, and the $K > 0$ start of the phase transition curves at $K = 0.2$ shown by the various colored symbols.

By setting up a consistency relation in a similar fashion (see below), we can calculate the magnitude of the order parameter as a function of the coupling constant for $D = 3$. As shown in Fig. 3.6, this theory (solid black curve) agrees well with results from simulations of Eq. (3.2) with $N = 10^4$ (red plus signs).

We now give our analysis for $D = 3$ resulting in the solid curve in Fig. 3.6. As earlier, we assume that ρ is in some particular fixed direction. Since the distribution

of the direction of the unit vectors σ_i has been taken to be isotropic, we can assume that there will be rotational symmetry of the distribution of stable fixed points of the agents about the axis along ρ . Thus

$$|\rho| = \frac{1}{N} \sum_{i=1}^N \hat{\rho} \cdot \sigma_i^F. \quad (3.14)$$

Since each agent has a unique natural rotation vector, we label the agent state variables as functions of their rotation vectors, as opposed to the index label i . Since the rotation vectors are chosen from a given distribution $G(\omega)$, we can approximate the above sum as

$$|\rho| = \int \hat{\rho} \cdot \sigma^F(\omega) G(\omega) d\omega, \quad (3.15)$$

which applies in the limit $N \rightarrow \infty$ in Eq. (3.2). We interpret $\hat{\rho} \cdot \sigma^F(\omega)$ as $\cos[\theta(\omega)]$, where $\theta(\omega)$ is the angle between the direction of the order parameter, and the stable fixed point of the agent with rotation vector ω . We will later use Eq. (3.10) to insert the expression for $\cos[\theta(\omega)]$. We write the above as

$$|\rho| = \int \cos[\theta(\omega_0, \hat{\omega})] g(\omega_0) U(\hat{\omega}) d\omega_0 d\hat{\omega}. \quad (3.16)$$

Performing a change of variables from ω_0 to $\mu = \omega/(K|\rho|)$ we get

$$|\rho| = \int \cos[\theta(\mu, \hat{\omega})] g(\mu K|\rho|) U(\hat{\omega}) K|\rho| d\mu d\hat{\omega}, \quad (3.17)$$

and hence

$$1 = \int \cos[\theta(\mu, \hat{\omega})] g(\mu K |\rho|) U(\hat{\omega}) K d\mu d\hat{\omega}. \quad (3.18)$$

This can now be numerically solved to obtain $|\rho|$ for a given K . For example, for the particular choice of $G(\omega)$ discussed above, where the three components of each vector ω_i are chosen independently from a normal distribution centered at 0 with a standard deviation of Δ , the integral in Eq. (3.18) over $\hat{\omega}$ can be split into an azimuthal integral about the axis $\hat{\rho}$, which is trivial, and an integral over the angle between $\hat{\rho}$ and $\hat{\omega}$, i.e., the ζ integral below

$$1 = \frac{K}{2} \int_{-1}^1 d\zeta \int_{-\infty}^{\infty} d\mu \sqrt{\frac{[1 - \mu^2 + \sqrt{(\mu^2 - 1)^2 + 4\mu^2\zeta^2}]}{2}} \times \frac{e^{-(\mu K |\rho|)^2 / (2\Delta^2)}}{(\sqrt{2\pi}\Delta)^3} (\mu K |\rho|)^3, \quad (3.19)$$

where the integration variable ζ represents $\hat{\rho} \cdot \hat{\omega}$. Solving this integral equation numerically for $|\rho|$ for different values of the coupling constant K we obtain the solid black curve in Fig. 3.6.

To complete the analysis of the coherent states for $K > 0$, we now discuss why the state vectors σ_i approach their stable fixed points σ_i^F . We demonstrate this in the limit of $0 < K \ll \Delta$. Under this assumption, we note that in Eq. (3.7), the typical magnitude of the second term on the right-hand side, $\mathcal{O}(\Delta)$, is much larger than the first term, which is $\mathcal{O}(|K\rho|)$. We refer to $\mathcal{O}(\Delta)$ as the fast time-scale, and $\mathcal{O}(|K\rho|)$ as the slow time-scale. The assumed separation of time-scales implies that, to lowest order, we can neglect the first term in Eq. (3.7), leading to the equation

$$\frac{d\sigma_i}{dt} = \omega_i \hat{\omega}_i \times \sigma_i. \quad (3.20)$$

This has the solution depicted in Fig. 3.3, where the state vector $\boldsymbol{\sigma}_i$ uniformly precesses rapidly about $\hat{\boldsymbol{\omega}}_i$, with the quantity $z_i(t) = \boldsymbol{\sigma}_i(t) \cdot \hat{\boldsymbol{\omega}}_i$ constant on the fast time-scale. To determine the dynamics over the slow time-scale, we consider the dot product of Eq. (3.7) with $\hat{\boldsymbol{\omega}}_i$, and average both sides of the equation over the fast time scale. This gives the evolution of z_i as

$$\frac{dz_i(t)}{dt} = K \langle \boldsymbol{\rho} \rangle \cdot \hat{\boldsymbol{\omega}}_i [1 - z_i(t)^2], \quad (3.21)$$

where $\langle \boldsymbol{\rho} \rangle = N^{-1} \sum z_i \hat{\boldsymbol{\omega}}_i$, with the angle brackets representing averaging over the fast time-scale. This equation has a single stable fixed point at $+1$ or -1 dependent on the sign of $\langle \boldsymbol{\rho} \rangle \cdot \hat{\boldsymbol{\omega}}$. Thus starting from random initial conditions, $z_i(t)$ will move to its fixed point at $\text{sgn}(\langle \boldsymbol{\rho} \rangle \cdot \hat{\boldsymbol{\omega}})$. This is equivalent to stating that each $\boldsymbol{\sigma}_i$ will move to its fixed point $[\text{sgn}(\boldsymbol{\rho} \cdot \hat{\boldsymbol{\omega}}_i)] \hat{\boldsymbol{\omega}}_i$. While we have only thus proved that $\boldsymbol{\sigma}_i$ will approach $\boldsymbol{\sigma}_i^F$ in the limit of small K , we numerically observe this to be true for all K , i.e., each agent goes to its corresponding stable fixed point as discussed above.

Until now, we have restricted our discussion of coherent states to $K > 0$. Are there any stable coherent states for $K < 0$? If the answer were yes, the fixed points of the agents could be calculated as earlier resulting in Eqs. (3.10) and (3.11), and would be governed by the stability equation given in Eq. (3.12). Since $K < 0$, the stable fixed points will correspond to solutions where $\boldsymbol{\rho} \cdot \boldsymbol{\sigma}^F < 0$ for each of the agents. This would imply that all of the agents would point to the hemisphere that the vector $\boldsymbol{\rho}$ points away from (not toward), contradicting the definition of $\boldsymbol{\rho}$ as the average of the orientations of all the agents. Thus there cannot be any stable

fixed point solutions with positive magnitude of the order parameter for negative coupling.

This, however, does not rule out the possibility of unstable coherent states with $K < 0$. Going back to Eq. (3.7), we make a few observations. First, since all natural rotations were chosen such that the distribution of rotation directions was uniform on the sphere, the transformation $\boldsymbol{\omega} \rightarrow -\boldsymbol{\omega}$ does not affect the distribution or the macroscopic dynamics of the agents. After this transformation, we note that transforming $K \rightarrow -K$, and changing the direction of time, i.e., $t \rightarrow -t$, leaves Eq. (3.7) invariant. Thus, each stable fixed point of the macroscopic order parameter, $\boldsymbol{\rho}$, for a given value of coupling strength $K > 0$, is also a fixed point at a coupling strength of $-K$, but is unstable (since we have reversed the sign of time). Thus the curve of coherent stable states for $K > 0$ extends symmetrically to $K < 0$ representing coherent unstable states. These stable (solid black curve) and unstable states (dashed black curve) are shown in Fig. 3.6. We call these coherent states the ‘upper’ branch of the phase transition diagram.

3.3.2 Incoherent states for $D = 3$

When the order parameter has zero magnitude, the system is said to be incoherent. As we demonstrate, this state is stable for negative values of the coupling constant and unstable for positive values of the coupling constant.

In order to address the incoherent state, we first consider the following question: Given a state where $|\boldsymbol{\rho}| = 0$ for all time, what are the possible dynamics of the

individual agents? Setting $\boldsymbol{\rho} = 0$ in Eq. (3.2), we get $d\boldsymbol{\sigma}_i/dt = \mathbf{W}_i\boldsymbol{\sigma}_i$. In the case $D = 3$, this means that the state $\boldsymbol{\sigma}_i$ of each agent precesses about their own rotation axes, as illustrated in Fig. 3.3. If each agent were randomly placed uniformly on \mathcal{S} , then this would be consistent with $|\boldsymbol{\rho}| = 0$, and would be a steady state. However, this is not the only such arrangement of $\boldsymbol{\sigma}_i$ that is possible corresponding to $|\boldsymbol{\rho}| = 0$. For example, if each agent, $\boldsymbol{\sigma}_i$ was placed on the axis of the corresponding rotation vector, such that $\boldsymbol{\sigma}_i = \hat{\boldsymbol{\omega}}_i$ (or $\boldsymbol{\sigma}_i = -\hat{\boldsymbol{\omega}}_i$), then this would also be consistent with $|\boldsymbol{\rho}| = 0$ [since we have assumed that $U(\hat{\boldsymbol{\omega}})$ is uniform], and the agents would each be at fixed points (this will be possible whenever D is odd). In fact, the steady-state $|\boldsymbol{\rho}| = 0$ applies for any random proportion p of agents oriented parallel to the axes of their natural rotations, and the remaining agents at uniformly distributed locations on the sphere. Thus for $N \rightarrow \infty$ there are an infinite number of distributions of $\boldsymbol{\omega}$ and $\boldsymbol{\sigma}$ for which $|\boldsymbol{\rho}| = 0$ is a steady state.

To characterize these states in the limit of $N \rightarrow \infty$, we assume that the distribution of agent orientations $\boldsymbol{\sigma}$ rendered onto the unit sphere \mathcal{S} is well defined. We denote by $F(\boldsymbol{\sigma}, \boldsymbol{\omega}, t)$ the distribution of agents on \mathcal{S} , such that $F(\boldsymbol{\sigma}, \boldsymbol{\omega}, t)d\boldsymbol{\sigma}d\boldsymbol{\omega}$ is the fraction of agents that lie in the two-dimensional differential element on the surface \mathcal{S} centered at $\boldsymbol{\sigma}$ at time t , and have a natural rotation vector within the differential element $d\boldsymbol{\omega}$ centered at $\boldsymbol{\omega}$. Since the natural rotations of each agent are time independent and are independent of $\boldsymbol{\sigma}$, we can write

$$F(\boldsymbol{\sigma}, \boldsymbol{\omega}, t) = G(\boldsymbol{\omega})f(\boldsymbol{\sigma}, \boldsymbol{\omega}, t), \quad (3.22)$$

where

$$G(\boldsymbol{\omega}) = \int_{\mathcal{S}} F(\boldsymbol{\sigma}, \boldsymbol{\omega}, t) d\boldsymbol{\sigma}$$

is the distribution of the antisymmetric natural rotation vectors, $\int G(\boldsymbol{\omega}) d\boldsymbol{\omega} = 1$, and $G(\boldsymbol{\omega}) = g(\omega)U(\hat{\boldsymbol{\omega}})$. In terms of this distribution function F , the order parameter will be given as

$$\boldsymbol{\rho}(t) = \int_{\mathcal{S}} \boldsymbol{\sigma} G(\boldsymbol{\omega}) f(\boldsymbol{\sigma}, \boldsymbol{\omega}, t) d\boldsymbol{\sigma} d\boldsymbol{\omega}. \quad (3.23)$$

An example of a class of distributions in $D = 3$ for which $|\boldsymbol{\rho}| = 0$ is a steady state is given by

$$\begin{aligned} F_0(\boldsymbol{\sigma}, \boldsymbol{\omega}) &= g(\omega)U(\hat{\boldsymbol{\omega}}) \left[\frac{p}{2}\delta(\boldsymbol{\sigma} - \hat{\boldsymbol{\omega}}) + \frac{p}{2}\delta(\boldsymbol{\sigma} + \hat{\boldsymbol{\omega}}) + \frac{1-p}{4\pi} \right] \\ &= g(\omega)U(\hat{\boldsymbol{\omega}})f_0(\boldsymbol{\sigma}, \boldsymbol{\omega}), \end{aligned} \quad (3.24)$$

for any $p \in [0, 1]$, where $\delta(\cdot)$ represents the Dirac delta function.

As we will demonstrate shortly, in the limit $N \rightarrow \infty$, this entire class of distributions is stable to small perturbations for all $K < 0$, i.e., for the incoherent region demonstrated in Fig. 3.1. This is in sharp contrast to the case of $D = 2$, wherein there is a single stable incoherent steady-state distribution in the large system size limit (corresponding to $f = 1/(2\pi)$) for the incoherent region in Fig. 3.1.

However, we observe from numerical simulations with $K < 0$ (done at large, but necessarily finite N) that, starting with an initial condition corresponding to Eq. (3.24) with $p = 0$ (i.e., with $\boldsymbol{\sigma}_i$ distributed isotropically and *independently* of its corresponding $\boldsymbol{\omega}_i$, for all i) we observe that $\boldsymbol{\sigma}_i$ evolves slowly with time to

either $\sigma_i = +\hat{\omega}_i$ or $\sigma_i = -\hat{\omega}_i$ (i.e., σ_i aligns with its rotation vector), with about half of the population $\{\sigma_i\}$ going to $+\hat{\omega}_i$, and half to $-\hat{\omega}_i$. Furthermore, as N increases, the rate of this relaxation becomes slower and slower, approaching zero as $N \rightarrow \infty$. In addition, the fractions of agents going to $+\hat{\omega}_i$ and $-\hat{\omega}_i$ approach $1/2$ as $N \rightarrow \infty$. Thus, taking the limit $t \rightarrow \infty$ followed by taking the limit $N \rightarrow \infty$, Eq. (3.24) with $p = 1$ (i.e., $F(\sigma, \omega) = g(\omega)U(\hat{\omega})[\delta(\sigma - \hat{\omega}) + \delta(\sigma + \hat{\omega})]/2$) appears to approximate the distribution of agents on \mathcal{S} . If the order in which the limits are taken is reversed, then $p = 0$, its initial value (i.e., $F(\sigma, \omega) = g(\omega)U(\hat{\omega})U(\sigma)$) represents the distribution of agents on \mathcal{S} . Similar results apply for other odd values of the dimension D , where $\hat{\omega}_i$ is now the D -dimensional eigenvector of \mathbf{W}_i having zero eigenvalue and with magnitude one (i.e., $\mathbf{W}_i\hat{\omega}_i = 0$).

We illustrate these numerical results in Figs. 3.7 where we show the histograms of the initial (plotted in blue) and final (plotted in red) distributions of $\hat{\omega}_i \cdot \sigma_i$ over the N agents. These numerical simulations were performed with $N = 1000$, $K = -2$, $\Delta = 1$. In the insets we plot the time-series of z_i vs time for 50 randomly chosen agents. We see that for all odd D , $\hat{\omega}_i \cdot \sigma_i$ evolves towards ± 1 . Note that a similar consideration of even D is inapplicable since a randomly chosen even-dimensional \mathbf{W}_i typically does not have a zero eigenvalue, and thus $\hat{\omega}_i$ does not exist.

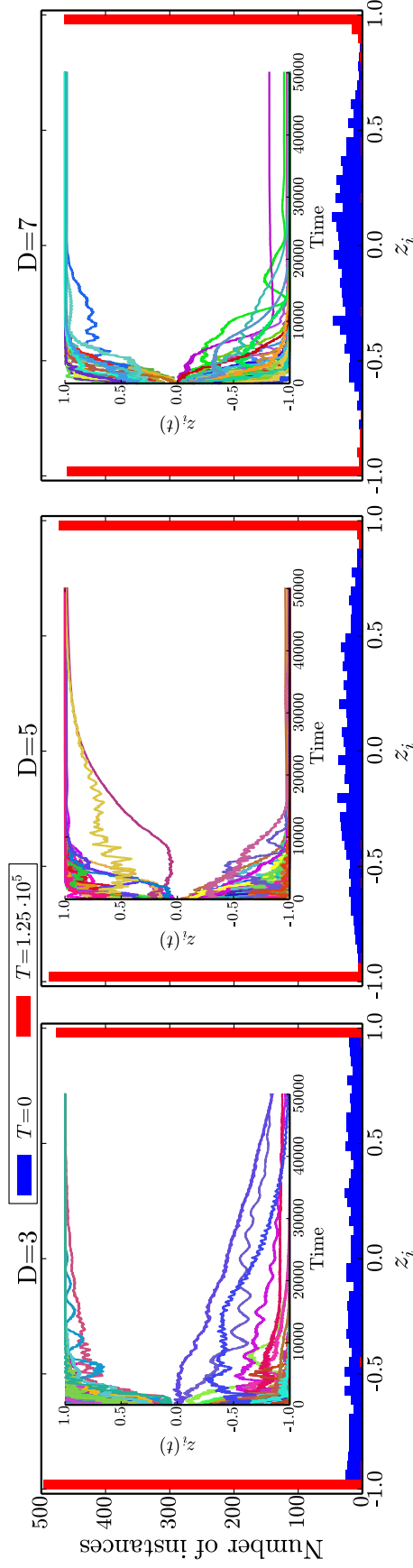


Figure 3.7: $N = 1000$ agents were simulated with a coupling strength of $K = -2$. Histograms of $z_i = \sigma_i \cdot \hat{\omega}_i$ have been plotted at $T = 0$ (in blue, corresponding to the initial condition having σ_i uniformly spread on \mathcal{S}), and after $T = 1.25 \cdot 10^5$ time units (in red). Note how the distributions concentrate at 1 and -1 for large T . In the insets, we show plots of z_i as a function of time for 50 randomly chosen agents.

While macroscopically, in terms of the magnitude of the order parameter ($|\boldsymbol{\rho}|=0$), the $N \rightarrow \infty$ stationary states with distributions given by Eq. (3.24) appear identical for all p , their stability to perturbations depends on p . To analyze the stability of this class of $N \rightarrow \infty$ stationary states we perform a linear analysis. To do this, we first describe the dynamics of the system in terms of the distribution F . We treat Eq. (3.7) as a velocity field for the flow of this distribution and hence set up a continuity equation:

$$\partial f / \partial t + \nabla_{\mathcal{S}} \cdot (f(\boldsymbol{\sigma}, \boldsymbol{\omega}, t) \mathbf{v}) = 0, \quad (3.25)$$

with a velocity field \mathbf{v} given by

$$\mathbf{v} = K[\boldsymbol{\rho} - (\boldsymbol{\sigma} \cdot \boldsymbol{\rho})\boldsymbol{\sigma}] + \boldsymbol{\omega} \times \boldsymbol{\sigma}, \quad (3.26)$$

where $\nabla_{\mathcal{S}} \cdot \mathbf{A}$ represents the operator for the divergence of an arbitrary vector field \mathbf{A} , along the surface \mathcal{S} of the unit sphere in $\boldsymbol{\sigma}$ -space. The order parameter, $\boldsymbol{\rho}$ is described in terms of the distribution function F according to Eq. (3.23). We show in Appendix A.2 that the continuity equation Eq. (3.25) can be rewritten as

$$\begin{aligned} \partial f / \partial t + [\nabla_{\mathcal{S}} f(\boldsymbol{\sigma}, \boldsymbol{\omega}, t) - 2f(\boldsymbol{\sigma}, \boldsymbol{\omega}, t)\boldsymbol{\sigma}] \cdot \boldsymbol{\rho} \\ + (\boldsymbol{\omega} \times \boldsymbol{\sigma}) \cdot \nabla_{\mathcal{S}} f(\boldsymbol{\sigma}, \boldsymbol{\omega}, t) = 0, \end{aligned} \quad (3.27)$$

where $\nabla_{\mathcal{S}} \Phi$ is the component of the gradient of a scalar field Φ that is parallel to the surface \mathcal{S} . We consider a small perturbation, such that the distribution $f(\boldsymbol{\sigma}, \boldsymbol{\omega}, t)$

can be written as

$$f(\boldsymbol{\sigma}, \boldsymbol{\omega}, t) = f_0(\boldsymbol{\sigma}, \boldsymbol{\omega}) + \xi(\boldsymbol{\sigma}, \boldsymbol{\omega})e^{st}, \quad (3.28)$$

where $\xi(\boldsymbol{\sigma}, \boldsymbol{\omega})$ is small. Inserting Eq. (4.25) into Eq. (3.27) and linearizing gives

$$s\xi(\boldsymbol{\sigma}, \boldsymbol{\omega}, t) + (\boldsymbol{\omega} \times \boldsymbol{\sigma}) \cdot \nabla \xi(\boldsymbol{\sigma}, \boldsymbol{\omega}, t) = 2K(\boldsymbol{\rho} \cdot \boldsymbol{\sigma})f_0(\boldsymbol{\sigma}, \boldsymbol{\omega}). \quad (3.29)$$

To further simplify this equation, we make a choice of basis, such that $\boldsymbol{\omega} = \omega \hat{z}$. This allows us to rewrite the above equation as

$$s\xi(\boldsymbol{\sigma}, \boldsymbol{\omega}, t) + \omega \frac{\partial}{\partial \phi} \xi(\boldsymbol{\sigma}, \boldsymbol{\omega}, t) = 2K(\boldsymbol{\rho} \cdot \boldsymbol{\sigma})f_0(\boldsymbol{\sigma}, \boldsymbol{\omega}), \quad (3.30)$$

where ϕ is the azimuthal coordinate around the z -axis. In this basis, we can then write f_0 as

$$f_0(\theta, \phi, \boldsymbol{\omega}) = \frac{p \delta(\theta) + \delta(\theta - \pi)}{2 \pi \sin(\theta)} + \frac{1-p}{4\pi}, \quad (3.31)$$

where θ is the angle measured from the z -axis, and together θ and ϕ represent $\boldsymbol{\sigma}$.

Inserting the form f_0 from Eq. (3.31) into Eq. (3.30), we then solve for $\xi(\boldsymbol{\sigma}, \boldsymbol{\omega}, t)$ and insert the obtained solution into Eq. (3.23) to obtain

$$\boldsymbol{\rho} = \boldsymbol{\rho}(1-p) \frac{2K}{3} \left(\frac{1}{3s} + \frac{2s}{3} \int \frac{g(\omega)d\omega}{s^2 + \omega^2} \right) + \boldsymbol{\rho} p \frac{2K}{3s},$$

giving the final dispersion relation,

$$1 = (1-p) \frac{2K}{3} \left[\frac{1}{3s} + \frac{2s}{3} \int \frac{g(\omega)d\omega}{s^2 + \omega^2} \right] + p \frac{2K}{3s}. \quad (3.32)$$

Note that the case of $p = 0$ (corresponding to an initial condition with independently chosen, uniformly random σ) and the case of $p = 1$ (corresponding to an initial condition with each σ being either $\hat{\omega}$ or $-\hat{\omega}$) have different dispersion relations. Thus, despite having the same macroscopic characteristic of $|\rho|=0$, they will have different stabilities to perturbation. In the limit of small K , s will also be small, and we can ignore the second term in the square brackets in the above expression. Thus,

$$s = (1 - p)\frac{2K}{9} + p\frac{2K}{3}.$$

Note that since K is small, this represents the behavior of s for K around zero. Since $s \propto K$, we see that the incoherent state, having $|\rho|=0$, will be stable ($s < 0$) for $K < 0$, and unstable ($s > 0$) for $K > 0$ as has been represented in Fig. 3.6. We call these incoherent states the ‘lower’ branch of the phase transition diagram.

It can be seen from Fig. 3.6 that the upper branch is stable whenever the lower branch is unstable (i.e., for $K > 0$), and the upper branch is unstable whenever the lower branch is stable (i.e., for $K < 0$). Thus, for no value of K are there two values of $|\rho|$ that are stable. This lack of bistability implies that the transition from incoherence to partial coherence occurs *nonhysteretically* at $K = 0$.

3.3.3 Phase transition in even dimensions

So far our primary focus has been on the cases of odd dimensions. As discussed earlier in Sec. 3.3 and in Fig. 3.4, the even-dimensional cases exhibit continuous (‘second order’) phase transitions at positive critical coupling strength $K_c > 0$. To

better understand this, we extend the treatment of the $D = 2$ case (e.g., Ref. [16]) to even $D > 2$. Like in the case of $D = 3$, we assume that the system has reached an equilibrium, with the order parameter having a magnitude $|\boldsymbol{\rho}|$. Unlike Eq. (3.11), wherein a fixed point for each agent exists for all values of \mathbf{W} , this will no longer be the case for even D . Rather, only certain values of the natural rotation \mathbf{W} will permit the existence of fixed points above a certain value of K . Similar to Ref. [16], we first determine the conditions on \mathbf{W} that permit fixed points of the corresponding agents, and then use this to set up a consistency relation similar to Eq. (3.14) to determine K_c . A key assumption in this approach is that for steady states with $|\boldsymbol{\rho}| > 0$ with $N \rightarrow \infty$, only agents for which $\boldsymbol{\sigma}$ is at a fixed point contribute to the sum in Eq. (3.5), which we prove *a posteriori* [see Eqs. (3.39) and (3.40) and accompanying discussion].

As in Eq. (3.8), we see that the fixed points of $\boldsymbol{\sigma}_i$ must satisfy

$$0 = K[\boldsymbol{\rho} - (\boldsymbol{\rho} \cdot \boldsymbol{\sigma}^F)\boldsymbol{\sigma}^F] + \mathbf{W}\boldsymbol{\sigma}^F, \quad (3.33)$$

where we have dropped the index i for simplicity. Denoting the term $(\boldsymbol{\rho} \cdot \boldsymbol{\sigma}^F)$ as γ , we observe

$$\boldsymbol{\sigma}^F = (\gamma\mathbb{1} - \mathbf{W})^{-1}\boldsymbol{\rho}, \quad (3.34)$$

where $\mathbf{1}$ denotes the D -dimensional identity matrix. Since $|\boldsymbol{\sigma}^F|^2 = (\boldsymbol{\sigma}^F)^T \boldsymbol{\sigma}^F = 1$,

$$1 = \boldsymbol{\rho}^T (\gamma \mathbf{1} + \mathbf{W}/K)^{-1} (\gamma \mathbf{1} - \mathbf{W}/K)^{-1} \boldsymbol{\rho} \quad (3.35)$$

$$= \boldsymbol{\rho}^T (\gamma^2 \mathbf{1} - \mathbf{W}^2/K^2)^{-1} \boldsymbol{\rho}. \quad (3.36)$$

We now transform the above equation to a basis that block-diagonalizes the anti-symmetric matrix \mathbf{W} . There exists a real orthogonal matrix, \mathbf{R} such that $\mathbf{R}^T \mathbf{W} \mathbf{R}$ is a block-diagonal matrix whose j^{th} block is the 2×2 matrix

$$\mathbf{W}^{(j)} = \begin{pmatrix} 0 & \omega_j \\ -\omega_j & 0 \end{pmatrix}$$

for all $j \in \{1, 2, \dots, D/2\}$. We will refer to these ω_j as the $\Lambda = D/2$ natural frequencies associated with \mathbf{W} . Further, we define ρ_k^2 to be the sum of the squares of the magnitudes of the $2k - 1^{\text{th}}$ and $2k^{\text{th}}$ components of $\mathbf{R}\boldsymbol{\rho}$. Then Eq. (3.36) can be simplified to

$$1 = \sum_{k=1}^{\Lambda} \frac{\rho_k^2}{\gamma^2 + \omega_k^2/K^2} \equiv H(\gamma). \quad (3.37)$$

Note that this change of basis does not affect the value of γ , since it is a scalar quantity. Each term in the summand of the above expression can be interpreted as being proportional to a Lorentzian function of γ centered about $\gamma = 0$, and hence has a single maximum at $\gamma = 0$. Thus, $H(\gamma)$ will also have a single maximum at $\gamma = 0$, from which it follows that in order for Eq. (3.37) to have a real solution for γ , $H(\gamma = 0)$ must be greater than or equal to 1. Hence the condition on \mathbf{W} that

will permit the existence of $\boldsymbol{\sigma}^F$ will be

$$H(\gamma = 0) = K^2 \sum_k \frac{\rho_k^2}{\omega_k^2} > 1. \quad (3.38)$$

For the case of the standard $D = 2$ Kuramoto model, the above criteria reduces to $|\omega| < |K\rho|$ (Ref. [16], Eq. (4.2)). For a given $\boldsymbol{\rho}$, we denote the region in \mathbf{W} -space that satisfies that the above criteria as Γ . Each $\mathbf{W}_i \in \Gamma$ will have a corresponding fixed point for $\boldsymbol{\sigma}_i$ and the set of such agents i will be referred to as the entrained population. For each $\mathbf{W}_j \notin \Gamma$, $\boldsymbol{\sigma}_j$ is continually in motion, and we refer to these agents as the drifting population. We now argue that the contribution to the order parameter, $\boldsymbol{\rho}$ from the drifting population will be zero, and then use the Eq. (3.37) to write out a consistency relation for the order parameter as calculated only from the remaining entrained population.

Assuming an equilibrium of the system, such that the order parameter is at a fixed point, the drifting agents must form a stationary distribution on \mathcal{S} . We denote this distribution by $f(\boldsymbol{\sigma}, \mathbf{W})$, which is analogous to $f(\boldsymbol{\sigma}, \boldsymbol{\omega}, t)$ defined in Eq. (3.22). Since the velocity of each agent is governed by Eq. (3.6), stationarity of the distribution requires that $f(\boldsymbol{\sigma}, \mathbf{W})$ is inversely proportional to the magnitude of this velocity. Hence

$$f(\boldsymbol{\sigma}, \mathbf{W}) = \frac{C(\mathbf{W}, K\rho)}{|K[\boldsymbol{\rho} - (\boldsymbol{\rho} \cdot \boldsymbol{\sigma})\boldsymbol{\sigma}] + \mathbf{W}\boldsymbol{\sigma}|}, \quad (3.39)$$

where $C(\mathbf{W}, K\rho)$ is a normalization constant,

$$\int_{|\sigma|=1} f(\sigma, \mathbf{W}) d\sigma = 1 \quad (3.40)$$

for each \mathbf{W} not in Γ . Since Γ is invariant to the transformation $\mathbf{W} \rightarrow -\mathbf{W}$, it follows from the definition of $C(\mathbf{W}, K\rho)$ that it must also be invariant to $\mathbf{W} \rightarrow -\mathbf{W}$. The contribution to the order parameter from the drifting population is then given by

$$\rho_{\text{drift}} = \int_{|\sigma|=1} \int_{\mathbf{W} \notin \Gamma} \sigma \frac{C(\mathbf{W}, K\rho)}{|K[\rho - (\rho \cdot \sigma)\sigma] + \mathbf{W}\sigma|} G(\mathbf{W}) d\mathbf{W} d\sigma.$$

Applying the variable transformations of $\sigma \rightarrow -\sigma$ and $\mathbf{W} \rightarrow -\mathbf{W}$ we obtain $\rho_{\text{drift}} = -\rho_{\text{drift}}$, and hence $|\rho_{\text{drift}}| = 0$.

Thus, the only contribution to the order parameter is from the entrained population of agents. Let $H(\gamma) = 1$ give rise to some solution $(\rho \cdot \sigma^F) = \gamma \equiv \gamma(\{\omega_i\}, \{\rho_i\})$. Then, dotting both sides of Eq. (3.5) with ρ in the limit of infinite system size gives

$$|\rho|^2 = \int_{\Gamma} \gamma(\{\omega_i\}, \{\rho_i\}) G(\mathbf{W}) d\mathbf{W}. \quad (3.41)$$

As in the two-dimensional case, the critical coupling strength, K_c , will be such that the magnitude of the order parameter is infinitesimally small but nonzero. We can use this to determine a value of the critical coupling as

$$K_c = \frac{2}{\pi \tilde{g}(0)}, \quad (3.42)$$

where

$$\tilde{g}(0) = \int_{-\infty}^{\infty} \dots \int_{-\infty}^{\infty} g(0, \omega_2, \dots, \omega_\Lambda) d\omega_2 \dots d\omega_\Lambda, \quad (3.43)$$

and $g(\omega_1, \dots, \omega_\Lambda)$ is the joint distribution of natural frequencies associated with the distribution \mathbf{W} (see Appendix A.3 for details). Note that, for our particular choice of an antisymmetric matrix ensemble from which we randomly draw the \mathbf{W}_i (i.e., independently Gaussian upper-triangular matrix elements), there are known results for g and \tilde{g} from random matrix theory. In particular, Ref. [76] yields²

$$\tilde{g}(0) = \frac{1}{D} \sqrt{\frac{2}{\pi}} \sum_{n=0}^{(D/2)-1} \frac{(2n)!}{2^{2n} (n!)^2}. \quad (3.44)$$

The predictions for the critical coupling strength, K_c , made according to Eqs. (3.42) and (3.44) for $D = 2, 4, 6$ and 8 have been marked by vertical arrows in Fig. 3.4(a). We expect that with increasing N the numerically observed transitions will appear to be sharper at the marked critical coupling strength. Note that continuing the curve from large values of $|\rho|$ to the x -axis without changing its curvature (as would be expected from the shape of the phase transition curve in $D = 2$; see Fig. 3.1) approximates the predicted values accurately.

3.4 Model variant: Extended-body agents in three dimensions

From Eq. (3.2), the dynamics of the system of agents can be thought of resulting from the interplay of two terms, $K[\boldsymbol{\rho} - (\boldsymbol{\rho} \cdot \boldsymbol{\sigma}_i)\boldsymbol{\sigma}_i]$, promoting coherence

²In comparing the equation in Ref. [76], with our numerical results, we observe that there appears to be a misprint of a factor of $1/(D\sqrt{2})$ in their expression

among agents, and $\mathbf{W}_i\boldsymbol{\sigma}_i$, promoting decoherence between agents. We have shown that the competition between these two opposing tendencies is resolved by a critical transition from incoherence to coherence that is qualitatively different for even and odd dimensionality (Figs. 3.1 and 3.4). In order to show that this qualitative result is not restricted to our particular assumed form of the $K = 0$ agent dynamics ($d\boldsymbol{\sigma}_i/dt = \mathbf{W}_i\boldsymbol{\sigma}_i$), we here consider a very different model with $D = 3$, and show that our conclusion for the behavior shown for the solution of Eq. (3.2) continues to apply. Specifically, we consider a different form of the dispersal term in the context of the three-dimensional dynamics of extended objects (e.g., the fish in Fig. 3.8). We will also further justify the term $\mathbf{W}_i\boldsymbol{\sigma}_i$ as a simple choice of dispersive dynamics for interacting agents.

As we discuss in Sec. 3.2, the setup of Eq. (3.2) considers interactions between agents that are fully described by a single D -dimensional unit vector. For an extended object, a single unit vector does not uniquely specify the agent state. In the specific context of three-dimensional extended objects in three-dimensional space (e.g., the dynamics of flocks of birds, swarms of drones etc.), the orientation of the extended body must be specified by two unit vectors. We call such agents extended-body agents, and describe their state via the two vectors $\boldsymbol{\sigma}$, which as earlier represents the direction of the velocity of the extended-body agent; and $\boldsymbol{\eta}$, chosen orthogonal to $\boldsymbol{\sigma}$ (see Fig. 3.8). For simplicity, we define $\boldsymbol{\nu} = \boldsymbol{\sigma} \times \boldsymbol{\eta}$ to form the right-handed orthonormal triple $\{\boldsymbol{\sigma}, \boldsymbol{\eta}, \boldsymbol{\nu}\}$. It should be noted that extended-body agents in two dimensions are completely described by a single unit vector, $\boldsymbol{\sigma}$, as in the standard $D = 2$ Kuramoto model. We will first set up the dynamics

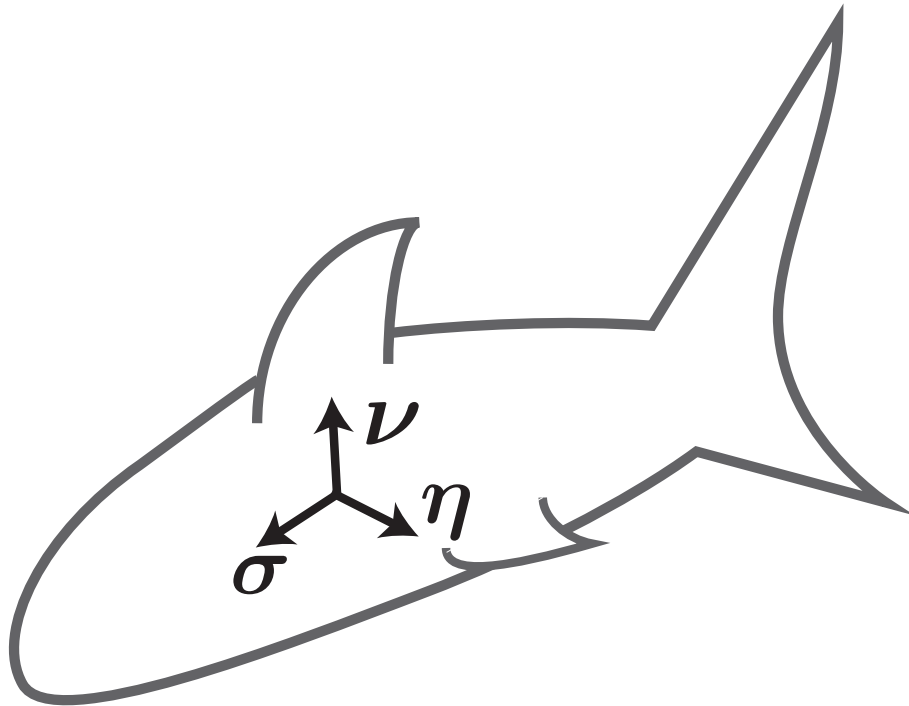


Figure 3.8: Illustration of an extended-body agent. Unlike the agents in the generalized Kuramoto model Eq. (3.2), we assume that the state of an extended-body agent cannot be described by a single unit vector σ . Rather, the pair of vectors σ and η together describe the orientation and state of the agent. The direction of agent velocity is assumed to be along the direction σ as earlier. The unit vector ν is defined as $\nu = \sigma \times \eta$

of this extended-body agent when it is not coupled to other agents. Motivated by the uncoupled dynamics of this extended-body agent representing some fixed errors/biases, we assume that the uncoupled dynamics of this extended-body agent is autonomous, i.e., not explicitly dependent on time. Under this assumption, we write

$$\begin{aligned}
d\boldsymbol{\sigma}/dt &= \Phi(\boldsymbol{\sigma}, \boldsymbol{\eta}), \\
d\boldsymbol{\eta}/dt &= \Psi(\boldsymbol{\sigma}, \boldsymbol{\eta}), \\
d\boldsymbol{\nu}/dt &= \Theta(\boldsymbol{\sigma}, \boldsymbol{\eta}) = \Phi \times \boldsymbol{\eta} + \boldsymbol{\sigma} \times \Psi.
\end{aligned}
\tag{3.45}$$

Further, we make the natural assumption that the dynamics do not depend on information of its orientation with respect to any fixed frame of reference, i.e., there is no ‘special’ direction in space that determines the dynamics of the extended-body agent. Thus,

$$\Phi(\mathbf{R}\boldsymbol{\sigma}, \mathbf{R}\boldsymbol{\eta}) = \mathbf{R}\Phi(\boldsymbol{\sigma}, \boldsymbol{\eta}), \tag{3.46}$$

$$\Psi(\mathbf{R}\boldsymbol{\sigma}, \mathbf{R}\boldsymbol{\eta}) = \mathbf{R}\Psi(\boldsymbol{\sigma}, \boldsymbol{\eta}), \tag{3.47}$$

$$\Theta(\mathbf{R}\boldsymbol{\sigma}, \mathbf{R}\boldsymbol{\eta}) = \mathbf{R}\Theta(\boldsymbol{\sigma}, \boldsymbol{\eta}), \tag{3.48}$$

for any rotation matrix \mathbf{R} . Since the unit vectors $\{\boldsymbol{\sigma}, \boldsymbol{\eta}, \boldsymbol{\nu}\}$ form an orthonormal

basis, we can write the vector field Φ in this basis,

$$\Phi(\boldsymbol{\sigma}, \boldsymbol{\eta}) = a(\boldsymbol{\sigma}, \boldsymbol{\eta})\boldsymbol{\sigma} + b(\boldsymbol{\sigma}, \boldsymbol{\eta})\boldsymbol{\eta} + c(\boldsymbol{\sigma}, \boldsymbol{\eta})\boldsymbol{\nu}. \quad (3.49)$$

Using Eq. (3.46),

$$\begin{aligned} a(\mathbf{R}\boldsymbol{\sigma}, \mathbf{R}\boldsymbol{\eta})\mathbf{R}\boldsymbol{\sigma} + b(\mathbf{R}\boldsymbol{\sigma}, \mathbf{R}\boldsymbol{\eta})\mathbf{R}\boldsymbol{\eta} + c(\mathbf{R}\boldsymbol{\sigma}, \mathbf{R}\boldsymbol{\eta})\mathbf{R}\boldsymbol{\nu} \\ = \mathbf{R}[a(\boldsymbol{\sigma}, \boldsymbol{\eta})\boldsymbol{\sigma} + b(\boldsymbol{\sigma}, \boldsymbol{\eta})\boldsymbol{\eta} + c(\boldsymbol{\sigma}, \boldsymbol{\eta})\boldsymbol{\nu}]. \end{aligned} \quad (3.50)$$

Comparing components along $\mathbf{R}\boldsymbol{\sigma}$ on both sides of the above equation,

$$a(\mathbf{R}\boldsymbol{\sigma}, \mathbf{R}\boldsymbol{\eta}) = a(\boldsymbol{\sigma}, \boldsymbol{\eta}), \quad (3.51)$$

and hence the scalar $a(\boldsymbol{\sigma}, \boldsymbol{\eta})$ must be independent of $\boldsymbol{\sigma}$ and $\boldsymbol{\eta}$, $a(\boldsymbol{\sigma}, \boldsymbol{\eta}) = a$. Similarly, $b(\boldsymbol{\sigma}, \boldsymbol{\eta})$ and $c(\boldsymbol{\sigma}, \boldsymbol{\eta})$ must also be independent of $\boldsymbol{\sigma}$ and $\boldsymbol{\eta}$. Applying similar reasoning to all the components of $\Phi(\boldsymbol{\sigma}, \boldsymbol{\eta})$, $\Psi(\boldsymbol{\sigma}, \boldsymbol{\eta})$ and $\Theta(\boldsymbol{\sigma}, \boldsymbol{\eta})$, we see that they must each be linear functions of $\boldsymbol{\sigma}$, $\boldsymbol{\eta}$ and $\boldsymbol{\nu}$. Hence [noting that $\mathbf{R}\boldsymbol{\nu} = (\mathbf{R}\boldsymbol{\sigma}) \times (\mathbf{R}\boldsymbol{\eta})$]

$$\begin{aligned} \Phi(\boldsymbol{\sigma}, \boldsymbol{\eta}) &= a\boldsymbol{\sigma} + b\boldsymbol{\eta} + c\boldsymbol{\nu}, \\ \Psi(\boldsymbol{\sigma}, \boldsymbol{\eta}) &= a'\boldsymbol{\sigma} + b'\boldsymbol{\eta} + c'\boldsymbol{\nu}, \\ \Theta(\boldsymbol{\sigma}, \boldsymbol{\eta}) &= a''\boldsymbol{\sigma} + b''\boldsymbol{\eta} + c''\boldsymbol{\nu}. \end{aligned} \quad (3.52)$$

Further, since $\{\boldsymbol{\sigma}, \boldsymbol{\eta}, \boldsymbol{\nu}\}$ are unit vectors forming a right-handed triple,

$$\boldsymbol{\sigma} \cdot \boldsymbol{\Phi} = \boldsymbol{\eta} \cdot \boldsymbol{\Psi} = \boldsymbol{\nu} \cdot \boldsymbol{\Theta} = 0, \quad (3.53)$$

and, using $d/dt(\boldsymbol{\sigma} \cdot \boldsymbol{\eta}) = d/dt(\boldsymbol{\sigma} \cdot \boldsymbol{\nu}) = d/dt(\boldsymbol{\eta} \cdot \boldsymbol{\nu}) = 0$,

$$\boldsymbol{\sigma} \cdot \boldsymbol{\Psi} + \boldsymbol{\eta} \cdot \boldsymbol{\Phi} = \boldsymbol{\sigma} \cdot \boldsymbol{\Theta} + \boldsymbol{\nu} \cdot \boldsymbol{\Phi} = \boldsymbol{\eta} \cdot \boldsymbol{\Theta} + \boldsymbol{\nu} \cdot \boldsymbol{\Psi} = 0. \quad (3.54)$$

Thus, Eqs. (3.52) reduce to

$$\begin{aligned} d\boldsymbol{\sigma}/dt &= \boldsymbol{\Phi}(\boldsymbol{\sigma}, \boldsymbol{\eta}) = -\alpha\boldsymbol{\eta} + \beta\boldsymbol{\nu}, \\ d\boldsymbol{\eta}/dt &= \boldsymbol{\Psi}(\boldsymbol{\sigma}, \boldsymbol{\eta}) = \alpha\boldsymbol{\sigma} + \gamma\boldsymbol{\nu}, \\ d\boldsymbol{\nu}/dt &= \boldsymbol{\Theta}(\boldsymbol{\sigma}, \boldsymbol{\eta}) = -\beta\boldsymbol{\sigma} - \gamma\boldsymbol{\eta}. \end{aligned} \quad (3.55)$$

for some scalar, extended-body-agent specific quantities α , β and γ . Having specified the uncoupled dynamics of an extended-body agent, we add the effect of inter-agent coupling, in the form of the Kuramoto-like interactions described in Sec. 3.2. Thus, analogous to Eq. (3.2), we write

$$\frac{d\boldsymbol{\sigma}_i}{dt} = K[\boldsymbol{\rho} - (\boldsymbol{\rho} \cdot \boldsymbol{\sigma}_i)\boldsymbol{\sigma}_i] + \Phi_i(\boldsymbol{\sigma}_i, \boldsymbol{\eta}_i), \quad (3.56)$$

where $\boldsymbol{\rho}$ is given by Eq. (3.5), which is the average of the velocity directions $\boldsymbol{\sigma}_i$ of each extended-body agent. Note that this form of coupling treats $\boldsymbol{\sigma}$ as a special direction as compared to $\boldsymbol{\eta}$ and $\boldsymbol{\nu}$, since we assume that the goal of the swarm is to

maintain coherence via coupling that aligns the velocity direction $\boldsymbol{\sigma}_i$ of each agent i to the motion of the swarm as a whole. We then write $\boldsymbol{\eta}_i$ and $\boldsymbol{\nu}_i$ such that the constraint Eqs. (3.53) and (3.54) continue to hold for the coupled system and that $K = 0$ corresponds to Eqs. (3.45).

$$d\boldsymbol{\eta}_i/dt = -K[\boldsymbol{\rho} \cdot \boldsymbol{\eta}_i]\boldsymbol{\sigma}_i + \Psi_i(\boldsymbol{\sigma}_i, \boldsymbol{\eta}_i), \quad (3.57)$$

$$d\boldsymbol{\nu}_i/dt = -K[\boldsymbol{\rho} \cdot \boldsymbol{\nu}_i]\boldsymbol{\sigma}_i + \Theta_i(\boldsymbol{\sigma}_i, \boldsymbol{\eta}_i). \quad (3.58)$$

We perform a simulation of $N = 10^4$ such extended-body agents by numerically integrating Eqs. (3.56), (3.57) and (3.58) for a range of values of K similar to Fig. 3.4. Since the dynamics captured by the Eqs. (3.45) represent random biases/errors, we choose the quantities α , β and γ for each agent from independent, normal distributions with zero mean and unit variance. In Fig. 3.9 we present the phase transition displayed by this system of evolving extended-body agents. For each value of K we numerically integrate the system until $|\boldsymbol{\rho}|$ reaches a steady-state value. Note that we continue to observe a discontinuous transition of $|\boldsymbol{\rho}|$ as K increases through 0. Further, we also numerically observed that if α , β and γ are chosen anisotropically, i.e., if they are chosen from normal distributions with zero mean but differing variance, the qualitative result shown in Fig. 3.9 does not change, i.e., the transition to coherence is still discontinuous at $K = 0$. This indicates that the phenomenon of discontinuous transitions in odd dimensions is not specific to the form of the dispersal term chosen in Eq. (3.2), rather, it is a more general phenomena occurring for a potentially wide range of systems of interacting

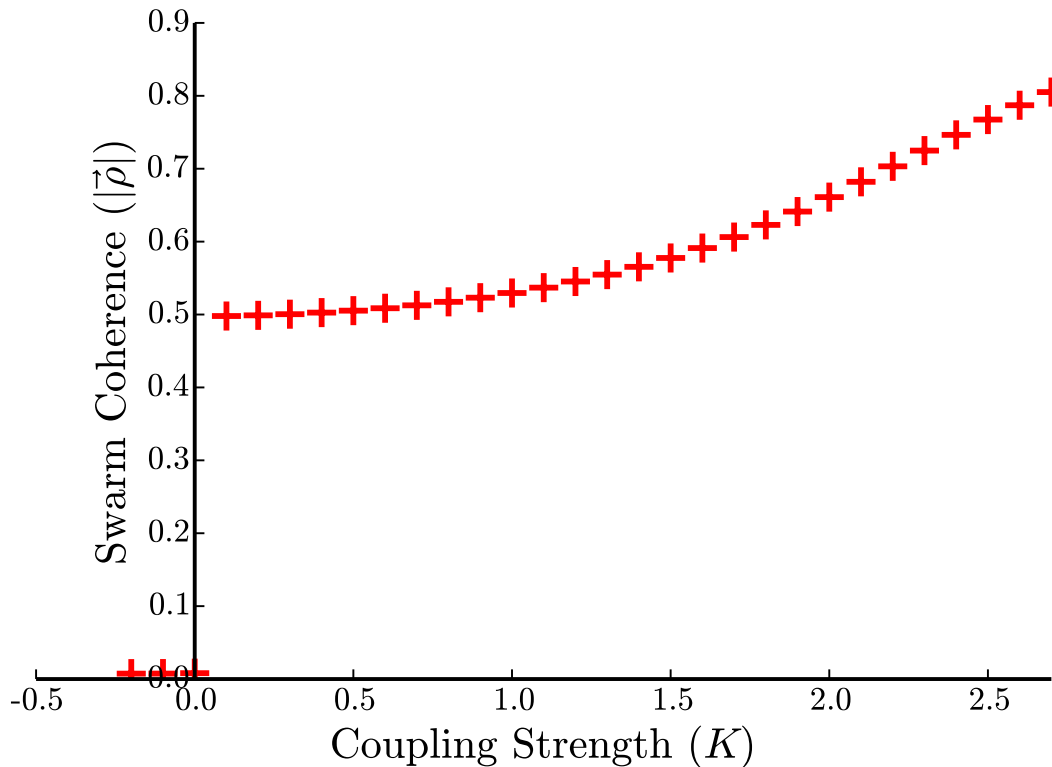


Figure 3.9: Phase transition for interacting three-dimensional extended-body agents described by Eqs. (3.56) – (3.58). The dynamics of individual agents in this system have been constructed to satisfy constraints imposed by extended-body dynamics, and are *not* equivalent to the dynamics of the generalized Kuramoto model described in Sec.3.3. Despite this, we continue to observe a discontinuous jump in the asymptotic steady-state value of $|\rho|$ as K is increased through 0.

agents in odd dimensions. In contrast, this model for two dimensions ($\beta = \gamma = 0$) is the same as the original Kuramoto model and hence has a continuous transition to coherence at a critical positive value of K .

To further examine the dynamics of the uncoupled agents Eqs. (3.55), we adopt notation where we represent Eqs. (3.55) as

$$\frac{d}{dt} \begin{pmatrix} \sigma & \eta & \nu \end{pmatrix} = \begin{pmatrix} \sigma & \eta & \nu \end{pmatrix} \mathbf{U}, \quad (3.59)$$

where \mathbf{U} is the 3×3 antisymmetric matrix,

$$\mathbf{U} = \begin{pmatrix} 0 & \alpha & -\beta \\ -\alpha & 0 & -\gamma \\ \beta & \gamma & 0 \end{pmatrix}, \quad (3.60)$$

and $\begin{pmatrix} \boldsymbol{\sigma} & \boldsymbol{\eta} & \boldsymbol{\nu} \end{pmatrix}$ represents a 3×3 matrix whose columns are the vectors $\boldsymbol{\sigma}$, $\boldsymbol{\eta}$ and $\boldsymbol{\nu}$. We can then consider a change of basis \mathbf{R} such that

$$\mathbf{R}^T \mathbf{U} \mathbf{R} = \begin{pmatrix} 0 & \omega & 0 \\ -\omega & 0 & 0 \\ 0 & 0 & 0 \end{pmatrix}, \quad (3.61)$$

where $\omega^2 = \alpha^2 + \beta^2 + \gamma^2$. Using the same convention as Eq. (3.59), we define the orthonormal triple of unit vectors $\{\mathbf{u}, \mathbf{v}, \mathbf{w}\}$ as

$$\begin{pmatrix} \mathbf{u} & \mathbf{v} & \mathbf{w} \end{pmatrix} = \begin{pmatrix} \boldsymbol{\sigma} & \boldsymbol{\eta} & \boldsymbol{\nu} \end{pmatrix} \mathbf{R}. \quad (3.62)$$

Thus Eq. (3.59) becomes

$$\begin{aligned} d\mathbf{u}/dt &= \omega \mathbf{v}, \\ d\mathbf{v}/dt &= -\omega \mathbf{u}, \\ d\mathbf{w}/dt &= 0. \end{aligned} \quad (3.63)$$

According to Eqs. (3.63), the vectors \mathbf{u} and \mathbf{v} , which are fixed linear combinations of $\boldsymbol{\sigma}$, $\boldsymbol{\eta}$ and $\boldsymbol{\nu}$, undergo uniform rotation with an angular frequency of ω about the axis \mathbf{w} . Since $\boldsymbol{\sigma}$, $\boldsymbol{\eta}$ and $\boldsymbol{\nu}$ describe the physical orientation of the uncoupled extended-body agent, the extended-body agent will demonstrate dynamics that correspond to rotations in three dimensions, and there will exist a \mathbf{W} such that $\dot{\boldsymbol{\sigma}} = \mathbf{W}\boldsymbol{\sigma}$. In particular, the axis of this rotation will be along the unit vector \mathbf{w} given by $\mathbf{w} = R_{13}\boldsymbol{\sigma} + R_{23}\boldsymbol{\eta} + R_{33}\boldsymbol{\nu}$, where R_{ij} is the ij^{th} component of \mathbf{R} . Since $\dot{\mathbf{w}} = 0$,

$$\mathbf{w} = R_{13}\boldsymbol{\sigma}(0) + R_{23}\boldsymbol{\eta}(0) + R_{33}\boldsymbol{\nu}(0).$$

Note that \mathbf{R} (and hence its components) is dependent on the random biases/systematic errors present, arising from the particular form of Φ and Ψ , whereas $\boldsymbol{\sigma}(0)$, $\boldsymbol{\eta}(0)$ and $\boldsymbol{\nu}(0) = \boldsymbol{\sigma}(0) \times \boldsymbol{\eta}(0)$ depends on the initial orientation/state of the extended-body agent. Thus the axis of rotation is dependent on the initial state of the extended-body agent, while the frequency of rotation, ω is determined solely by the random systematic errors of the extended-body agent [i.e., α , β and γ in Eq. (3.55)].

Thus, under the assumptions made above, the dynamics of uncoupled extended-body agents can be described as $\dot{\boldsymbol{\sigma}} = \mathbf{W}\boldsymbol{\sigma}$ for some initial-condition-dependent \mathbf{W} (in particular, $\mathbf{W}\boldsymbol{\sigma} = -\omega\mathbf{w} \times \boldsymbol{\sigma}$). Note however that this is *not* identical to the uncoupled dynamics of the agents described in Eq. (3.2). In particular, the axis of rotation of the extended-body agent under the dynamics described here is along the vector \mathbf{w} , which is determined by the initial conditions of the extended-body agent state ($\boldsymbol{\sigma}(0)$, $\boldsymbol{\eta}(0)$). However, in the uncoupled dynamics of the generalized Ku-

ramoto agents described by Eq. (3.2) the axis of rotation is predetermined by the rotation matrix \mathbf{W}_i assigned to agent i and is independent of the initial condition chosen for the agent. An isotropic ensemble of rotation matrices for the generalized Kuramoto agents in the case of extended-body agents corresponds to an ‘isotropic’ distribution of the extended-body agent parameters (α, β, γ) , as well as isotropic initial conditions of the extended-body agents.

Further, this simple interpretation of σ undergoing uniform rotation no longer holds for the case of coupled extended-body agents, and Eqs. (3.56), (3.57) and (3.58) cannot be simply written in the form of Eq. (3.2) with an initial-condition-dependent \mathbf{W} for arbitrary K (this, however, is possible in the limit of $K \rightarrow 0$ or $|\rho| \rightarrow 0$, hence our results for the stability analysis of the $|\rho|=0$ state will recreate the phase transitions in higher dimensions). The qualitative dynamics of coupled extended-body agents and coupled generalized Kuramoto agents described by Eq. (3.2) are in general distinct, yet our main point of discontinuous phase transitions for odd dimensions at $K = 0$ continues to hold.

Thus, for the case of extended-body agents, under the assumptions made in this section, rotation matrices as dispersal terms arise naturally as simple error/fixed-bias terms for the individual agents. Rather than considering the case of initial-condition-dependent rotation matrices, in Eq. (3.2) we have considered the simplification of choosing fixed rotation matrices \mathbf{W} . This motivates the generalization of the Kuramoto model presented in Eq. (3.2) as a simple model to capture the dynamics of swarming and flocking agents. Further, we also see that the result obtained from our toy model Eq. (3.2) for the qualitative continuous or discontinuous

behavior of the incoherent-to-coherent transition continues to hold for other three-dimensional agent dynamics, such as the extended-body agent dynamics described in this section.

In Sec. 5.5 we briefly describe other extensions and variants to the generalized Kuramoto model described in Sec. 3.2.

3.5 Discussion and conclusions

We have considered a generalization of the Kuramoto model to arbitrary dimensions, describing a system of interacting, orientable units, whose state is completely described by D -dimensional unit vectors. Our main result (Fig. 3.4) is that the macroscopic dynamics of the Kuramoto model is strongly dependent on the dimensionality of the system, with odd-dimensional systems behaving similar to one other, and likewise for even-dimensional systems. For odd-dimensional systems, including the practically important case of $D = 3$, we find that the phase transition from incoherence to partially coherent states occurs via a discontinuous, nonhysteretic transition as the coupling strength K increases through 0 (Sec. 3.3.1, also see Fig. 3.6). In contrast, even-dimensional systems, like $D = 2$, numerically appear to undergo continuous transitions of the coherence at a critical coupling strength $K_c > 0$ (Fig. 3.4 (a)). We also note that, unlike the two-dimensional Kuramoto model, the state of the system is not always completely classified by the magnitude of the order parameter. In particular, for the two-dimensional Kuramoto model there is a single stable incoherent steady-state distribution in the infinite size

limit ($f = 1/(2\pi)$), whereas the three-dimensional Kuramoto model has an infinite number of such distributions (for example, Eq. (3.24)) each with different stability properties (see Eq. (3.32)). By considering a setup of extended-body agents, in Sec. 3.4 we further motivated our choice of model Eq. (3.2) in the context of swarms of drones or flocks of birds. In particular, we demonstrated that our qualitative results relating to the difference between odd- and even-dimensional systems continue to hold for models that use a different choice of the dispersal term. This study of extended-body agents in Sec. 3.4 also explains why the choice of the dispersal term $\mathbf{W}\boldsymbol{\sigma}$ in the context of the qualitative phase transitions observed for $D = 3$ is justified .

While other authors [71,72] have also studied the Kuramoto model generalized to higher dimensions, their consideration has been limited to the case of identical natural rotations. Our setup of the problem (i.e., with heterogeneous natural rotations) by setting $G(\mathbf{W}) = \delta(\mathbf{W} - \mathbf{W}_0)$ reproduces the results in Refs. [71,72] for the case of globally coupled systems (here we interpret the Dirac delta function acting on the antisymmetric matrix \mathbf{W} as the product of Dirac delta functions acting on each of the upper-triangular elements of the matrix individually). This heterogeneous setup of the problem now describes the interplay of two opposing tendencies, i.e., the tendency for agent states to align due to the inter-agent coupling, *and* the tendency for agents to disperse themselves in opposition to such alignment. This leads to the possibility of new and interesting phenomena such as the difference between the odd and even dimensionality described in this chapter.

In addition to the variant described in Sec. 3.4, the setup of the generalized

Kuramoto model given by Eqs. (3.6) and (3.5) can be modified and generalized in various ways. An interesting question for possible future study is whether a striking difference between odd and even dimensions (as we have found for the generalized Kuramoto model and its variant in Sec. 3.4) manifests in these modifications. For example, beyond the globally coupled systems we have considered, one might consider network-based coupling, wherein agent j influences agent i with a strength A_{ij} . This is equivalent replacing $\boldsymbol{\rho}$ in Eq. (3.6) with $\boldsymbol{\rho}_i$, where

$$\boldsymbol{\rho}_i = \frac{1}{N} \sum_j A_{ij} \boldsymbol{\sigma}_j.$$

In the context of swarms of drones, a further natural generalization would be to have the network-based coupling A_{ij} depend on the spatial distance and relative orientation between the i^{th} and j^{th} swarm agent.

As discussed earlier, for positive K the dynamics of each $\boldsymbol{\sigma}_i$ are attracted towards the average state of the system, $\boldsymbol{\rho}$. This could be interpreted as a target direction for each $\boldsymbol{\sigma}_i$, and can be generalized by replacing Eq. (3.5) by other definitions of $\boldsymbol{\rho}$. For example, in the context of swarms of drones, it could be desirable for the orientation of the drones to be biased towards the plane of the horizon, or to be biased toward the direction of a given target destination. To achieve this, the ‘target direction’, $\boldsymbol{\rho}$ in Eq. (3.6) could be modified from the average state of the system to the average state biased towards a given target. Studying the dependence of the dynamics of such swarms of agents on modifications to $\boldsymbol{\rho}$ (via either the presence of network dependent interaction, or other bias targets) would be an interesting line

of future research.

In Chapter 5 we will present a mathematical formulation for studying the D -dimensional Kuramoto model in the infinite size limit via a generalization of the Ott-Antonsen ansatz [18,19], wherein we will also address the issue of generalization of ρ .

Chapter 4: Observing Microscopic Transitions from Macroscopic Bursts:
Instability-Mediated Resetting in the Incoherent Regime
of the D -dimensional Generalized Kuramoto Model

The dynamical phase transition from incoherence to coherence for a recently proposed, higher-dimensional generalization of the Kuramoto model, is examined from the point of view of the stability of the incoherent state. It is found that, due to the higher dimensionality, there is a continuum of different possible pretransition incoherent equilibrium states, each with distinct stability properties. This, in turn, leads to a novel phenomenon, which we call ‘Instability-Mediated Resetting,’ which enables the existence of a unique critical transition point in spite of the infinite continuum of possible pretransition states. In general, these results provide an example illustrating that, for systems with a large number of entities described via a macroscopic variable(s), a degeneracy of microscopic states corresponding to the same macroscopic variable may occur, and that signatures of such a degeneracy may be observable in the transient macroscopic system dynamics.

4.1 Introduction

4.1.1 Background

Motivated by a host of applications, much recent research has been focused on efforts aimed at understanding the behavior of large systems of many interacting dynamical agents. An important tool elucidating issues in this general area has been the study of simplified paradigmatic models. A prime example of such a model is the Kuramoto model [2, 9, 16, 17],

$$d\theta_i/dt = \omega_i + \frac{K}{N} \sum_{j=1}^N \sin(\theta_j - \theta_i), \quad (4.1)$$

where N is the number of agents ($i = 1, 2, \dots, N$), θ_i is an angle variable that specifies the state of agent i , the parameter K characterizes the coupling strength, and ω_i is the natural frequency of agent i ($\dot{\theta}_i = \omega_i$ in the absence of coupling), where ω_i is typically chosen randomly for each i from some distribution function $g(\omega)$ ($\int g(\omega)d\omega = 1$). Because the parameter ω_i characterizing the dynamics of each agent i is different for each agent, the agents are said to be heterogeneous. This model and its many generalizations have been used to study a wide variety of applications and phenomena. Examples include synchronously flashing fireflies [77], cellular clocks in the brain [46], Josephson junction circuits [39], pedestrian-induced oscillation of foot bridges [78], and motion direction alignment in large groups of agents (e.g., drones or flocking animals) [79–81], among many others. In the first

four of these examples θ_i represents the phase angle of an oscillation experienced by agent i , while, in contrast, in the fifth example, θ_i specifies the direction in which agent i moves.

One aspect of the Kuramoto model and its previous generalizations is that the state of agent i is given by the single scalar angle variable $\theta_i(t)$. Recently, a generalization of these models has been introduced in which the state of the agent i is a D -dimensional unit vector, $\boldsymbol{\sigma}_i(t)$, thus allowing for more degrees of freedom in the dynamics of the individual agents. In this generalized model the D -dimensional unit vector, $\boldsymbol{\sigma}_i(t)$, is taken to evolve according to the real equation [72, 82] (see Chapter 3),

$$d\boldsymbol{\sigma}_i/dt = K[\boldsymbol{\rho} - (\boldsymbol{\rho} \cdot \boldsymbol{\sigma}_i)\boldsymbol{\sigma}_i] + \mathbf{W}_i\boldsymbol{\sigma}_i, \quad (4.2)$$

where the D -dimensional vector $\boldsymbol{\rho}(t)$ (to be specified subsequently) is a common field felt by all the agents, and \mathbf{W}_i (analogous to ω_i in Eq. (4.1)) is a $D \times D$ antisymmetric matrix ($\mathbf{W}_i^T = -\mathbf{W}_i$) which we refer to as the rotation rate matrix. Note that for $K = 0$ Eq. (4.1) becomes $\dot{\boldsymbol{\sigma}}_i = \mathbf{W}_i\boldsymbol{\sigma}_i$ which represents a uniform rate of rotation of $\boldsymbol{\sigma}_i$ in D -dimensional space, $\boldsymbol{\sigma}_i(t) = [\exp(\mathbf{W}_i t)]\boldsymbol{\sigma}_i(0)$, analogous to the action of the frequency ω_i in $D = 2$. Dotting Eq. (4.2) with $\boldsymbol{\sigma}_i$, we obtain $d|\boldsymbol{\sigma}_i|^2/dt = 0$, as required by our designation of $\boldsymbol{\sigma}_i$ as a unit vector. In general, depending on the situation to be modeled, $\boldsymbol{\rho}(t)$ can be chosen in different ways [18] (see also Chapter 3). In this chapter we focus on the simplest interesting choice,

$$\boldsymbol{\rho}(t) = \frac{1}{N} \sum_{i=1}^N \boldsymbol{\sigma}_i(t), \quad (4.3)$$

and we call $|\rho(t)|$, the ‘order parameter.’ We note that, as shown in Chapter 3, Eqs. (4.2) and (5.16) reduce to Eq. (4.1) for $D = 2$ with

$$\boldsymbol{\sigma}_i = \begin{pmatrix} \cos \theta_i \\ \sin \theta_i \end{pmatrix} \text{ and } \mathbf{W}_i = \begin{pmatrix} 0 & -\omega_i \\ \omega_i & 0 \end{pmatrix},$$

thus justifying Eqs. (4.2) and (5.16) as a ‘generalization’ of the Kuramoto model, Eq. (4.1), to higher dimensionality. One motivation for this generalization is the previously mentioned example of the application of Eq. (4.1) to model motion alignment in flocks: For $D = 2$ (equivalent to the standard Kuramoto case, Eq. (4.1)) the direction of agent motion (characterized by the scalar angle θ_i or the unit vector $(\cos \theta_i \sin \theta_i)^T$) can be described for agents moving along a two-dimensional surface (like the surface of the Earth), while, if the agents are, e.g., moving in three dimensions (as for drones flying in the air), then the direction of an agent’s motion ($\boldsymbol{\sigma}_i$ for agent i) is necessarily given by a three-dimensional unit vector. In addition, Ref. [82] has considered the dynamics of the vector $\boldsymbol{\sigma}_i$ as characterizing the evolution of the opinions of an individual within a group of interacting individuals as the group evolves towards consensus. Another interesting point, as discussed in Chapter 3 is that the inter-agent coupling for Eqs. (4.2) and (5.16) is the same as that for the classical, mean-field, zero-temperature, Heisenberg model for the evolution of N interacting spin states $\boldsymbol{\sigma}_i$ in the presence of frozen-in random site disorder (the terms $\mathbf{W}_i \boldsymbol{\sigma}_i$, with \mathbf{W}_i randomly chosen).

Based Chapter 3 we view Eqs. (4.2) and (5.16) as the simplest D -dimensional

generalization of the Kuramoto model subject to the assumption that the state of any agent is a unit vector. See Sec. IV of Chapter 3 for a generalization, motivated by flocking drones, in which the agents are regarded as D -dimensional extended-body agents whose states of orientation are described by $(D - 1)$ mutually perpendicular unit vectors. Although the model in Sec. IV of Chapter 3 is quite different from that considered here, Chapter 3 shows that it shares the same qualitative type of transition behavior as Eq. (4.2). Thus we conjecture that the model we study in the present chapter can provide a general guide to the possible behavior of other related systems.

4.1.2 The Rotation Rates \mathbf{W}_i

Equation (4.2) with zero rotation rate ($\mathbf{W}_i = 0$) or a uniform rotation rate ($\mathbf{W}_i = \mathbf{W}$) was introduced in Refs. [72,82]. The generalization to heterogeneous rotation rates (the situation to be considered in the present chapter) makes Eq. (4.2) more similar to the original Kuramoto model and widens its range of applicability. In what follows, as in Chapter 3, we assume that the rotation rate matrix \mathbf{W}_i is randomly generated for each i , by choosing each of its $D(D - 1)/2$ upper triangular matrix elements, $w_{pq}^{(i)}$ (with $p < q$), independently from a zero-mean, Gaussian distribution function as described in Sec. 4.2. Alternately, we can say that each of the \mathbf{W}_i is randomly drawn from the ensemble of random antisymmetric matrices corresponding to the Gaussian distribution. It is important to note that this ensemble is invariant under rotations; i.e., the ensemble is unchanged when every matrix in the

ensemble is subjected to the same rotation, $\mathbf{W} \rightarrow \mathbf{R}\mathbf{W}$, for any orthogonal matrix \mathbf{R} (e.g., Ref. [76]).

4.1.3 The $N \rightarrow \infty$ limit and the multiplicity of incoherent equilibria

We are interested in the case where $N \gg 1$, and, to facilitate analysis, we consider the limit $N \rightarrow \infty$, for which we characterize the system state for dimensionality D by a distribution function $F(\mathbf{W}, \boldsymbol{\sigma}, t)$ such that the fraction of the agents lying in the differential volume element $d\boldsymbol{\sigma}d\mathbf{W}$ centered at $(\boldsymbol{\sigma}, \mathbf{W})$ in $\boldsymbol{\sigma}$ - \mathbf{W} space is $F(\mathbf{W}, \boldsymbol{\sigma}, t)d\boldsymbol{\sigma}d\mathbf{W}$ at time t . We define an incoherent equilibrium distribution to be such that $\partial F/\partial t = 0$ and $|\boldsymbol{\rho}| = 0$, where, since we consider the limit $N \rightarrow \infty$, Eq. (5.16) is replaced by

$$\boldsymbol{\rho}(t) = \int \int F(\mathbf{W}, \boldsymbol{\sigma}, t) \boldsymbol{\sigma} d\boldsymbol{\sigma} d\mathbf{W}. \quad (4.4)$$

As shown in Sec.4.2, for $D > 2$ there is an infinite continuum of equilibrium (i.e., time-independent) distribution functions F for which $|\boldsymbol{\rho}| = 0$. We can think of these distributions as defining a manifold \mathcal{M} in the space of distribution functions.

Within this manifold, a given F is neutrally stable to a perturbation δF such that $F + \delta F$ also lies in \mathcal{M} . Section 4.3 is devoted to an analysis of the stability of the manifold \mathcal{M} ; i.e., what happens if δF , the perturbation to F , is transverse to \mathcal{M} . Before discussing what we find in Sec. 4.3 for the case $D > 2$, it is first useful to recall the well-known results for the original Kuramoto model, corresponding to $D = 2$, as well as relevant results from Chapter 3 for $D > 2$.

4.1.4 The Dynamical phase transition

In the case of the original ($D = 2$) Kuramoto model, Eq. (4.1), for $N \rightarrow \infty$ one can consider a distribution function in (ω, θ) ; i.e., $F(\mathbf{W}, \boldsymbol{\sigma}, t) \rightarrow f(\omega, \theta, t)$. In this $D = 2$ case, in contrast to the $D > 2$ generalized model, Eq. (4.2), there is only one $|\boldsymbol{\rho}| = 0$ equilibrium distribution function, namely $f = g(\omega)/(2\pi)$. Furthermore, it has long been well-established for $D = 2$, that, as K increases continuously from zero, the long-time ($t \rightarrow \infty$) stable value of the order parameter $|\boldsymbol{\rho}|$ undergoes a continuous transition from incoherence ($|\boldsymbol{\rho}| = 0$) to partial coherence ($0 < |\boldsymbol{\rho}| < 1$) as K passes a critical value that depends on $g(\omega)$, see the green curve marked by the star symbols in Fig. 4.1. We denote this critical value by $K_c^{(+)}$. This transition has been studied from two different points of view (see Refs. [2, 9, 16, 17]):

Method (i): It is assumed that f reaches a steady-state distribution ($\partial f / \partial t = 0$) and the resulting nonlinear equation for f is then analytically solved, yielding two possible solutions for the order parameter $|\boldsymbol{\rho}|$; one has $|\boldsymbol{\rho}| = 0$ and corresponds to $f = g(\omega)/(2\pi)$; the other satisfies a transcendental equation for $|\boldsymbol{\rho}|$ as a function of K involving an integral of the ω -distribution function g . Taking g to be continuous, unimodal, symmetric, and peaked at $\omega = 0$, the transcendental root for $|\boldsymbol{\rho}|$ only exists for $K \geq K_c^{(+)} > 0$ and gives the $|\boldsymbol{\rho}| > 0$ branch in Fig. 4.1. In this approach, an analytical result for $K_c^{(+)}$ is obtained by taking the limit $|\boldsymbol{\rho}| \rightarrow 0^+$ in the expression for the transcendental branch. This is the approach originally taken by Kuramoto, who then essentially assumed that the $|\boldsymbol{\rho}| = 0$ branch applies for $K \leq K_c^{(+)}$, and the $|\boldsymbol{\rho}| > 0$ branch applies for $K > K_c^{(+)}$.

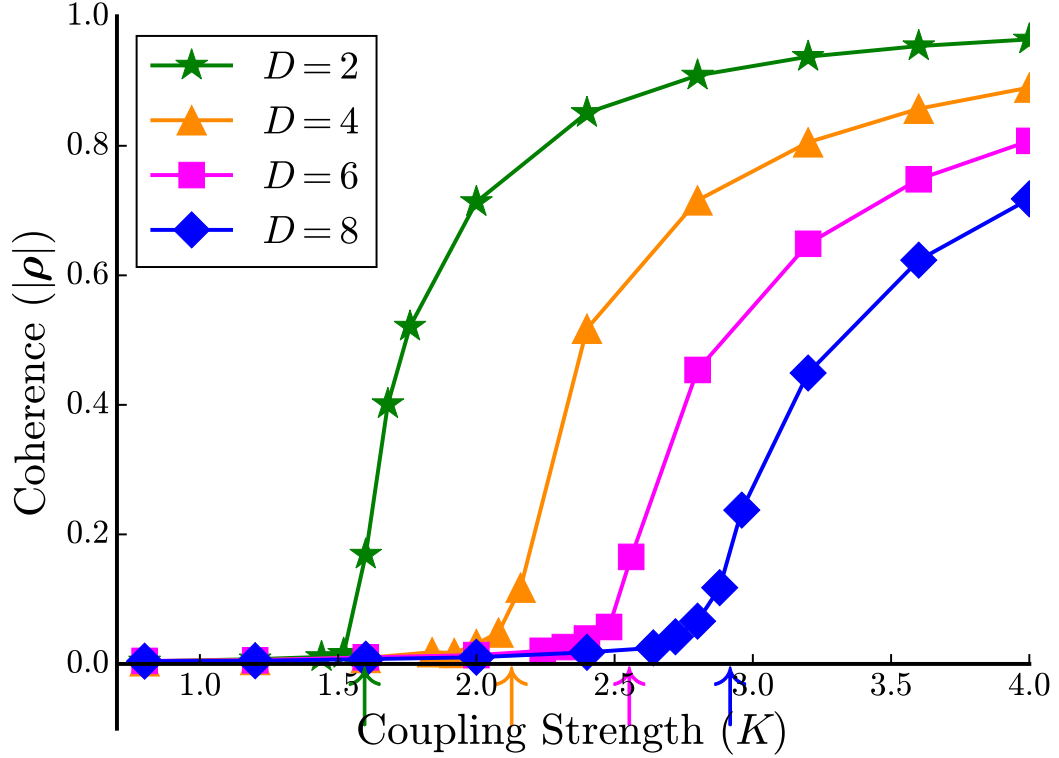


Figure 4.1: Dynamical Phase Transition for the Generalized Kuramoto model for $D = 2$ (green stars), 4 (orange triangles), 6 (magenta squares) and 8 (blue diamonds) dimensions. The $|\rho|$ values indicated by the plotted markers are obtained by choosing the values of $\sigma_i(t = 0)$ and \mathbf{W}_i for each of the $N = 10^5$ agents randomly (where the probability distribution of $\sigma_i(0)$ is isotropic in direction and that of \mathbf{W}_i is as given in Sec. 4.2) and then integrating Eq. (4.2) from each such initial condition until $|\rho(t)|$ attains a steady value. These steady state values attained appeared to be independent of this choice of initial condition. The theoretical predictions from Chapter 3 for the critical coupling strength, $K_c^{(+)}$, above which stable $|\rho| > 0$ steady states exist are indicated by correspondingly colored vertical arrows on the x -axis.

Method (ii): Considering the $|\rho|=0$ equilibrium distribution, a linear stability analysis was applied [2, 9, 16, 17, 83], and it was found that the $|\rho|=0$ equilibrium distribution (which exists for *all* K) becomes unstable when K increases through a critical value which is the same as that found for $K_c^{(+)}$ by method (i).

Thus the value of $K_c^{(+)}$ for the original Kuramoto problem can be obtained straightforwardly by following either method (i) or method (ii).

In Chapter 3 using Method (i), previously employed for the original Kuramoto problem, analysis giving the critical transition values for even D were obtained. These values are indicated by the vertical arrows in Fig. 4.1, and agree well with the plotted numerical results.

Parenthetically, we note that for odd $D \geq 3$, which is *not* considered in this chapter, the transition is qualitatively different from that shown in Fig. 4.1. Namely, as shown in Chapter 3, when D is odd, as K increases from negative values through zero there is a discontinuous jump in the coherence $|\rho|$.

4.1.5 Linear Stability of the incoherent equilibria

Motivated by the results in Fig. 4.1, in Sec. 4.3 we report results of a stability analysis of the incoherent equilibria for even D greater than two. That is, we attempt an analysis similar to method (ii), previously applied to the original Kuramoto model. We find that the straightforward correspondence that applies for $D = 2$ between the method (i) result for $K_c^{(+)}$ and the method (ii) stability result does not hold for $D = 4, 6, 8 \dots$, and that the apparent paradox presented by this finding is

resolved by a novel phenomenon that we call *Instability-Mediated Resetting* (IMR).

Specifically, our stability analysis in Sec. 4.3 applied to the infinity of possible incoherent equilibrium distributions found in Sec. 4.2, shows that different incoherent equilibria have different stability properties. Considering one such incoherent equilibrium, as K increases, the equilibrium will become unstable as K passes through some value K_c which depends on the specific incoherent equilibrium considered. There are thus many possible values of K_c , in fact we find a continuum of such K_c values spanning a range between $(K_c^{(+)}/2)$ and $K_c^{(+)}$.

4.1.6 Instability-Mediated Resetting (IMR)

These stability results for $D = 4, 6, \dots$ suggest the following question. How can instability of incoherent equilibrium distributions for $K < K_c^{(+)}$ be reconciled with the numerical results of Fig. 4.1 and the corresponding method (i) analytical results (the vertical arrows in Fig. 4.1)? The answer to this question is given in Sec. 4.4 which reports the following results on the nonlinear evolution of the instability found in Sec. 4.3: Considering an incoherent equilibrium which becomes unstable at $K = K_c < K_c^{(+)}$, if one starts with $K < K_c$ and then rapidly increases K to lie in the range $K_c < K < K_c^{(+)}$, the order parameter $|\rho|$ initially experiences growth consistent with the existence of instability. This growth, however, slows as $|\rho|$ reaches a maximum, and subsequently decays back to zero. But, after this short-lived macroscopic burst, once $|\rho|$ returns to essentially zero the resulting incoherent equilibrium is different from that which existed before the instability occurred, and this resulting

new incoherent equilibrium loses stability only at a value of the coupling strength between the value that K has been increased to and $K_c^{(+)}$.

In fact, if the initial burst occurred due to a value of K roughly in the middle of the range $K_c < K < K_c^{(+)}$, the resulting equilibrium may be one which loses stability only at $K_c^{(+)}$ itself, i.e., upon further increase of K , $|\rho|$ remains near zero until K increases past $K_c^{(+)}$. If K is suddenly increased through $K_c^{(+)}$ there is unstable growth of $|\rho|$, as for when K is increased suddenly through K_c , but now $|\rho|$ asymptotically approaches a positive value consistent with Fig. 4.1 for $K > K_c^{(+)}$. The essential point is that the instability for $K_c < K < K_c^{(+)}$ resets the equilibrium to one which is stable for $K < K_c^{(+)}$ and becomes unstable only when K exceeds $K_c^{(+)}$, consistent with the plot (Fig. 4.1) of the $t \rightarrow \infty$ order parameter vs K . This is the IMR phenomenon previously referred to.

4.1.7 Main points of this chapter

This chapter focuses on the case of even dimensional generalizations of the Kuramoto model of the form Eq. (4.2). A main message of this chapter is that, although the curves, $|\rho(t \rightarrow \infty)|$ versus K plotted in Fig. 4.1 for $D = 4, 6, \dots$, are qualitatively similar to the curve for $D = 2$, the transient dynamics of $\rho(t)$ starting from a given incoherent distribution at $t = 0$ are surprisingly different for even $D \geq 4$ as compared with $D = 2$. We will demonstrate in Sec. 4.2 that for even $D > 2$, in contrast to $D = 2$, there is an infinite continuum of incoherent stable equilibria in the limit of $N \rightarrow \infty$. In Sec. 4.3 we will perform a linear stability analysis

of these equilibria, and show that these equilibria have different critical coupling strengths, i.e., values of K beyond which the equilibria are unstable. Further, we also show that in a continuous range of K , each value of K corresponds to the critical coupling strength of some incoherent equilibrium. The upper limit of this range corresponds to earlier results for the critical coupling strength for the $t \rightarrow \infty$ macroscopic phase transition of the order parameter shown in Fig. 4.1. To reconcile these lower values of critical stability coupling strengths for incoherent equilibria, with the phase transition of Fig. 4.1, we will examine the dynamics of the incoherent equilibria beyond their critical coupling strengths. This examination results in the observation of short-lived macroscopic bursts of $|\boldsymbol{\rho}|$ which lead to the phenomenon of Instability-Mediated Resetting, which we demonstrate and describe in Sec. 4.4. We also discuss the effect of finite N on the evolution of these incoherent equilibria in Sec. 4.4.

4.2 Incoherent Equilibria

We reiterate that in this chapter we will only consider the case of even D . For each \mathbf{W} there are $D/2$ two-dimensional invariant subspaces for the $|\boldsymbol{\rho}|=0$ evolution equation

$$d\boldsymbol{\sigma}/dt = \mathbf{W}\boldsymbol{\sigma}. \quad (4.5)$$

Thus, for each k ,

$$C_k = (\widetilde{\mathbf{P}}_k \widetilde{\boldsymbol{\sigma}})^T (\widetilde{\mathbf{P}}_k \widetilde{\boldsymbol{\sigma}}) = \boldsymbol{\sigma}^T \mathbf{P}_k^T \mathbf{P}_k \boldsymbol{\sigma} = \boldsymbol{\sigma}^T \mathbf{P}_k \boldsymbol{\sigma} \quad (4.8)$$

is a constant of motion for the $|\boldsymbol{\rho}|=0$ evolution equation $d\boldsymbol{\sigma}/dt = \mathbf{W}\boldsymbol{\sigma}$.

Since we are interested in the case where the number of agents, N , is large, $N \gg 1$, it is appropriate to simplify the analysis by considering the limit $N \rightarrow \infty$, in which case the state of the system can be described by a distribution function, $F(\mathbf{W}, \boldsymbol{\sigma}, t)$ satisfying

$$\partial F / \partial t + \nabla_S \cdot (\mathbf{v}F) = 0, \quad \mathbf{v} = K[\mathbf{1}_D - \boldsymbol{\sigma}\boldsymbol{\sigma}^T]\boldsymbol{\rho} + \mathbf{W}\boldsymbol{\sigma}, \quad (4.9)$$

where $\nabla_S \cdot (\mathbf{v}F)$ represents the divergence of the vector field $\mathbf{v}F$ on the spherical surface $|\boldsymbol{\sigma}|=1$. Hence any time independent distribution function, $\overline{F}_0(\mathbf{W}, \boldsymbol{\sigma})$, for the $|\boldsymbol{\rho}|=0$ dynamics must satisfy

$$\nabla_S \cdot [(\mathbf{W}\boldsymbol{\sigma})\overline{F}_0] = (\mathbf{W}\boldsymbol{\sigma}) \cdot \nabla_S \overline{F}_0 = 0, \quad (4.10)$$

where ∇_S represents the gradient operator on the spherical surface $|\boldsymbol{\sigma}|=1$. The first equality follows from the fact that $\nabla_S \cdot (\mathbf{W}\boldsymbol{\sigma}) = 0$ for \mathbf{W} an antisymmetric matrix. Since

$$0 = dC_k/dt = \nabla_S C_k(\boldsymbol{\sigma}) \cdot d\boldsymbol{\sigma}/dt = (\mathbf{W}\boldsymbol{\sigma}) \cdot \nabla_S C_k(\boldsymbol{\sigma}), \quad (4.11)$$

by comparing Eqs. (4.10) and (4.11), we see that the most general solution for a time-independent distribution \overline{F}_0 is

$$\overline{F}_0(\mathbf{W}, \boldsymbol{\sigma}) = F_0(\mathbf{W}; C_1, \dots, C_{D/2}) = F_0(\mathbf{W}, \mathbf{c}), \quad (4.12)$$

where \mathbf{c} denotes the $(D/2)$ -vector $(C_1, \dots, C_{D/2})^T$, i.e., \overline{F}_0 depends on \mathbf{W} and the $(D/2)$ constants of the motion. There are two constraints. The first one is that, since $|\boldsymbol{\sigma}| = 1$, we have that $|\mathbf{c}| = 1$. The second constraint is that

$$0 = \boldsymbol{\rho}_0 = \int \int_{|\boldsymbol{\sigma}|=1} \boldsymbol{\sigma} \overline{F}_0(\mathbf{W}, \boldsymbol{\sigma}) d\mathbf{W} d\boldsymbol{\sigma}, \quad (4.13)$$

which is automatically satisfied if, as we henceforth assume, \overline{F}_0 is isotropic in the sense that

$$\overline{F}_0(\mathbf{R}^T \mathbf{W} \mathbf{R}, \mathbf{R} \boldsymbol{\sigma}) = \overline{F}_0(\mathbf{W}, \boldsymbol{\sigma}) \quad (4.14)$$

for any rotation matrix \mathbf{R} . Thus

$$F_0(\mathbf{R}^T \mathbf{W} \mathbf{R}, \mathbf{c}) = F_0(\mathbf{W}, \mathbf{c}), \quad (4.15)$$

since the constants C_k are invariant to such rotations. Equation (4.13) for $\boldsymbol{\rho}_0$ then yields $\boldsymbol{\rho}_0 = \mathbf{R} \boldsymbol{\rho}_0$ for any rotation \mathbf{R} , which then implies that the integral $\int \boldsymbol{\sigma} \overline{F}_0 d\mathbf{W} d\boldsymbol{\sigma} = 0$, as required by our definition of an incoherent distribution, Eq. (4.13).

In our work we consider the case where the marginal distribution of \mathbf{W} ex-

pressed in terms of the matrix elements

$$w_{ii} = 0, \quad w_{ij} = -w_{ji} \quad (4.16)$$

is Gaussian. That is,

$$\begin{aligned} G(\mathbf{W})d\mathbf{W} &= \left[\int_{|\boldsymbol{\sigma}|=1} F_0(\mathbf{W}, \mathbf{c})d\boldsymbol{\sigma} \right] d\mathbf{W} \\ &= \prod_{j=1}^D \prod_{i>j}^D g_M(w_{ij})dw_{ij}, \end{aligned} \quad (4.17)$$

where $g_M(w)$ is the Gaussian distribution

$$g_M(w) = \frac{1}{\sqrt{2\pi\langle w^2 \rangle}} e^{-\frac{w^2}{2\langle w^2 \rangle}}, \quad \langle w^2 \rangle = \int_{-\infty}^{\infty} w^2 g_M(w)dw. \quad (4.18)$$

Thus

$$G(\mathbf{W}) = (2\pi\langle w^2 \rangle)^{-D(D-1)/4} \exp \left[-\text{Trace}(\mathbf{W}^T \mathbf{W}) / (4\langle w^2 \rangle) \right]. \quad (4.19)$$

Since $\text{Trace}(\mathbf{W}^T \mathbf{W}) = -\text{Trace}(\mathbf{W}^2)$ is invariant to rotations of \mathbf{W} (i.e., $\mathbf{W} \rightarrow \mathbf{R}^T \mathbf{W} \mathbf{R}$) and $d\mathbf{W} = d(\mathbf{R} \mathbf{W})$ (since $\det(\mathbf{R})=1$), we see that $G(\mathbf{W})$ as defined above is isotropic in the sense that

$$G(\mathbf{W}) = G(\mathbf{R}^T \mathbf{W} \mathbf{R}) \quad (4.20)$$

for any $D \times D$ rotation matrix \mathbf{R} .

According to random matrix theory, the distribution of block frequencies ω_k in Eq. (4.6) for such a Gaussian ensemble of even-dimensional random antisymmetric

matrices with $\langle w^2 \rangle$ set to 1 is [76]

$$\begin{aligned} & \tilde{g}(\omega_1, \dots, \omega_{D/2}) \\ &= \kappa \prod_{1 \leq j \leq k \leq D/2} (\omega_j^2 - \omega_k^2)^2 \exp \left(- \sum_{i=1}^{D/2} \omega_i^2 / 2 \right), \end{aligned} \quad (4.21)$$

where κ is a constant chosen to ensure that the integral of the distribution $\tilde{g}(\omega_1, \dots, \omega_{D/2})$ is normalized to 1. Note that \tilde{g} is symmetric to interchanges of any two of its arguments.

As an aside, we also mention that using Eq. (4.6), $\mathbf{W} = \mathbf{R}_D \widetilde{\mathbf{W}} \mathbf{R}_D^T$, an alternative representation of $G(\mathbf{W}) d\mathbf{W}$ is

$$\tilde{g}(\omega_1, \dots, \omega_{D/2}) d\omega_1 \dots d\omega_{D/2} d\mu(\mathbf{R}_D),$$

where μ is the Haar measure for $D \times D$ rotation matrices. (The Haar measure for rotation matrices essentially gives a formal rigorous specification of what we loosely refer to as isotropy [84]. In what follows we use our informal notion of ‘isotropy’ and do not invoke Haar measures.)

Returning to the distribution function F_0 , we define \hat{F}_0 by

$$F_0(\mathbf{W}, \mathbf{c}) = G(\mathbf{W}) \hat{F}_0(\mathbf{W}, \mathbf{c}), \quad (4.22)$$

where

$$\int \hat{F}_0(\mathbf{W}, \mathbf{c}) \delta(|\boldsymbol{\sigma}| - 1) d\boldsymbol{\sigma} = 1. \quad (4.23)$$

Note that $|\boldsymbol{\sigma}|^2 = C_1 + \dots + C_{D/2} = 1$. Clearly, even with $G(\mathbf{W})$ specified as Gaussian,

there is still an infinity of choices for \hat{F}_0 and hence F_0 . These choices specify how $\boldsymbol{\sigma}$ is distributed over the $D/2$ subspaces of \mathbf{W} that are invariant for the $|\boldsymbol{\rho}|=0$ dynamics of $\boldsymbol{\sigma}$.

4.3 Stability of incoherent equilibria

We linearize Eq. (4.2) about distributions corresponding to incoherent equilibria, i.e., $|\boldsymbol{\rho}|=0$, by setting $\boldsymbol{\sigma} = \boldsymbol{\sigma}_0 + \delta\boldsymbol{\sigma}$ and $\boldsymbol{\rho} = \delta\boldsymbol{\rho}$ for small perturbations $\delta\boldsymbol{\sigma}$ and $\delta\boldsymbol{\rho}$. This yields,

$$d\boldsymbol{\sigma}_0/dt = \mathbf{W}\boldsymbol{\sigma}_0, \quad (4.24)$$

$$d\delta\boldsymbol{\sigma}/dt = K[\mathbf{1} - \boldsymbol{\sigma}_0\boldsymbol{\sigma}_0^T]\delta\boldsymbol{\rho} + \mathbf{W}\delta\boldsymbol{\sigma}. \quad (4.25)$$

Transforming Eq. (4.24) to the basis that block-diagonalizes \mathbf{W} (as in Eq. (4.6)), we obtain

$$d\tilde{\boldsymbol{\sigma}}_0/dt = \tilde{\mathbf{W}}\tilde{\boldsymbol{\sigma}}_0. \quad (4.26)$$

Thus each two-dimensional subspace k will undergo independent rotation with frequencies corresponding to real ω_k frequencies of $\tilde{\mathbf{W}}$. This gives the solution

$$\tilde{\boldsymbol{\sigma}}_0(t) = \mathbf{Q}(t)\tilde{\boldsymbol{\sigma}}_0(0), \quad (4.27)$$

to a given incoherent equilibrium characterized by $\hat{F}_0(\mathbf{W}, \mathbf{c})$. Thus

$$\delta \boldsymbol{\rho}(t) = \langle \langle \delta \boldsymbol{\sigma}(t) \rangle_{\boldsymbol{\sigma}_0(0)} \rangle_{\mathbf{W}}, \quad (4.32)$$

where $\langle \bullet \rangle_{\boldsymbol{\sigma}_0(0)}$ denotes an average over $\boldsymbol{\sigma}_0(0)$ at fixed \mathbf{W} , and $\langle \bullet \rangle_{\mathbf{W}}$ denotes an average over \mathbf{W} . We first average Eq. (4.31) over $\boldsymbol{\sigma}_0(0)$:

$$\langle \delta \boldsymbol{\sigma}(t) \rangle_{\boldsymbol{\sigma}_0(0)} = K \left\{ \int_{-\infty}^t e^{\mathbf{W}(t-\tau)} [\mathbb{1} - \langle \boldsymbol{\sigma}_0(\tau) \boldsymbol{\sigma}_0(\tau)^T \rangle_{\boldsymbol{\sigma}_0(0)}] e^{s\tau} d\tau \right\} \delta \boldsymbol{\rho}(0). \quad (4.33)$$

We focus on the evaluation of the term

$$\langle \boldsymbol{\sigma}_0(\tau) \boldsymbol{\sigma}_0(\tau)^T \rangle_{\boldsymbol{\sigma}_0(0)} \quad (4.34)$$

$$= \mathbf{R}_D \langle \tilde{\boldsymbol{\sigma}}_0(\tau) \tilde{\boldsymbol{\sigma}}_0(\tau)^T \rangle_{\boldsymbol{\sigma}_0(0)} \mathbf{R}_D^T, \quad (4.35)$$

$$= \mathbf{R}_D \left[\int_{|\boldsymbol{\sigma}|=1} \hat{F}_0(\mathbf{W}, \mathbf{c}) \tilde{\boldsymbol{\sigma}}_0(\tau) \tilde{\boldsymbol{\sigma}}_0(\tau)^T d\boldsymbol{\sigma} \right] \mathbf{R}_D^T. \quad (4.36)$$

Note that $\boldsymbol{\sigma}_0 \boldsymbol{\sigma}_0^T$ is a $D \times D$ matrix which can be constructed from $(D/2) \times (D/2)$ blocks of 2×2 matrices, where the block at index (k, l) will be $\mathbf{x}_k \mathbf{x}_l^T$ for $1 \leq k, l \leq D/2$. Defining $\mathbf{x}_k(0) = (y_k^+, y_k^-)^T$, we obtain from Eq. (4.27)

$$\mathbf{x}_k(\tau) = \begin{pmatrix} y_k^+ \cos \omega_k \tau + y_k^- \sin \omega_k \tau \\ -y_k^+ \sin \omega_k \tau + y_k^- \cos \omega_k \tau \end{pmatrix}. \quad (4.37)$$

Since $C_k = (y_k^+)^2 + (y_k^-)^2$, we write

$$y_k^+ = \sqrt{C_k} \cos \theta_k, \quad y_k^- = \sqrt{C_k} \sin \theta_k. \quad (4.38)$$

Thus

$$\mathbf{x}_k(\tau) = \sqrt{C_k} \begin{pmatrix} \cos(\omega_k \tau - \theta_k) \\ \sin(\omega_k \tau - \theta_k) \end{pmatrix}. \quad (4.39)$$

We interpret the average to be performed in Eq. (4.36) as an average over θ_k and $\sqrt{C_k}$ for each k , with the differential element $d\boldsymbol{\sigma}$ transforming to $\prod_k \sqrt{C_k} d\sqrt{C_k} d\theta_k$.

Noting that $\langle \mathbf{x}_k \rangle$ averaged over θ_k is zero, we see that $\langle \mathbf{x}_k \mathbf{x}_l^T \rangle$ can only be nonzero if $k = l$. Further, in averaging $\mathbf{x}_k \mathbf{x}_k^T$, the diagonal terms corresponding to $C_k \cos^2(\omega_k \tau - \theta_k)$ and $C_k \sin^2(\omega_k \tau - \theta_k)$ will yield $(C_k/2)$ when averaged over θ_k , and the cross terms corresponding to $C_k \sin(\omega_k \tau - \theta_k) \cos(\omega_k \tau - \theta_k)$ will yield zero. Thus, we obtain

$$\langle \mathbf{x}_k \mathbf{x}_k^T \rangle_{\theta_k} = \frac{C_k}{2} \mathbb{1}_2, \quad (4.40)$$

where $\mathbb{1}_2$ represents the 2×2 identity matrix. Note that the average over θ_k removes all τ dependence in Eq. (4.36). Performing the average over C_k , we obtain

$$\langle \mathbf{x}_k \mathbf{x}_k^T \rangle_{\boldsymbol{\sigma}_0(0)} = \frac{\bar{C}_k(\mathbf{W})}{2} \mathbb{1}_2, \quad (4.41)$$

where

$$\bar{C}_k(\mathbf{W}) = \frac{\int_{\Gamma} \hat{F}_0(\mathbf{W}, \mathbf{c}) C_k d\mathbf{c}}{\int_{\Gamma} \hat{F}_0(\mathbf{W}, \mathbf{c}) d\mathbf{c}}, \quad (4.42)$$

with the domain Γ corresponding to the set of all \mathbf{c} such that $0 \leq C_k \leq 1$ for all k , and $\sum_k C_k = 1$.

Thus the quantity $\langle \boldsymbol{\sigma}_0(\tau) \boldsymbol{\sigma}_0(\tau)^T \rangle_{\boldsymbol{\sigma}_0(0)}$ in Eq. (4.35) becomes

$$\langle \boldsymbol{\sigma}_0(\tau) \boldsymbol{\sigma}_0(\tau)^T \rangle_{\boldsymbol{\sigma}_0(0)} = \mathbf{R}_D \bar{\mathbf{C}}(\mathbf{W}) \mathbf{R}_D^T, \quad (4.43)$$

where $\bar{\mathbf{C}}(\mathbf{W})$ is the D -dimensional diagonal matrix,

$$\bar{\mathbf{C}}(\mathbf{W}) = \frac{1}{2} \text{diag} [\bar{C}_1(\mathbf{W}), \bar{C}_1(\mathbf{W}), \bar{C}_2(\mathbf{W}), \bar{C}_2(\mathbf{W}), \dots, \bar{C}_{D/2}(\mathbf{W}), \bar{C}_{D/2}(\mathbf{W})].$$

Now performing the average over \mathbf{W} as prescribed in Eq. (4.32), we obtain from Eqs. (4.33) and (4.43)

$$\begin{aligned} \delta \boldsymbol{\rho}(t) &= \delta \boldsymbol{\rho}(0) e^{st} \\ &= K \left\{ \int d\mathbf{W} G(\mathbf{W}) \int_{-\infty}^t e^{\mathbf{W}(t-\tau)} \mathbf{R}_D [\mathbf{1} - \bar{\mathbf{C}}] \mathbf{R}_D^T e^{s\tau} d\tau \right\} \delta \boldsymbol{\rho}(0), \end{aligned}$$

or

$$\left\{ \mathbf{1} - K \int d\mathbf{W} G(\mathbf{W}) \int_{-\infty}^t e^{(t-\tau)(\mathbf{W}-s\mathbf{1})} \mathbf{R}_D [\mathbf{1} - \bar{\mathbf{C}}(\mathbf{W})] \mathbf{R}_D^T d\tau \right\} \delta \boldsymbol{\rho}(0) = 0.$$

Integrating over τ , we obtain

$$\left\{ \mathbf{1} - K \int d\mathbf{W} G(\mathbf{W}) (s\mathbf{1} - \mathbf{W})^{-1} \mathbf{R}_D [\mathbf{1} - \bar{\mathbf{C}}(\mathbf{W})] \mathbf{R}_D^T \right\} \delta \boldsymbol{\rho}(0) = 0.$$

Using the change of basis Eq. (4.6),

$$\left\{ \mathbf{1} - K \int d\mathbf{W} G(\mathbf{W}) \mathbf{R}_D (s\mathbf{1} - \widetilde{\mathbf{W}})^{-1} [\mathbf{1} - \bar{\mathbf{C}}(\mathbf{W})] \mathbf{R}_D^T \right\} \delta \boldsymbol{\rho}(0) = 0. \quad (4.44)$$

Since $\mathbf{R}_D(\mathbf{W}) = \mathbf{R}_D(-\mathbf{W})$, $G(\mathbf{W}) = G(-\mathbf{W})$, and by Eq. (4.15) $\bar{\mathbf{C}}(\mathbf{W}) = \bar{\mathbf{C}}(-\mathbf{W})$, we can replace the $(s\mathbf{1} - \widetilde{\mathbf{W}})^{-1}$ term in Eq. (4.44) by

$$\frac{1}{2} \left[\frac{1}{s\mathbf{1} - \widetilde{\mathbf{W}}} + \frac{1}{s\mathbf{1} + \widetilde{\mathbf{W}}} \right] = \frac{s}{s^2\mathbf{1} - \widetilde{\mathbf{W}}^2}. \quad (4.45)$$

Noting that

$$\begin{pmatrix} 0 & -\omega \\ \omega & 0 \end{pmatrix}^2 = -\omega^2 \mathbb{1}_2,$$

the quantity in Eq. (4.45) becomes

$$\begin{aligned} & H(s; \omega_1, \dots, \omega_{D/2}) \\ &= s \operatorname{diag} \left[\frac{1}{s^2 + \omega_1^2}, \frac{1}{s^2 + \omega_1^2}, \dots, \frac{1}{s^2 + \omega_{D/2}^2}, \frac{1}{s^2 + \omega_{D/2}^2} \right], \end{aligned} \quad (4.46)$$

which when inserted into Eq. (4.44), yields

$$\left\{ \mathbb{1} - K \int d\mathbf{W} G(\mathbf{W}) \mathbf{R}_D \mathbf{V} \mathbf{R}_D^T \right\} \delta \boldsymbol{\rho}(0) = 0, \quad (4.47)$$

where

$$\begin{aligned} \mathbf{V} &= H(s; \omega_1, \dots, \omega_{D/2}) [\mathbb{1} - \bar{\mathbf{C}}(\mathbf{W})] \\ &= s \operatorname{diag} \left[\frac{1 - \frac{\bar{C}_1}{2}}{s^2 + \omega_1^2}, \frac{1 - \frac{\bar{C}_1}{2}}{s^2 + \omega_1^2}, \right. \\ &\quad \left. \dots, \frac{1 - \frac{\bar{C}_{D/2}}{2}}{s^2 + \omega_{D/2}^2}, \frac{1 - \frac{\bar{C}_{D/2}}{2}}{s^2 + \omega_{D/2}^2} \right]. \end{aligned}$$

Noting that $G(\mathbf{W})$ is isotropic in the sense of Eq. (4.20), we can average $\mathbf{R}_D \mathbf{V} \mathbf{R}_D^T$ (equivalently \mathbf{V}) over an isotropic ensemble of rotations and replace $d\mathbf{W} G(\mathbf{W})$ by the distribution of the rotation invariant quantities characterizing \mathbf{W} , i.e., $\{\omega_1, \dots, \omega_{D/2}\}$. Noting that $\operatorname{Trace}(\mathbf{V}) = \operatorname{Trace}(\mathbf{R} \mathbf{V} \mathbf{R}^T)$ for any rotation \mathbf{R} and that the average $\langle \mathbf{R} \mathbf{V} \mathbf{R}^T \rangle_{\mathbf{R}}$ over an isotropic ensemble of rotations \mathbf{R} must, by the

isotropy, be a scalar multiple of the $D \times D$ identity matrix, we obtain

$$\begin{aligned} \langle \mathbf{RVR}^T \rangle_{\mathbf{R}} &= \frac{1}{D} \text{Trace}(\mathbf{V}) \mathbf{1} \\ &= \left(\frac{2s}{D} \sum_{k=1}^{D/2} \frac{1 - \bar{C}_k(\mathbf{W})/2}{s^2 + \omega_k^2} \right) \mathbf{1}. \end{aligned} \quad (4.48)$$

Using Eqs.(4.48) and (4.21), we find that, for $\delta \boldsymbol{\rho}(0) \neq 0$, Eq. (4.47) yields the scalar equation

$$\begin{aligned} 1 - \frac{2Ks}{D} \int d\omega_1 \dots \int d\omega_{D/2} \tilde{g}(\omega_1, \dots, \omega_{D/2}) \\ \times \sum_{k=1}^{D/2} \frac{1 - \bar{C}_k(\mathbf{W})/2}{s^2 + \omega_k^2} = 0, \end{aligned} \quad (4.49)$$

where after averaging over the ensemble of rotations, we have replaced $G(\mathbf{W})d\mathbf{W}$ in Eq. (4.47) by

$$\tilde{g}(\omega_1, \dots, \omega_{D/2}) d\omega_1 \dots d\omega_{D/2},$$

with \tilde{g} being the distribution of block frequencies (Eq.(4.21)) corresponding to the distribution $G(\mathbf{W})$. Note that, by the invariance of $\hat{F}_0(\mathbf{W}, \mathbf{c})$ with respect to rotations of \mathbf{W} , although in our definition of \bar{C}_k we write $\bar{C}_k \equiv \bar{C}_k(\mathbf{W})$ (see Eq. (4.42)), we can more specifically write it as a function only of the rotation invariant block frequencies $\{\omega_1, \dots, \omega_{D/2}\}$ characterizing \mathbf{W} :

$$\bar{C}_k(\mathbf{W}) \rightarrow \bar{C}_k(\omega_1, \dots, \omega_{D/2}).$$

Due to the isotropy of the ensemble of matrices \mathbf{W} , the function $\bar{C}_k(\omega_1, \dots, \omega_{D/2})$

will be invariant to any swapping of indices, i.e.,

$$\bar{C}_k(\omega_1, \dots, \omega_k, \dots, \omega_{D/2}) = \bar{C}_1(\omega_k, \dots, \omega_1, \dots, \omega_{D/2}),$$

for all k . Since \tilde{g} is also invariant to swapping of its arguments (see Eq. (4.21)), we obtain

$$\begin{aligned} 1 - Ks \int d\omega_1 \dots \int d\omega_{D/2} \tilde{g}(\omega_1, \dots, \omega_{D/2}) \\ \times \frac{1 - \bar{C}_1(\omega_1, \dots, \omega_k, \dots, \omega_{D/2})/2}{s^2 + \omega_1^2} = 0, \end{aligned} \quad (4.50)$$

To obtain K_c , the critical coupling constant at instability onset, we consider the limit $\text{Re}(s) \rightarrow 0$ from $\text{Re}(s) > 0$. Denoting the real and imaginary parts of s by p and q respectively, we hence consider the limit of $s = p + iq \rightarrow iq$ from $p > 0$.

Note that

$$\begin{aligned} \lim_{p \rightarrow 0^+} \frac{s}{s^2 + \omega_1^2} &= \lim_{p \rightarrow 0^+} \frac{1}{2} \left\{ \frac{-i}{\omega_1 - i(p + iq)} + \frac{i}{\omega_1 + i(p + iq)} \right\} \\ &= \pi[\delta(\omega_1 + q) + \delta(\omega_1 - q)]/2 \end{aligned} \quad (4.51)$$

$$-i\mathcal{PV} \left\{ \frac{1}{\omega_1 + q} - \frac{1}{\omega_1 - q} \right\}, \quad (4.52)$$

where $\delta(x)$ represents the Dirac delta function at x and \mathcal{PV} represents the Cauchy

Principal value of the integral over ω_1 . Thus we find from Eq. (4.49) that

$$\begin{aligned}
& 1 - K_c(q) \\
& \times \left\{ (\pi/2) \int \tilde{g}(\omega_1, \dots, \omega_{D/2}) [1 - \bar{C}_1(\omega_1, \dots, \omega_{D/2})/2] \right. \\
& \times [\delta(\omega_1 + q) + \delta(\omega_1 - q)] \prod_{j=1}^{D/2} d\omega_j \\
& - i\mathcal{PV} \int \tilde{g}(\omega_1, \dots, \omega_{D/2}) [1 - \bar{C}_1(\omega_1, \dots, \omega_{D/2})/2] \\
& \left. \times \left[\frac{1}{\omega_1 + q} - \frac{1}{\omega_1 - q} \right] \prod_{j=1}^{D/2} d\omega_j \right\} = 0,
\end{aligned} \tag{4.53}$$

where $K_c(q)$ is the critical coupling strength at which a small perturbation to the distribution F_0 begins to have an unstable mode growing as e^{st} with $\text{Im}(s) = q$. Given our choice of an isotropic ensemble of rotation matrices \mathbf{W} , the functions \tilde{g} and \bar{C}_1 must be even functions in each of their arguments. Further, since $K_c(q)$ represents a coupling strength, it must be real. Thus, from the real and imaginary parts of Eq. (4.53) we obtain

$$\begin{aligned}
K_c(q) = \frac{1}{\pi} & \left[\int \tilde{g}(q, \omega_2, \dots, \omega_{D/2}) \right. \\
& \left. \times [1 - \bar{C}_1(q, \omega_2, \dots, \omega_{D/2})/2] \prod_{j \geq 2} d\omega_j \right]^{-1},
\end{aligned} \tag{4.54}$$

and

$$\begin{aligned}
0 = \mathcal{PV} & \int \tilde{g}(\omega_1, \dots, \omega_{D/2}) [1 - \bar{C}_1(\omega_1, \dots, \omega_{D/2})/2] \\
& \times \left[\frac{1}{\omega_1 + q} - \frac{1}{\omega_1 - q} \right] \prod_{j=1}^{D/2} d\omega_j.
\end{aligned} \tag{4.55}$$

Using Eq. (4.54) the above expression reduces to

$$0 = \mathcal{PV} \int \frac{d\omega_1}{(\omega_1 + q)K_c(\omega_1)} - \mathcal{PV} \int \frac{d\omega_1}{(\omega_1 - q)K_c(\omega_1)}. \tag{4.56}$$

For a given distribution $\tilde{g}(\omega_1, \dots, \omega_{D/2})$ and a given $\bar{C}_1(\omega_1, \dots, \omega_{D/2})$, Eq. (4.56) can be solved to obtain a set of solutions for q , which we denote as \mathcal{Q} . Note that $q = 0 \in \mathcal{Q}$. The q dependence of K_c indicates that for each value of $q \in \mathcal{Q}$ there exists a mode of instability that arises at the corresponding value of $K_c(q)$. However, the critical coupling strength K_c of a distribution F_0 is the smallest value of K for which there is an unstable mode. Thus

$$K_c = \min_{q \in \mathcal{Q}} K_c(q). \quad (4.57)$$

For notational convenience we define

$$h(\omega) = \int d\omega_2 \dots \int d\omega_{D/2} \tilde{g}(\omega, \omega_2, \dots, \omega_{D/2}). \quad (4.58)$$

Recalling Eq. (4.42), we see that \bar{C}_1 is the expected value of the fraction of $|\sigma_i|^2$ lying in the first invariant subspace of \mathbf{W} . Hence, for $D \geq 4$,

$$0 \leq \bar{C}_1(\omega_1, \dots, \omega_{D/2}) \leq 1$$

for all realizations of \mathbf{W} . For the case of $D = 2$ (i.e., the standard Kuramoto model) there is only a single frequency associated with \mathbf{W} , and hence $\bar{C}_1 = 1$. Thus, Eq. (4.54) shows that $K_c(q)$ must lie in the range

$$\frac{1}{\pi h(q)} \leq K_c(q) \leq \frac{2}{\pi h(q)}. \quad (4.59)$$

Following the form of \tilde{g} given in Eq. (4.21), we observe that $h(q)$ is maximized at $q = 0 \in \mathcal{Q}$. Thus, minimizing each of the three terms in the above inequality over $q \in \mathcal{Q}$,

$$0 \leq K_c^{(-)} = \frac{1}{\pi h(0)} \leq K_c \leq K_c^{(+)} = \frac{2}{\pi h(0)}. \quad (4.60)$$

Using the above inequality we make the following observations:

- For all incoherent equilibria, the corresponding K_c is greater than $K_c^{(-)}$. Thus any incoherent equilibrium will be stable for coupling strengths $K < K_c^{(-)}$
- There does not exist any incoherent equilibrium distribution whose K_c is greater than $K_c^{(+)}$. Thus, all incoherent equilibria become unstable for coupling strengths $K > K_c^{(+)}$. This is consistent with Fig. 4.1, where we see that for $K > K_c^{(+)}$ the system attains an equilibria with $|\rho| > 0$.
- For an arbitrary choice of \bar{C}_k it is not necessary that $K_c(q)$ will be minimized at $q = 0$. However, for several of the examples we consider below we will consider simple choices for \bar{C}_1 such that the minima will occur at $K_c(0)$.
- The inequality in Eq. (4.60) does not have an explicit D dependence. However, as noted above for $D = 2$, $\bar{C}_1 = 1$, resulting in a single critical coupling constant $K_c = K_c^{(+)} = 2/(\pi h(0)) = 2/(\pi \tilde{g}(0))$.

In the subsequent discussion we will consider the special case of $D = 4$ and give examples of distributions and their corresponding critical coupling strengths for the onset of instability.

Uniform σ : For each \mathbf{W}_i , the corresponding unit vector σ_i is chosen randomly with uniform probability in all directions. Thus the expected value of the magnitude squared of the projection $\sigma_i \mathbf{P}_k \sigma_i$ onto subspace k (see Eq. (4.8)) is the same for all of the $D/2$ subspaces, and, since $|\sigma_i|^2 = 1$, this expected value is $(2/D)$, i.e.,

$$\bar{C}_1 = 2/D. \quad (4.61)$$

The uniform distribution is of particular interest because of its ease of implementation in computer simulations and because of the intuitive naturalness of this choice. From Eq. (4.54) we obtain

$$\begin{aligned} K_c(q) &= \frac{1}{\pi} \left[\int \tilde{g}(q, \omega_2, \dots, \omega_{D/2}) \frac{(D-1)}{D} \prod_{j \geq 2} d\omega_j \right]^{-1}, \\ &= \frac{D}{(D-1)\pi h(q)}, \end{aligned}$$

and since $h(q)$ is minimized at $q = 0 \in \mathcal{Q}$, thus

$$K_c^{(u)} = \frac{D}{(D-1)\pi h(0)}, \quad (4.62)$$

giving $K_c^{(u)} = 4/[3\pi h(0)]$ for $D = 4$.

Minimally Stable Distribution: We define a minimally stable distribution to be one whose critical coupling constant for the onset of instability corresponds to the lower bound of Eq. (4.60), i.e., $K_c = K_c^{(-)}$. To construct such a distribution we initialize each agent arbitrarily but restricted to the subspace that is orthogonal to

the subspace corresponding to the smallest absolute value of the frequency, i.e., for each agent we set $C_{min} = 0$ where

$$C_{min} = C_k \text{ if } |\omega_k| \leq |\omega_j| \text{ for all } 1 \leq j \leq (D/2). \quad (4.63)$$

For $D = 4$ this corresponds to

$$\bar{C}_1(\omega_1, \omega_2) = \begin{cases} 0 & \text{if } |\omega_1| \leq |\omega_2|, \\ 1 & \text{if } |\omega_1| > |\omega_2|. \end{cases} \quad (4.64)$$

Note that for this distribution $\bar{C}_1(0, \omega_2) = 0$ for all ω_2 . To see why this results in a minimally stable distribution we compute the integral in Eq. (4.54) and observe that $K_c(q)$ for this distribution is minimized at $q = 0$ (see Fig. 4.2 ; For this minimally stable distribution $K_c(q)$ has been labelled as $K_c^{(min)}(q)$, shown in purple). This gives $K_c = K_c(0) = 1/(\pi h(0)) = K_c^{(-)}$.

Maximally Stable Distribution: We define a maximally stable distribution to be one whose critical coupling constant for the onset of instability corresponds to the upper bound of Eq. (4.60), i.e., $K_c = K_c^{(+)}$. In $D = 4$, such a distribution can be set up similar to the case of the minimally stable distribution, by choosing the σ_i to lie entirely in the subspace corresponding to the smallest absolute value of the

frequency, i.e., by setting $C_{min} = 1$ for each agent. This corresponds to

$$\bar{C}_1(\omega_1, \omega_2) = \begin{cases} 1 & \text{if } |\omega_1| \leq |\omega_2|, \\ 0 & \text{if } |\omega_1| > |\omega_2|. \end{cases} \quad (4.65)$$

As earlier, integration of Eq. (4.54) with the above \bar{C}_1 results in an expression for $K_c(q)$ which is again minimized at $q = 0$ (see Fig. 4.2; For this maximally stable distribution $K_c(q)$ has been labelled as $K_c^{(max)}(q)$, shown in green). This gives $K_c = K_c(0) = 2/(\pi h(0)) = K_c^{(+)}$. (An analogous construction of setting $C_{min} = 1$ for each agent does not work to construct a maximally stable distribution in $D \geq 6$. While this implies that $C_{min} = 1$ for each agent is not always a maximally stable distribution, it does *not* imply that there is no such distribution in $D \geq 6$. We leave the construction of such a distribution to future work.)

In addition to yielding an upper bound on K_c , maximally stable distributions are of particular interest because they surprisingly tend to arise naturally in our numerical simulations performed on necessarily finite system size, even when other equilibrium distributions $F_0(\mathbf{W}, \boldsymbol{\sigma})$ are initialized (e.g., when the uniform $\boldsymbol{\sigma}$ distribution is initialized); see Sec. 4.4.3. Note that it is not necessary for a maximally stable distribution to have $C_{min} = 1$ for each agent; for example, the maximally stable distributions attained due to the long-time limit of finite- N -effects as shown in Fig. 4.6 do not have $C_{min} = 1$ for each agent.

The largest possible value of the critical coupling constant, $K_c^{(+)}$, beyond which no stable incoherent equilibria exist, corresponds to the calculation of K_c performed

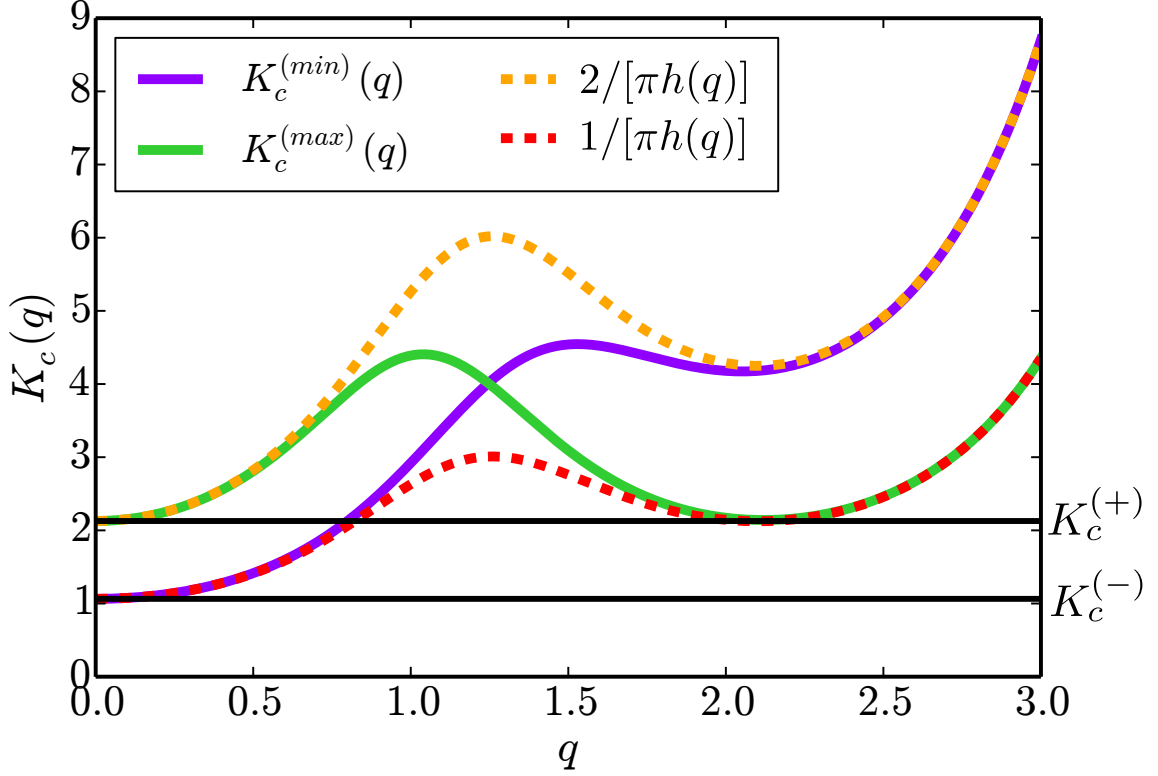


Figure 4.2: $K_c(q)$ vs q for the case of the minimally stable distribution (shown in green, labelled $K_c^{(min)}(q)$) corresponding to Eq. (4.64) and the maximally stable distribution (shown in purple, labelled $K_c^{(max)}(q)$) corresponding to Eq. (4.65) for $D = 4$. Note that $K_c(q)$ is always bounded by $1/[\pi h(q)]$ (shown as the red dashed curve) and $2/[\pi h(q)]$ (shown as the orange dashed curve) as indicated in Eq. (4.59). The critical coupling strength for the onset of instability, K_c for a given distribution is given by the minimum value attained by $K_c(q)$, which for $K_c^{(min)}(q)$ and $K_c^{(max)}(q)$ is at $q = 0$. ($K_c^{(max)}(q)$ appears to be approximately minimized at $q \approx 2.12$, corresponding to a value of $K_c(q) = 2.141$. The true minima however is at $q = 0$, corresponding to $K_c(q) = 2.128$)

	$h(0)$	$K_c^{(-)}$	$K_c^{(u)}$	$K_c^{(+)}$
$D = 2$	$(2\pi)^{-1/2}$	N/A	1.596	1.596
$D = 4$	$(3/4) \times (2\pi)^{-1/2}$	1.064	1.418	2.128
$D = 6$	$(5/8) \times (2\pi)^{-1/2}$	1.277	1.532	2.553
$D = 8$	$(35/64) \times (2\pi)^{-1/2}$	1.459	1.667	2.918

Table 4.1: Expressions for $h(0)$ and numerical values of $K_c^{(-)}$, $K_c^{(u)}$ and $K_c^{(+)}$ for $D = 2, 4, 6$ and 8 . The expression for $h(0)$ is obtained from Chapter 3, and the values of the various critical coupling strengths are obtained from Eq. (4.66)

in Chapter 3 for $D \geq 4$, as shown via the arrows marked in Fig.4.1. Thus, for $D \geq 4$ we obtain

$$K_c^{(-)} = \frac{1}{\pi h(0)} < K_c^{(u)} = \frac{D}{(D-1)\pi h(0)} < K_c^{(+)} = \frac{2}{\pi h(0)} \quad (4.66)$$

In particular, for the choice of the distribution of rotations matrices Eq. (4.19), Chapter 3, presents an expression for $h(0)$, which we use to give values of $K_c^{(-)}$, $K_c^{(u)}$ and $K_c^{(+)}$ for the cases of even $D \leq 8$ in Table 4.1.

In order to demonstrate that any K_c value between $K_c^{(-)}$ and $K_c^{(+)}$ can occur depending on the equilibrium, we consider a particular simple example: For every \mathbf{W}_i in our randomly chosen \mathbf{W} -ensemble, we determine σ_i according to either one of the three protocols specified above with probabilities $p^{(u)}$ (for the uniform case), $p^{(+)}$ (for the maximally stable case) or $p^{(-)}$ (for the minimally stable case), with

$$p^{(u)} + p^{(-)} + p^{(+)} = 1 \quad (4.67)$$

Using the expected value interpretation of \bar{C}_1 , we thus obtain from Eqs. (4.61),

(4.64) and (4.65)

$$\bar{C}_1 = \begin{cases} p^{(+)} + 2p^{(u)}/D & \text{if } |\omega_1| \leq |\omega_2|, \\ p^{(-)} + 2p^{(u)}/D & \text{if } |\omega_1| > |\omega_2|, \end{cases}$$

corresponding to

$$K_c = p^{(u)}K_c^{(u)} + p^{(+)}K_c^{(+)} + p^{(-)}K_c^{(-)}. \quad (4.68)$$

Hence for $D = 4$, by choosing values of $p^{(u,+,-)}$, we can construct a distribution to have any given value of K_c between $K_c^{(-)}$ and $K_c^{(+)}$ (We expect similar constructions to exist for all even $D \geq 4$). Furthermore, for any given K_c in the range Eq. (4.60), Eqs. (4.67) and (4.68) represent only two constraints on the three parameters, $p^{(u)}$, $p^{(-)}$ and $p^{(+)}$. Thus, for each value of K_c in the range $K_c^{(-)} < K_c < K_c^{(+)}$ there are an infinity of possible choices for $p^{(u)}$, $p^{(+)}$ and $p^{(-)}$ (i.e., an infinite number of distribution functions) satisfying Eq. (4.68).

4.4 Macroscopic bursts and Instability-Mediated Resetting

In the previous section we considered $N \rightarrow \infty$ and showed that, for even $D \geq 4$, the stability of incoherent equilibria depends on their associated equilibrium distribution function, F . In particular, we observe a range of critical parameter values K_c for instability onset from $K_c^{(-)}$ to $K_c^{(+)} = 2K_c^{(-)}$, where K_c depends on F . By definition, for any $K < K_c^{(-)}$ all incoherent distributions are stable, and for $K > K_c^{(+)}$ all incoherent distributions are unstable.

We now return to the central question posed in Sec. 4.1, namely, how can we reconcile the loss of the stability of an incoherent distribution at a critical coupling

value of $K_c < K_c^{(+)}$ with Fig. 4.1, which shows the attracting value of the magnitude of the order parameter, $|\boldsymbol{\rho}|$, characterizing the coherence of the agent population for $t \rightarrow \infty$? In particular, in Fig. 4.1, how is the time-asymptotic value for $|\boldsymbol{\rho}|$ maintained at zero for $K_c^{(-)} < K < K_c^{(+)}$ despite multiple incoherent equilibria losing their stabilities at critical coupling strengths $K_c < K$?

4.4.1 Macroscopic bursts of coherence

To examine the aforementioned question, we first consider the following setup: We initialize the system to a minimally stable incoherent equilibrium distribution by setting $C_{min} = 0$ for each agent (see Sec.4.3). This initial setup will be invariant to evolution with a coupling strength of $K < K_c^{(-)}$. We then consider a sudden increase in K to a value satisfying $K_c^{(-)} < K < K_c^{(+)}$.

The dynamics observed following this change of K is represented in Fig. 4.3(a), for a numerical simulation of $N = 10^6$ agents in $D = 4$ dimensions, initialized to the minimally stable distribution with $C_{min} = 0$, and then numerically integrated according to Eq. (4.2) with a coupling strength of $K = 1.4 > K_c^{(-)} \approx 1.064$ (see Table 4.1). In Fig. 4.3(a) we plot two quantities — in the orange solid curve we present $|\boldsymbol{\rho}(t)|$, and in the blue dashed curve we show the average value of C_{min} over all agents, $\langle C_{min} \rangle$. Note the rapid rise and fall of $|\boldsymbol{\rho}|$ which is accompanied by a change in value of $\langle C_{min} \rangle$. This rapid change in $\langle C_{min} \rangle$ indicates the evolution of the system away from the initialized incoherent distribution (constructed to have $\langle C_{min} \rangle \approx 0$) to a different incoherent distribution with a larger value of

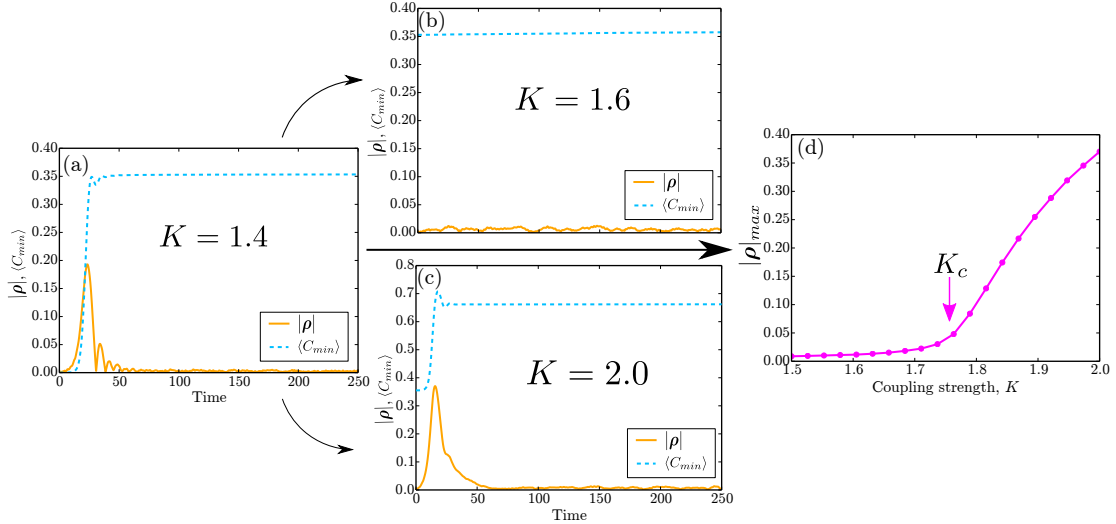


Figure 4.3: Representative plots demonstrating the short-lived macroscopic burst of coherence and the resulting IMR. (a) The magnitude of the order parameter (orange solid curve) and $\langle C_{min} \rangle$ (blue dashed curve) as a function of time for a system setup with a minimally stable distribution corresponding to $\langle C_{min} \rangle = 0$ and evolved with $K = 1.4$. Note the sharp rise and fall of $|\rho|$, i.e. the macroscopic burst of coherence, accompanied by the increase of the value of $\langle C_{min} \rangle$ (i.e., IMR). This results in an increase of the critical coupling constant for instability onset of the new incoherent distribution. Panels (b) and (c) show the order parameter evolution beginning with the distribution function at the last time-step of (a) but with K increased to $K = 1.6$ and 2.0 respectively. The presence of a macroscopic burst of $|\rho|$ in (c) and not in (b) indicates that K_c has been reset to a value between 1.6 and 2.0 . In panel (d) $|\rho|_{max}$ indicates the largest value of $|\rho|$ for systems initialized similar to (b) or (c) following a discontinuous increase of the coupling constant to a value K plotted on the horizontal axis. $|\rho|_{max}$ is macroscopically observable (i.e., distinguishable from finite- N -induced fluctuations) for bursts of $|\rho|$, and approximately 0 for incoherent steady-state distributions without any such burst. Hence (d) indicates that, by the end of the simulation in panel (a), due to IMR the critical coupling strength has been reset to $K_c \approx 1.75$. See text for more details.

$\langle C_{min} \rangle$.

To explain the origin and consequences of this short-lived macroscopic burst of $|\rho|$ we describe the evolution of the system in the space of distribution functions. Let us consider a given incoherent steady-state distribution, corresponding to a distribution F and having a corresponding critical coupling stability strength K_c for $K_c^{(-)} \leq K_c < K_c^{(+)}$ (in the numerical example presented above, F was constructed to be a minimally stable distribution with $K_c = K_c^{(-)}$). Denote a distribution of agents for a system initialized close to this incoherent steady-state distribution by $F + \delta F$, for some perturbation δF . We then examine the expected dynamics for evolution of the system under the dynamics of Eq. (4.2) for a coupling strength K abruptly increased from $K < K_c$ to $K_c < K < K_c^{(+)}$.

For almost every perturbation δF , the distribution $F + \delta F$ will no longer lie in the manifold of incoherent distributions \mathcal{M} . Since the initially chosen incoherent distribution is unstable at the increased value of K , for small t the system will rapidly evolve away from the initial distribution, $F + \delta F$, at a rate governed by Eq. (4.49), with the perturbation δF increasing as $\delta F e^{st}$, $\text{Re}(s) > 0$. This corresponds to increasing distance away from the manifold of incoherent distributions, \mathcal{M} , and hence appears as the sharp increase in $|\rho|$ described earlier (orange curve in Fig. 4.3(a)). Note, however, that for $K \leq K_c^{(+)}$ the analysis in Chapter 3 shows that there are no time-independent attractors with $|\rho| > 0$, and, further, our numerical experiments indicate that there are no $|\rho| > 0$ time-dependent attractors (e.g., periodic or chaotic). Hence the distribution function must evolve to a stable steady-state distribution function on the manifold \mathcal{M} . Thus, in the space of distribution functions, the

evolution of the system will follow a trajectory that begins near the initial incoherent steady-state distribution in \mathcal{M} , moves away from \mathcal{M} , and is then attracted back towards \mathcal{M} , but to a different incoherent steady-state distribution (corresponding to some distribution F_1) that is stable for the chosen coupling strength K . Thus, observing this system at large finite N via the order parameter demonstrates an initially small value of $|\rho|$ near zero, which rapidly rises to a large (macroscopic) value, and then falls back to a small value near zero as depicted in the representative illustration Fig. 4.3(a).

This transition from the distribution $F \in \mathcal{M}$ to the distribution $F_1 \in \mathcal{M}$ with $F_1 \neq F$ is not distinguishable solely by observation of the time-asymptotic values of ρ , since both F and F_1 correspond to incoherent steady-state distributions. However, a signature of this transition is displayed in the transient dynamics of the macroscopic observable ρ in the form of a rapid short-lived burst of $|\rho|$ away from its steady state value near zero.

4.4.2 Instability-Mediated Resetting

An important expected consequence of the above described behavior is an ‘Instability-Mediated Resetting’ of the system stability properties, which we define and describe as follows: The critical coupling constant of F_1 , denoted $K_c^{(1)}$, is necessarily greater than K . Hence, due to the evolution of the system from $F \in \mathcal{M}$ to $F_1 \in \mathcal{M}$ the critical coupling strength of the system has been reset from $K_c < K$ to $K_c^{(1)} > K$. This change in critical coupling strength without change

in the time-asymptotic macroscopic steady-state of the system (i.e., the system is on the manifold \mathcal{M} corresponding to $|\rho|=0$ at the initial distribution and at the asymptotic final distribution) is what we call *Instability-Mediated Resetting*. To demonstrate this change in critical coupling strength we choose the resulting distribution at the end of the aforementioned simulation (corresponding to time $t = 500$ in Fig. 4.3(a)) as the initial distribution for the following two situations: (i) evolution with $K = 1.6 < K_c^{(+)} \approx 2.128$, corresponding to Fig. 4.3(b), and (ii) evolution with $K = 2.0 < K_c^{(+)}$, corresponding to Fig. 4.3(c). Note that in Fig. 4.3(b) $|\rho|$ and $\langle C_{min} \rangle$ do not change significantly, whereas in Fig. 4.3(c) for $K = 2.0$ we see a characteristic short burst of $|\rho(t)|$, accompanied by a change in $\langle C_{min} \rangle$. Thus we infer that $1.6 < K_c^{(1)} < 2.0$, hence indicating this instability-mediated resetting of the critical coupling constant for instability. To more precisely pin down the value of $K_c^{(1)}$, we evolve the system for a range of values of K with each evolution having the initial condition described earlier. In Fig. 4.3(d) we plot the maximum value of $|\rho|$ attained during the evolution as a function of K . We interpret Fig. 4.3(d) as follows: For all values of $K < K_c^{(1)}$ there is no burst in $|\rho|$ and hence the maximum value is near zero; for $K > K_c^{(1)}$ the burst in $|\rho|$ results in a large value of this maximum, and this transition from zero indicates a value of $K_c^{(1)} \approx 1.75$.

We use a similar setup to verify Eq. (4.66). We consider three series of numerical simulations, corresponding to initial conditions of the minimally stable distribution (constructed with $\langle C_{min} \rangle = 0$), the uniform σ distribution (setup as described in Sec. 4.3), and the maximally stable distribution (constructed with $\langle C_{min} \rangle = 1$). For each initial condition, we evolve the system with an abrupt increase

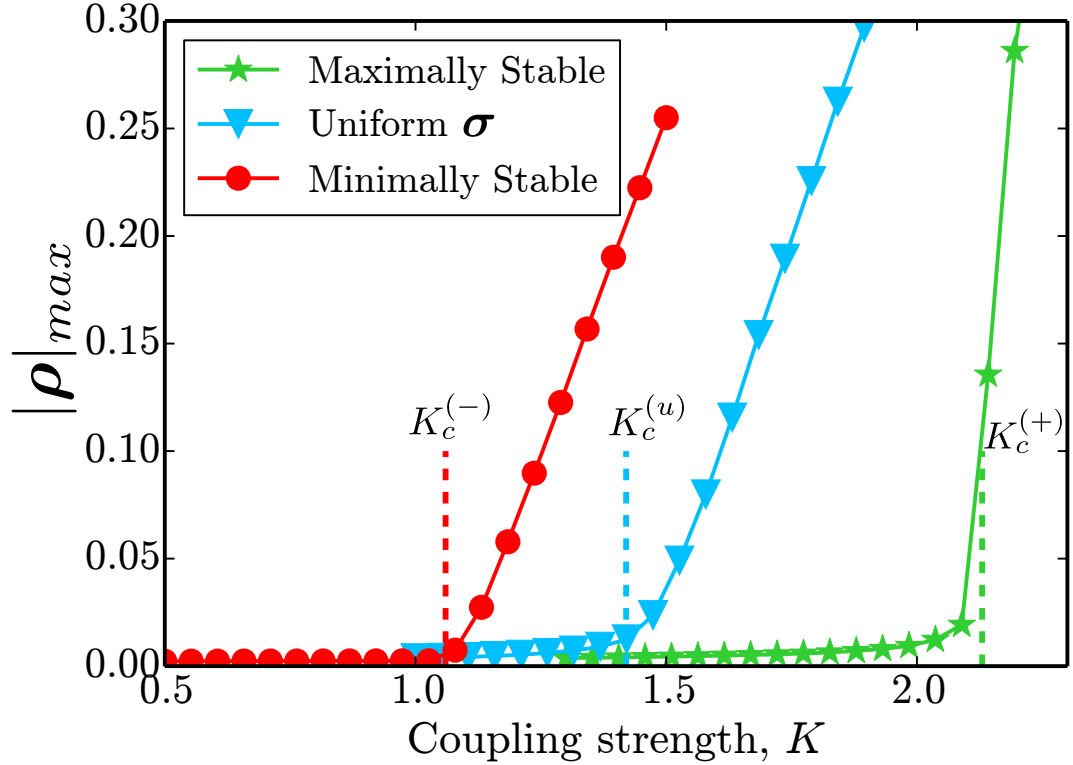


Figure 4.4: Transitions demonstrating the results derived in Eq. (4.66) for a system with $N = 10^6$. For the minimally stable distribution (red circles), the uniform σ distribution (blue triangles), and the maximally stable distribution (green stars), the system is evolved for various values of K . The maximum value attained by $|\rho(t)|$ over a short evolution is shown as a function of K . For incoherent steady-state distributions that undergo stable evolution at a given value of K , $|\rho|_{max}$ is approximately zero, whereas instability of incoherent steady-state distributions results in a short-lived burst of coherence, resulting in a larger value of $|\rho|_{max}$. The theoretical predictions for the transitions to instability are shown in the respective colors using vertical dashed lines, and agree well with the numerical results. (Note that for $K > K_c^{(+)}$, $|\rho|_{max}$ corresponds to the stable state of $|\rho| > 0$ shown in Fig. 4.1 as opposed to the peak value during these short bursts.)

from a coupling strength less than 0.5 at $t = 0$ to a given value of K and note the maximum value of $|\rho|$ attained during the evolution $t \geq 0$. This is then repeated for the same initial condition with a different value of K , over a range of values for K . The results are then plotted for this maximum attained value of $|\rho(t)|$ as a function of K . As earlier, for K below the corresponding K_c this maximum value will be approximately zero, and for K above K_c the rapid macroscopic burst of $|\rho|$ will be apparent with a larger maximum value of $|\rho|$. Thus we expect the onset of such transient bursts for the three cases at the theoretically described values $K_c^{(-)}$, $K_c^{(u)}$ and $K_c^{(+)}$, respectively, according to Eq. (4.66). These values have been marked with the vertical dashed lines in Fig. 4.4. Note the close agreement between these theoretically predicted values and the numerically observed burst onset. We expect improving agreement with increasing N . (Note that for $K > K_c^{(+)}$ the maximum attained value corresponds to the stable distribution with $|\rho| > 0$ as opposed to the rapid rise and fall described earlier.)

In each of the above cases, for a system initialized to a distribution F , with a corresponding critical instability coupling strength of K_c , we examined the case of an abrupt increase in K from a value of $K < K_c$ to a value $K > K_c$. The distribution F remains invariant to evolution for $K < K_c$, and then, after the abrupt increase, there is an initial repulsion away from the state with distribution F , followed by an attraction back towards an invariant state with distribution $F_1 \in \mathcal{M}$.

While the system state is away from \mathcal{M} and is being attracted towards F_1 , if the value of K is altered again to one greater than $K_c^{(1)}$, then the system will again be repelled away from \mathcal{M} . As the system is then attracted towards another dis-

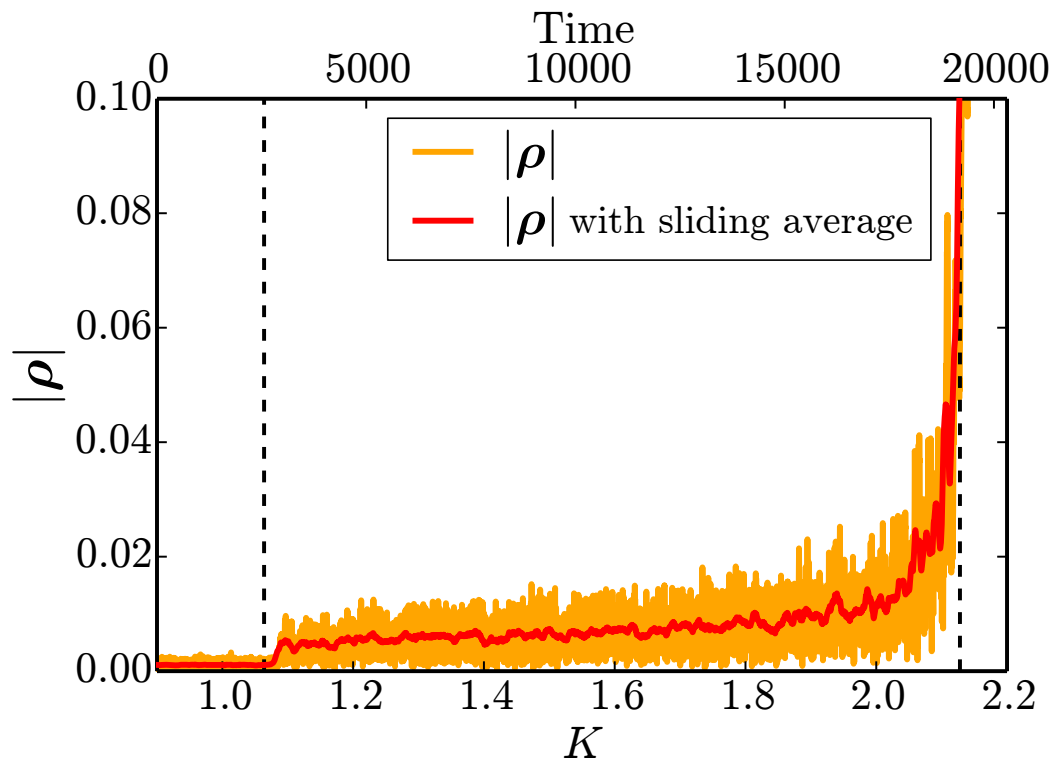


Figure 4.5: Evolution of $|\rho(t)|$ for a system having $N = 10^6$ initialized at a minimally stable incoherent steady-state distribution with slow temporally linear increase in K shown in orange, and a sliding average shown in red. The temporal increase of K is linear in time and is indicated by the horizontal axis at the top of the figure panel. The vertical dashed lines correspond to $K_c^{(-)}$ and $K_c^{(+)}$. For $K \leq K_c^{(-)}$ the initialized steady-state distribution is stable and hence $|\rho|$ maintains a value close to zero. For $K_c^{(-)} < K < K_c^{(+)}$ the system demonstrates enhanced fluctuations of $|\rho|$ about increased, nonzero values that are apparently sustained by the continuous increase of K . For $K \geq K_c^{(+)}$ no incoherent distribution is stable, and $|\rho|$ attains a larger value similar to Fig. 4.1

tinct distribution F_2 (with a critical coupling strength of $K_c^{(2)} > K_c^{(1)}$), the coupling strength can be varied again to $K > K_c^{(2)}$, resulting in additional delay in the attraction towards \mathcal{M} . In this fashion, if we consider a slowly increasing coupling strength, then we can delay this attraction towards the manifold \mathcal{M} for large amounts of time, resulting in $|\boldsymbol{\rho}(t)| > 0$ for extended periods of time without any such steady state existing at the corresponding coupling strength. This phenomenon is demonstrated in Fig 4.5, where we consider a linearly increasing coupling constant K , and plot $|\boldsymbol{\rho}|$ as a function of K and time. We observe $|\boldsymbol{\rho}|$ to show a small fluctuating increase at $K \approx K_c^{(-)}$, which is sustained until $K \approx K_c^{(+)}$, after which $|\boldsymbol{\rho}|$ approaches the steady state value of $|\boldsymbol{\rho}| > 0$ shown in Fig. 4.5. If we consider successively slower rates of increase of K , the resulting plot of $|\boldsymbol{\rho}|$ as a function of K displays smaller fluctuations from $|\boldsymbol{\rho}| = 0$ sustained through $K_c^{(-)} < K < K_c^{(+)}$. In the limit of an infinitely slow rate of increase of K , we expect that $|\boldsymbol{\rho}|$ will remain at zero for all $K < K_c^{(+)}$, reproducing Fig. 4.1.

4.4.3 Resetting due to finite size

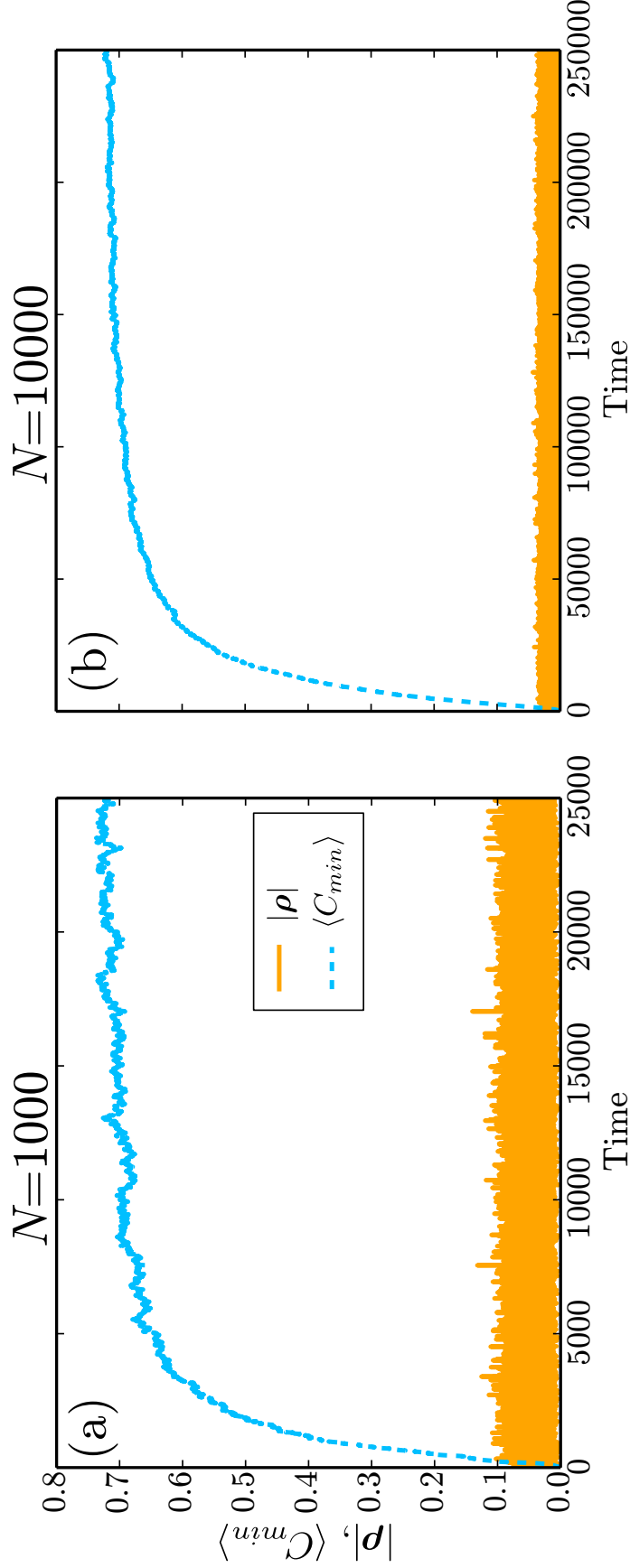


Figure 4.6: Slow finite- N -induced evolution of the incoherent steady-state distributions for (a) $N = 10^3$ and (b) $N = 10^4$. Note the significantly longer timescales shown here as compared with the Fig. 4.3. $|\rho|$ is shown as the orange curve, and $\langle C_{min} \rangle$ is shown as the blue dashed curve. Further, note the larger timescale for (b) as compared with (a). In both cases the system was initialized to a minimally stable incoherent steady-state distribution with $\langle C_{min} \rangle = 0$. $|\rho|$ remains approximately zero, indicating that the system remains in \mathcal{M} , but the gradual increase in $\langle C_{min} \rangle$ indicates the change in distribution on \mathcal{M} . The final distribution achieved after long time evolution is a maximally stable distribution.

So far we have restricted our analysis to the $N \rightarrow \infty$ limit, wherein several incoherent equilibria in the manifold \mathcal{M} can simultaneously be stable to perturbations orthogonal to \mathcal{M} and are neutrally stable to perturbations in \mathcal{M} . Hence, a small perturbation within \mathcal{M} can move an incoherent equilibrium in \mathcal{M} to another nearby incoherent equilibrium in \mathcal{M} , and many such small perturbations can cumulatively cause a large change from an initial incoherent distribution. As we have observed earlier, transient dynamics away from \mathcal{M} appear to shift the critical coupling strength for loss of stability towards $K_c^{(+)}$. Thus, we suspect that perturbations away from \mathcal{M} are biased towards maximally stable distributions. Since, in practice, N is always finite it is of interest to consider the effect of finite N . Viewing the difference between N finite but large and $N \rightarrow \infty$ as small, we can regard the system with N finite but large as being akin to the $N \rightarrow \infty$ limit system with small added perturbations. Thus we might suspect finite, large N to induce a slow secular evolution of the $N \rightarrow \infty$ incoherent equilibria towards a maximally stable distribution within \mathcal{M} . In particular, we observe that for large-but-finite N , a system initialized at any stable incoherent equilibrium undergoes slow evolution to a equilibrium corresponding to a maximally stable distribution. We demonstrate this effect in Fig. 4.6(a), where we plot $\langle C_{min} \rangle$ as a function of time for evolution of $N = 10^3$ agents initialized to the minimally stable distribution with $\langle C_{min} \rangle = 0$, evolved with $K = 0.9 < K_c^{(-)}$. Note that $\langle C_{min} \rangle$ undergoes slow growth and eventually asymptotes to a large value of $\langle C_{min} \rangle \approx 0.7$ at very long times. After this long time, the large value of $\langle C_{min} \rangle$ indicates that a large fraction of agents have moved to the subspace corresponding to the lowest frequency of rotation, similar to

our setup of the maximally stable distribution in Sec. 4.3. From this state if we consider sudden changes in K to values in the range of $K_c^{(-)} < K < K_c^{(+)}$, we do not observe any characteristic burst in the value of $|\rho|$, indicating that our distribution was indeed a maximally stable distribution.

Since this evolution towards a maximally stable distribution appears to be mediated by finite- N effects, we expect this evolution to become progressively slower as N increases, with stationarity of the incoherent distributions restored as $N \rightarrow \infty$. This picture is confirmed numerically Fig. 4.6, where it can be clearly seen that for a larger value of $N = 10^4$ initialized as earlier with $\langle C_{min} \rangle = 0$ and evolved at $K = 0.9 < K_c^{(-)}$ takes about ten times longer time to reach an asymptotic state for $\langle C_{min} \rangle$ (Note the different scales on the x-axes of the plots). Thus, for N large but finite, if one were to initialize an incoherent equilibrium distribution with $K < K_c$ (where K_c is calculated in the $N \rightarrow \infty$ limit) and wait for sufficiently long time, then one could continuously increase K without the incoherent distribution becoming unstable until K reaches $K_c^{(+)}$.

4.5 Conclusions

In this chapter we look at a D -dimensional generalization of the Kuramoto model. Unlike the case of the standard ($D = 2$) Kuramoto model, we have shown that for even $D \geq 4$ there are an infinite number of time-independent distributions of agents (defining the manifold \mathcal{M}) that correspond to the completely incoherent distribution (i.e., having $|\rho| = 0$) in the infinite system-size limit (Sec. 4.2). We

then proved that these distributions demonstrate different stabilities, with each distribution being stable for coupling strengths below a critical coupling strength K_c corresponding to the given distribution (Sec. 4.3). Further, for each value of K_c within a range $K_c^{(-)} < K_c < K_c^{(+)} = 2K_c^{(-)}$ there exists an infinite number of distributions that become unstable as K is increased through K_c . In Sec. 4.4 we show that these properties result in transitions within the $|\rho|=0$ manifold \mathcal{M} of steady-state distributions as K is increased in the range $[K_c^{(-)}, K_c^{(+)})$, which leave their signatures as short-lived macroscopic bursts in the value of $|\rho|$ (Fig. 4.3). These transitions imply a change in the microscopic state of the system, with the distribution after a transient having a significantly larger critical coupling strength for instability due to an Instability-Mediated Resetting of the distribution function (Fig. 4.3(d)). While for all $K < K_c^{(+)}$ the only stable steady-state distributions are on \mathcal{M} , we demonstrate (Fig. 4.5) that considering a linearly increasing K results in a small positive fluctuating value of $|\rho(t)|$ (and hence indicating evolution not on \mathcal{M}) which can be sustained for long periods of time as K is linearly increased through the range $K_c < K < K_c^{(+)}$ (where K_c refers to the originally initialized distribution); also, these fluctuations in $|\rho|$ become smaller as the rate of increase of K with time becomes slower. Since there are a multitude of stable distributions on \mathcal{M} , with neutral stability to perturbations in \mathcal{M} , noise can cause slow evolution of distributions in \mathcal{M} . We observe such slow evolution due to noise induced by finite- N effects (Fig. 4.6), which evolves the system towards a maximally stable distribution.

Chapter 5: Complexity Reduction Ansatz for Systems of Interacting Orientable Agents: Beyond The Kuramoto Model

The dynamics of systems with many coupled dynamical agents is a subject of increasing importance with a very broad range of applications. Much of the progress in this field has flowed from the discovery of solvable paradigmatic ‘toy’ systems. In many such systems, the agents are assumed to have one-dimensional dynamics, and a certain class of such systems has been shown to be in some sense ‘solvable’ via a novel analytic technique. In our work we consider a more general class of dynamical systems of coupled agents that may have arbitrary dimension. This is a significantly broader class of systems that contains, but is not limited to the previously described class of systems with one-dimensional agents. We then demonstrate that in this broader class of dynamical systems we can construct an analogous technique that can be used to solve such systems. Our method provides analytic techniques to allow previously inaccessible mathematical analyses of these systems. We give significant examples applying our method to large systems of interacting higher-dimensional agents, with a particular focus on the Kuramoto model generalized to higher dimensions.

5.1 Introduction

Models of systems of many coupled dynamical agents are useful tools for studying a very wide variety of phenomena [68]. Examples include flashing fireflies [5, 6], circadian rhythms of mammals [7, 8], oscillating neutrinos [14], arrays of Josephson junctions [12], oscillation of footbridges [43], biochemical oscillators [40, 85], power-grids [10, 11], collections of neurons [22, 25, 44], flocking dynamics [79–81, 86] and others. In many cases the states of the individual agents can be described by a single angle-like variable, θ . This class of model systems includes situations for which the dynamical agents are oscillators [68], neurons [22, 25, 44] or robots moving on a two-dimensional plane [79], among others. Many such models, possibly involving network-based interactions [47, 87], such as the Kuramoto model [2], the Kuramoto-Sakaguchi model [87, 88], and models of theta neurons [22] among others [19], reduce to the form

$$\dot{\theta}_i = \omega(\eta_i, \{\theta\}, t) + \frac{1}{2t} [H(\eta_i, \{\theta\}, t)e^{-i\theta_i} - H^*(\eta_i, \{\theta\}, t)e^{i\theta_i}], \quad (5.1)$$

where θ_i represents the state of the i^{th} agent, η_i is a (possibly vector) constant parameter that is associated with the i^{th} agent, $\omega(\eta_i, \{\theta\}, t)$ is its “natural frequency”, N is the total number of agents, and $H(\eta_i, \{\theta\}, t)$ is a common field that acts on each agent, dependent on the agent’s parameter η_i , and $\{\theta\}$ indicates a dependence on the set of states $\{\theta_1, \dots, \theta_N\}$ in the form of an average over i of a function of the angle θ_i .

For example, the well-studied Kuramoto model [2, 3] can be expressed in the form of Eq. (5.1) by choosing $H(\eta_i, \{\theta\}, t) = N^{-1} \sum_j \exp(i\theta_j)$, independent of η_i , and choosing $\omega(\eta_i, \{\theta\}, t)$ to independent of $\{\theta\}$ and t , allowing $\omega(\eta_i, \{\theta\}, t)$ to be replaced by ω_i . Reference [18] introduced an ansatz to analytically achieve substantial reductions in the complexity of problems of the type exemplified by Eq. (5.1) in the limit of a large number of agents ($N \rightarrow \infty$). Subsequently, this reduction has been applied in studies of a wide variety of systems (e.g., Refs. [8, 12, 22, 25, 43, 44, 52, 89]).

Several flocking models employ the Kuramoto model (e.g., Refs. [79, 80, 86]) to describe orientational alignment of the velocities of individuals in a flock. Since the standard Kuramoto model (in common with other models conforming to the general form of Eq. (5.1)) describes the dynamics of scalar angles, these models are restricted to describing flock dynamics in a two-dimensional plane. Other work has shown that the Kuramoto model can be generalized to flocks moving in three and higher-dimensional space [72, 73, 82, 90–92]. In this case each agent’s state is assumed to be specified by a unit vector $\boldsymbol{\sigma}_i(t)$ in the D -dimensional space. Alternately we may think of $\boldsymbol{\sigma}_i$ as specifying a point on the unit sphere in D -dimensional space. Reference [82] notes that the vector $\boldsymbol{\sigma}_i$ can be thought of as representing the opinion of an individual in a group, or the orientation of the velocity of a member of a flock. (For the case of flocking of birds, fish or flying drones, the generalization to $D = 3$ is of most interest.) For $D = 2$, the unit vector $\boldsymbol{\sigma}_i$ is determined by its scalar orientation angle θ_i specifying a point on the unit circle, thus recovering the previous model, Eq. (5.1) (see Sec. 5.2). References [93–96] have also studied

the Kuramoto model and its generalizations to higher dimensions in the contexts of continuous-time consensus protocols, multi-agent rendezvous, distributed control, and coalition formation. In this chapter we present a new technique that enables analytic treatment of the dynamics of a large class of systems with higher-dimensional agents, including the aforementioned systems. In particular, in this chapter we focus on the continuum limit of infinitely many higher-dimensional agents, allowing us to use ideas similar to those developed previously in the context of Eq. (5.1).

The remainder of the chapter is organized as follows: In Sec. 5.2 we construct a generalization of Eq. (5.1) to arbitrary dimensions and describe the infinite system size limit in such systems. Then, in Sec. 5.3 we extend the ansatz of Ref. [18], resulting in a simplified analytic description of this generalized class of systems. In Sec. 5.4 we demonstrate the utility of our results to example systems, with particular focus on the Kuramoto model generalized to higher dimensions. Finally, in Sec. 5.5 we conclude with a discussion and summary of our results.

5.2 Generalizing Kuramoto-like Agents to Higher Dimensions

In Chapters 3 and 4, we constructed a generalization of the Kuramoto model to D dimensions. Here we consider an even more general setup, where we consider a generalization to Eq. (5.1) to a system in D dimensions,

$$\dot{\sigma}_i = [\rho(\eta_i, \{\sigma\}, t) - (\sigma_i \cdot \rho(\eta_i, \{\sigma\}, t))\sigma_i] + \mathbf{W}(\eta_i, \{\sigma\}, t)\sigma_i, \quad (5.2)$$

where for each i , $\boldsymbol{\sigma}_i(t)$ is a real D -dimensional unit vector, $|\boldsymbol{\sigma}_i(0)|=1$, $\boldsymbol{\rho}(\eta_i, \{\boldsymbol{\sigma}\}, t)$ is an arbitrary real D -dimensional vector, which can be thought of as a common field that affects each agent in an η_i dependent fashion, $\mathbf{W}(\eta_i, \{\boldsymbol{\sigma}\}, t)$ is a real $D \times D$ antisymmetric matrix, η_i is a (possibly vector) constant parameter associated with each agent, and, as earlier, $\{\boldsymbol{\sigma}\}$ indicates a dependence on the set of all states $\{\boldsymbol{\sigma}_1, \dots, \boldsymbol{\sigma}_N\}$ in the form of the average over i of a function of the unit vectors $\boldsymbol{\sigma}_i$ (we further quantify this dependence on $\{\boldsymbol{\sigma}\}$ later). For example, in the context of flocking agents in D dimensions, $\boldsymbol{\sigma}_i$ represents the orientation of the i^{th} agent, $\boldsymbol{\rho}(\eta_i, \{\boldsymbol{\sigma}\}, t)$ represents a ‘goal’ orientation to which the i^{th} agent attempts to align itself, and $\mathbf{W}(\eta_i, \{\boldsymbol{\sigma}\}, t)$ represents a fixed bias, or a systematic error to the agent dynamics causing the agent to head in a direction that deviates from the direction of $\boldsymbol{\rho}$. Note from the form of Eq. (5.2) that the dot product of the right-hand side of Eq. (5.2) with $\boldsymbol{\sigma}_i$ is identically zero, so that $d|\boldsymbol{\sigma}|/dt = 0$, as required by our identification of $\boldsymbol{\sigma}$ as a unit vector. Thus the dynamics of each $\boldsymbol{\sigma}_i$ is restricted to the $(D - 1)$ -dimensional surface, \mathcal{S} , of the unit sphere, $|\boldsymbol{\sigma}|=1$. For $D = 2$, choosing $\boldsymbol{\sigma}_i = (\cos \theta_i, \sin \theta_i)^T$, $\boldsymbol{\rho}(\eta_i, \{\boldsymbol{\sigma}\}, t) = (\text{Re}[H(\eta_i, \{\theta\}, t)], \text{Im}[H(\eta_i, \{\theta\}, t)])^T$ and

$$\mathbf{W}(\eta_i, \{\boldsymbol{\sigma}\}, t) = \begin{pmatrix} 0 & \omega(\eta_i, \{\theta\}, t) \\ -\omega(\eta_i, \{\theta\}, t) & 0 \end{pmatrix},$$

reduces Eq. (5.2) to Eq. (5.1), thus justifying Eq. (5.2) as a D -dimensional generalization of Eq. (5.1).

We now consider the limit of a large number of agents, and denote by $F(\boldsymbol{\sigma}, \eta, t)$

the distribution of agents on \mathcal{S} , such that $F(\boldsymbol{\sigma}, \eta, t)d^{D-1}\sigma d\eta$ is the fraction of agents that lie in the $(D - 1)$ -dimensional differential element $d^{D-1}\sigma$ on the surface \mathcal{S} centered at $\boldsymbol{\sigma}$ at time t , and have an associated parameter η within the differential element $d\eta$ centered at η . Since the associated parameter η for each agent is time independent, we define

$$g(\eta) = \int_{\mathcal{S}} F(\boldsymbol{\sigma}, \eta, t)d^{D-1}\sigma,$$

and

$$f(\boldsymbol{\sigma}, \eta, t) = F(\boldsymbol{\sigma}, \eta, t)/g(\eta).$$

Noting that Eq. (5.2) specifies the vector field of the flow controlling the dynamics of the distribution f , we write a continuity equation for f ,

$$\partial f(\boldsymbol{\sigma}, \eta, t)/\partial t + \nabla_{\mathcal{S}} \cdot [f(\boldsymbol{\sigma}, \eta, t)\mathbf{v}(\boldsymbol{\sigma}, \eta, t)] = 0, \quad (5.3)$$

where the velocity field $\mathbf{v}(\boldsymbol{\sigma}, \eta, t)$ is given by $\mathbf{v}(\boldsymbol{\sigma}, \eta, t) = (\boldsymbol{\rho}(\eta, t) - (\boldsymbol{\sigma} \cdot \boldsymbol{\rho}(\eta, t))\boldsymbol{\sigma}) + \mathbf{W}(\eta, t)\boldsymbol{\sigma}$, and $\nabla_{\mathcal{S}} \cdot \mathbf{A}$ represents the divergence of a vector field \mathbf{A} , along the surface \mathcal{S} . This can be done if the dependence of $\boldsymbol{\rho}$ and \mathbf{W} on $\{\boldsymbol{\sigma}\}$ can be specified as a functional of $F(\boldsymbol{\sigma}, \eta, t)$ that is not explicitly dependent on $\boldsymbol{\sigma}$. (A simple example of such a dependence on $\{\boldsymbol{\sigma}\}$ would be the average value of $p(\boldsymbol{\sigma}_i)$ for some given function p , which can be written as $\int \int p(\boldsymbol{\sigma})F(\boldsymbol{\sigma}, \eta, t)d\boldsymbol{\sigma}d\eta$.) Following Appendix A, Eq. (5.3) can be rewritten as

$$\begin{aligned} \partial f/\partial t + [\nabla_{\mathcal{S}} f(\boldsymbol{\sigma}, \eta, t) - (D - 1)f(\boldsymbol{\sigma}, \eta, t)\boldsymbol{\sigma}] \cdot \boldsymbol{\rho}(\eta, t) \\ + (\mathbf{W}(\eta, t)\boldsymbol{\sigma}) \cdot \nabla_{\mathcal{S}} f(\boldsymbol{\sigma}, \eta, t) = 0, \end{aligned} \quad (5.4)$$

where $\nabla_{\mathcal{S}}\Phi$ is the gradient of a scalar field Φ projected on the surface \mathcal{S} .

5.3 Analytic Solution in the Limit of Large Systems

For $D = 2$, Refs. [18, 19] demonstrated that the ansatz that $f(\theta, t)$ is in the form

$$f(\theta, \eta, t) = \frac{1}{2\pi} \frac{1 - |\alpha(\eta, t)|^2}{|e^{i\theta} - \alpha(\eta, t)|^2}, \quad (5.5)$$

where $\alpha(\eta, t)$ is a complex scalar function of η and t , $|\alpha(\eta, 0)| < 1$, reduces Eq. (5.1) to the following θ -independent form

$$\frac{\partial \alpha}{\partial t} + i\eta + \frac{1}{2} (H^*(\eta, t)\alpha^2(\eta, t) - H(\eta, t)) = 0. \quad (5.6)$$

The form Eq. (5.5) represents an invariant manifold in the space of possible distributions f , that satisfy the continuity equation Eq. (5.3) for $D = 2$. Furthermore, previous work [19, 20] has shown that initial conditions for f are attracted to the invariant manifold Eq. (5.5) for a large class of possible models of the form Eq. (5.1). Thus Eq. (5.5) can be used to greatly simplify the study of the long-term dynamics of these systems.

Here we present an ansatz demonstrating the existence of a similar invariant manifold for Eq. (5.3) in any dimension D . Noting that $e^{i\theta}$ can be interpreted as a unit vector in the complex plane and that the complex quantity α can similarly be interpreted as a two-dimensional vector of its real and imaginary parts, based on Eq. (5.5) we posit the following guess for the form of $f(\boldsymbol{\sigma}, \eta, t)$ for arbitrary dimension

D ,

$$f(\boldsymbol{\sigma}, \eta, t) = \frac{N_D(\boldsymbol{\alpha}(\eta, t))}{|\boldsymbol{\sigma} - \boldsymbol{\alpha}(\eta, t)|^{\beta_D}}, \quad (5.7)$$

where $\boldsymbol{\alpha}$ is a real D -dimensional vector such that $|\boldsymbol{\alpha}(\eta, 0)| < 1$, β_D is a yet-to-be-determined constant, and $N_D(\boldsymbol{\alpha})$ is a scalar normalization chosen to ensure that

$$\int_{\mathcal{S}} f(\boldsymbol{\sigma}, \eta, t) d^{D-1}\sigma = 1. \quad (5.8)$$

Inserting Eq. (5.7) into the continuity equation in Eq. (5.4), we obtain after some algebra,

$$\begin{aligned} & (1 + |\boldsymbol{\alpha}|^2 - 2\boldsymbol{\alpha} \cdot \boldsymbol{\sigma}) \partial_t N_D(\boldsymbol{\alpha}) - \beta_D N_D(\boldsymbol{\alpha}) (\boldsymbol{\alpha} \cdot \partial_t \boldsymbol{\alpha} - \boldsymbol{\sigma} \cdot \partial_t \boldsymbol{\alpha}) \\ & + N_D(\boldsymbol{\alpha}) \{ \beta_D (\boldsymbol{\alpha} \cdot \boldsymbol{\rho}) + [2(D-1) - \beta_D] (\boldsymbol{\alpha} \cdot \boldsymbol{\sigma}) (\boldsymbol{\rho} \cdot \boldsymbol{\sigma}) \\ & - (D-1) (\boldsymbol{\rho} \cdot \boldsymbol{\sigma}) (1 + |\boldsymbol{\alpha}|^2) - \beta_D \boldsymbol{\sigma} \cdot \mathbf{W} \boldsymbol{\alpha} \} = 0. \end{aligned} \quad (5.9)$$

For our ansatz Eq. (5.7) to apply, the above equation must hold for all $\boldsymbol{\sigma}$. Focusing on the term in Eq. (5.9) that is quadratic in $\boldsymbol{\sigma}$, i.e., $N_D(\boldsymbol{\alpha}) [2(D-1) - \beta_D] (\boldsymbol{\alpha} \cdot \boldsymbol{\sigma}) (\boldsymbol{\rho} \cdot \boldsymbol{\sigma})$, since in general $\boldsymbol{\alpha}$ and $\boldsymbol{\rho}$ will not be zero for all t , we require that

$$\beta_D = 2(D-1). \quad (5.10)$$

With β_D in Eq.(5.7) determined, we now obtain the normalization constant $N_D(\boldsymbol{\alpha})$. To perform the integral in Eq. (5.8), without loss of generality we take the vector $\boldsymbol{\alpha}$ to be along the \hat{z} axis. For an arbitrary point $\boldsymbol{\sigma}$ on \mathcal{S} , we denote the angle between $\boldsymbol{\sigma}$ and \hat{z} by θ . In particular, we note that the distance of the point $\boldsymbol{\sigma}$ from the \hat{z} axis is $\sin \theta$. For a coordinate system on the surface \mathcal{S} , we

use θ as one of the coordinates, denoting position with respect to \hat{z} on the sphere. From the symmetry of f in Eq.(5.7) about the direction $\boldsymbol{\alpha}$, we see that the integrals over these remaining coordinates give the surface area $S_{D-1} \sin^{D-2} \theta$ of the $(D-2)$ dimensional surface of a sphere with radius $\sin \theta$ embedded in $(D-1)$ dimensions, where $S_{D-1} = (2\pi)^{(D-1)/2} / \Gamma((D-1)/2)$ is the area of the sphere of unit radius in $D-1$ dimensional space. Thus Eq. (5.8) becomes

$$1 = S_{D-1} \int_0^\pi \frac{N_D(\boldsymbol{\alpha}) \sin^{D-2} \theta d\theta}{(1 + |\boldsymbol{\alpha}|^2 - 2|\boldsymbol{\alpha}| \cos \theta)^{D-1}}, \quad (5.11)$$

which can be evaluated to give

$$1 = K_D^{-1} \frac{N_D(\boldsymbol{\alpha})}{(1 - |\boldsymbol{\alpha}|^2)^{D-1}}, \quad (5.12)$$

where K_D is a constant dependent only on D . This results in

$$N_D(\boldsymbol{\alpha}) = K_D (1 - |\boldsymbol{\alpha}|^2)^{D-1}, \quad (5.13)$$

giving the form of the ansatz for arbitrary dimensions as

$$f(\boldsymbol{\sigma}, \eta, t) = K_D \frac{(1 - |\boldsymbol{\alpha}(\eta, t)|^2)^{D-1}}{|\boldsymbol{\sigma} - \boldsymbol{\alpha}(\eta, t)|^{2(D-1)}}, \quad (5.14)$$

which, for $D = 2$, agrees with Eq. (5.5).

To determine whether the ansatz Eq. (5.14), is consistent with Eq. (5.9) we insert it into Eq. (5.9). We find that the ansatz with β_D given by Eq. (5.10) indeed

is a solution of Eq. (5.9) and that Eq. (5.9) reduces to the following equation for $\boldsymbol{\alpha}$ (see Appendix B.1 for details),

$$\partial_t \boldsymbol{\alpha} = \frac{1}{2}(1 + |\boldsymbol{\alpha}|^2)\boldsymbol{\rho} - (\boldsymbol{\rho} \cdot \boldsymbol{\alpha})\boldsymbol{\alpha} + \mathbf{W}\boldsymbol{\alpha}. \quad (5.15)$$

The key point is that Eq. (5.15) does not involve $\boldsymbol{\sigma}$ (and remarkably, also does not involve any dependence on D). Thus, analogously to Eq. (5.6), we have a $\boldsymbol{\sigma}$ -independent description of the dynamics of $\boldsymbol{\alpha}$. This is our main result.

We note that for initial conditions with $|\boldsymbol{\alpha}| < 1$, $|\boldsymbol{\alpha}|$ will remain less than 1 at all finite times since from Eq. (5.15) $\partial_t |\boldsymbol{\alpha}| = 0$ at $|\boldsymbol{\alpha}| = 1$, thus verifying that f given by Eq. (5.14) does not diverge for $t < \infty$.

5.4 Example Systems

We now consider a few examples illustrating the utility of the generalized ansatz, Eq. (5.14), to systems of the form given in Eq. (5.2). We detail the particular example of the Kuramoto model generalized to D dimensions (introduced in Chapter 3) as representative of the utility of our main result Eq. (5.15), and thereafter briefly mention applications of this result to a variety of other systems.

5.4.1 The Kuramoto Model Generalized to Higher Dimensions

A generalization of the Kuramoto model with homogenous oscillators to arbitrary dimension was introduced by Olfati-Saber in 2006 [82] in the context of flocking dynamics, consensus protocols, and opinion dynamics. We generalized this to het-

erogeneous systems in Chapter 3. For generalization to D dimensions, a system order parameter, \mathbf{z} , can be defined as

$$\mathbf{z}(t) = \frac{1}{N} \sum_i \boldsymbol{\sigma}_i(t). \quad (5.16)$$

The magnitude of $\mathbf{z}(t)$ is a measure of the coherence of the set of agents $\{\boldsymbol{\sigma}\}$. The common field $\boldsymbol{\rho}$ is then defined as the η_i -independent function,

$$\boldsymbol{\rho}(\eta, \{\boldsymbol{\sigma}\}, t) = K\mathbf{z}(t) = (K/N) \sum_i \boldsymbol{\sigma}_i(t), \quad (5.17)$$

where K is a coupling constant. By interpreting the vector parameters η_i in $\mathbf{W}(\eta_i, \{\boldsymbol{\sigma}\}, t)$ as the $D(D-1)/2$ independent elements of a D -dimensional antisymmetric matrix \mathbf{W}_i , we can replace $g(\eta)d\eta$ in integrals by $G(\mathbf{W})d\mathbf{W}$ where $G(\mathbf{W})$ is a distribution of antisymmetric matrices. In cases such as these where $\mathbf{W}(\eta_i, \{\boldsymbol{\sigma}\}, t)$ is independent of $\{\boldsymbol{\sigma}\}$ and t , we interpret $\mathbf{W}(\eta_i) = \mathbf{W}_i$ as the “natural rotation” of $\boldsymbol{\sigma}_i$.

In the limit of infinite system size, with a distribution of agents given according to Eq. (5.14),

$$\begin{aligned} \mathbf{z}(t) &= \int_{\mathcal{S}} F(\boldsymbol{\sigma}, \mathbf{W}, t) \boldsymbol{\sigma} d^{D-1} \boldsymbol{\sigma} d\mathbf{W}, \\ &= \int d\mathbf{W} G(\mathbf{W}) \boldsymbol{\alpha}(\mathbf{W}, t) / |\boldsymbol{\alpha}(\mathbf{W}, t)| \\ &\quad \times \int_0^\pi \frac{K_D (1 - |\boldsymbol{\alpha}(\mathbf{W}, t)|^2)^{D-1} \cos \theta \sin^{D-2} \theta d\theta}{(1 + |\boldsymbol{\alpha}(\mathbf{W}, t)|^2 - 2|\boldsymbol{\alpha}(\mathbf{W}, t)| \cos \theta)^{D-1}} \end{aligned} \quad (5.18)$$

For $D = 2$ (i.e, the original Kuramoto model) Eq. (5.18) evaluates to give $\boldsymbol{\rho}(t) = K\mathbf{z}(t) = K \int d\omega g(\omega) \boldsymbol{\alpha}(\omega, t)$. Equation (5.15) is then equivalent to Eq. (6)

from Ref. [18]. For $D = 3$, the integral in Eq. (5.18) gives

$$\begin{aligned} \boldsymbol{\rho} = K \int d\mathbf{W} G(\mathbf{W}) \boldsymbol{\alpha}(\mathbf{W}, t) / |\boldsymbol{\alpha}(\mathbf{W}, t)| \\ \times \left[2|\boldsymbol{\alpha}|(1 + |\boldsymbol{\alpha}|^2) + (1 - |\boldsymbol{\alpha}|^2)^2 \log \left(\frac{1 - |\boldsymbol{\alpha}|}{1 + |\boldsymbol{\alpha}|} \right) \right] / 4|\boldsymbol{\alpha}|^2. \end{aligned} \quad (5.19)$$

This now allows us to use Eq. (5.15) with some given $G(\mathbf{W})$ to numerically integrate for the dynamics of $\boldsymbol{\alpha}$, and the dynamics of the order parameter $\boldsymbol{\rho}$.

Using this simplification, we can efficiently simulate the dynamics of the full system of agents governed by Eq. (5.2). We first focus on the case of homogenous agents, i.e., identical natural rotations for each agent, $G(\mathbf{W}) = \delta(\mathbf{W} - \mathbf{W}_0)$, where $\delta(\cdot)$ is the Dirac-delta function. We can then change to a rotating basis in which the natural rotation term of each agent is zero, $\mathbf{W}_0 \rightarrow 0$. This makes the \mathbf{W} -integral in Eq. (5.18) trivial, allowing a direct representation of $\boldsymbol{\rho}$ in terms of $\boldsymbol{\alpha}$. Further, $\boldsymbol{\alpha}$ is only dependent on time (rather than \mathbf{W} and t). This represents a very large simplification in the complexity of the dynamics of the system of agents, since Eq. (5.15) is now a single D -dimensional ordinary differential equation which represents the collective dynamics of the $N \rightarrow \infty$, D -dimensional system of coupled differential equations in Eq. (5.2). The utility of this result is demonstrated for $D = 3$ in Fig. 5.1(a), where we show (plotted in black) the time-series for $|\boldsymbol{\rho}(t)|$ as generated from a system of $N = 5000$ agents (approximating the $N \rightarrow \infty$ limit), compared with the time-series generated from the theory derived in Eq. (5.15) (orange dashed curve). The initial condition for the full system was chosen such that the agents were uniformly randomly distributed on the sphere. For the theory derived in Eq. (5.15), i.e., the reduced equations, the initial value of $\boldsymbol{\alpha}$ was chosen to

have magnitude 0.01 in an arbitrary direction. Note the remarkably close agreement between the black and the orange dashed curve, demonstrating that the dynamics on the reduced manifold of Eq. (5.14) indeed gives the large- N dynamics of the full system of interacting agents.

For the case of heterogeneous agents, α in Eq. (5.18) depends on \mathbf{W} , and we perform the integral in a Monte-Carlo fashion. We randomly choose $N_{\mathbf{W}}$ values of \mathbf{W} from the given distribution $G(\mathbf{W})$ and simulate the dynamics of the corresponding $\alpha(\mathbf{W})$ s. These randomly chosen $\alpha(\mathbf{W})$ s are then used as the Monte-Carlo samples to evaluate \mathbf{z} according to Eq. (5.18), simulating the dynamics of the system in the $N \rightarrow \infty$ limit by only simulating the dynamics of $N_{\mathbf{W}}$ variables. Here we choose an isotropic distribution $G(\mathbf{W})$ constructed by choosing each upper triangular element from identical independent normal distributions with zero mean and unit variance, and choosing the remaining elements to make \mathbf{W} antisymmetric. Results are shown in Fig. 5.1(b) for $D = 3$, where $N_{\mathbf{W}} = 500$ Monte-Carlo samples were chosen to evaluate the $|\rho(t)|$ curve via the theory in Eq. (5.15), and are compared with the curve obtained for simulating the dynamics of the full system of equations in the $N \rightarrow \infty$ limit, approximated by a simulation of $N = 5000$ agents. Note how simulating the dynamics of $N_{\mathbf{W}} \ll N$ Monte-Carlo samples yields a smooth curve approximating the noisy curve generated by simulating the individual dynamics of $N = 5000$ agents. Initial conditions for the full system were chosen as a bimodal distribution of σ_i s, independent of the corresponding \mathbf{W}_i , with the two peaks being anti-podal to each other, hence representing a distribution explicitly not on the manifold dictated by Eq. (5.14). The initial condition for the reduced equations,

i.e., Eq. (5.15) were chosen to be uniform on a sphere of radius 0.01, corresponding to an approximately uniform distribution of $f(\boldsymbol{\sigma}, \eta, t)$ in $\boldsymbol{\sigma}$. Despite not lying on the invariant manifold described by Eq. (5.14), we observe that the dynamics of the full system rapidly approach the dynamics as predicted by Eq. (5.15) for the $N \rightarrow \infty$ limit for dynamics on the invariant manifold. This indicates that for the case of heterogeneous agents the invariant manifold Eq. (5.14) is attracting, as has been proven for the case of $D = 2$ [19]. Full system simulations with initial conditions described by a uniform distribution in $\boldsymbol{\sigma}$ (and hence lying on the invariant manifold Eq. (5.14) for $|\boldsymbol{\alpha}| = 0$) yielded a curve that is not discernibly different from the curve presented in Fig. 5.1(b).

5.4.2 Applications of Eq. (5.15) to previous results on the Generalized Kuramoto model

As demonstrated in Fig. 5.1, numerical integration of the dynamics on the invariant manifold, via Eq. (5.15) closely reproduces the time evolution of the order parameter of the Kuramoto model generalized to higher dimensions (Eq. (5.2) for $\boldsymbol{\rho}$ according to Eq. (5.19)). As we demonstrate in Fig. 5.2, this close similarity between a simulation of the full N -agent dynamics and the simulation of the reduced equation Eq. (5.15) holds at all values of the coupling constant K . This allows us to recreate the discontinuous phase transition of the Kuramoto model generalized to 3 dimensions reported in Chapter 3 (The continuous phase transition observed through reduced equations of the form Eq. (5.15) for the standard Kuramoto model

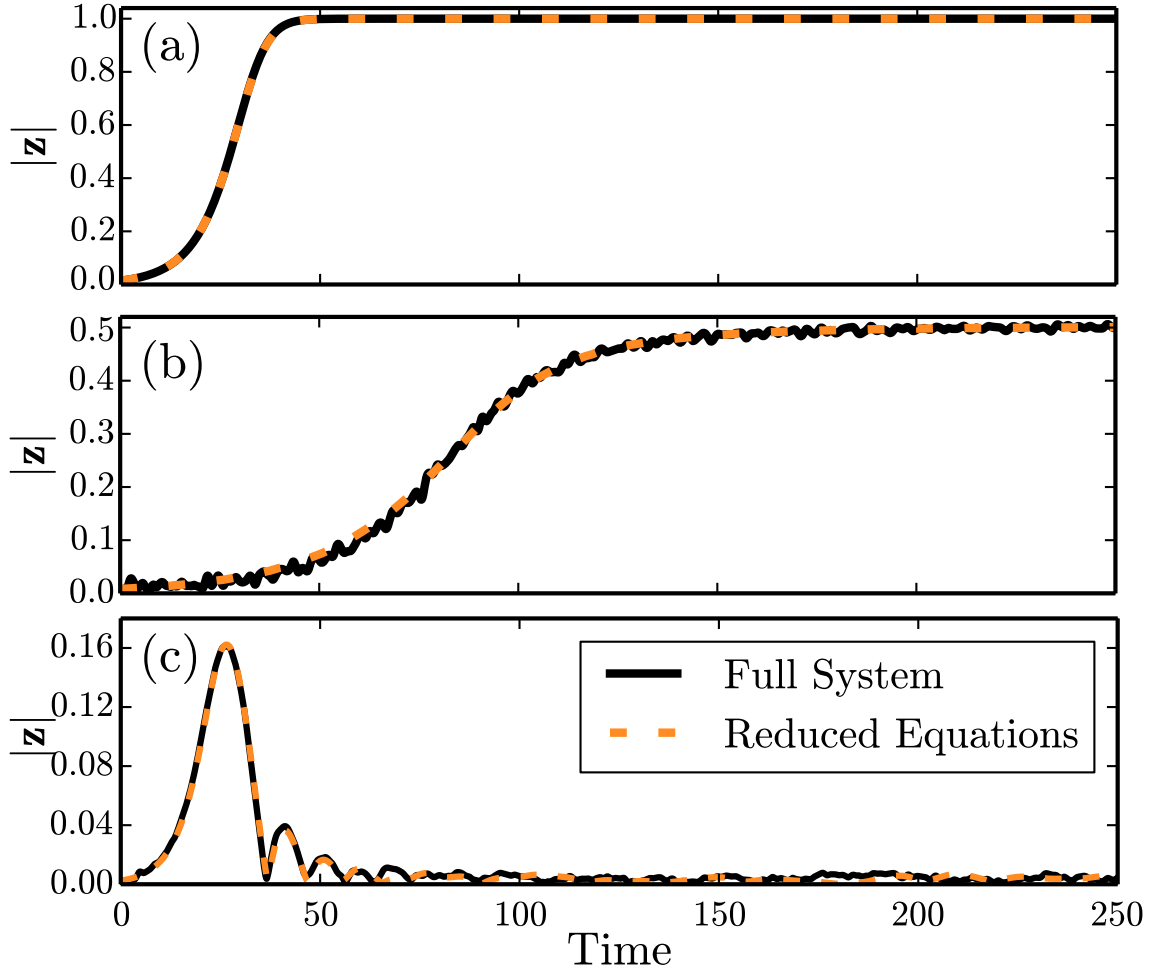


Figure 5.1: (a),(b): Comparison between the dynamics of the magnitude of the order parameter, $|z|$, as a function of time via full system modeling of the generalized Kuramoto model with $D = 3$ (Eq. (5.2) for ρ given by Eq. (5.19)) using $N = 5000$ agents shown in black, with the modeling of the reduced differential equation Eq.(5.15) plotted as the orange dashed line. $K = 2$ for both figures. (a) is the case of homogenous agents, i.e., $G(\mathbf{W}) = \delta(\mathbf{W} - \mathbf{W}_0)$. (b) is the case of heterogeneous agents, where the distribution $G(\mathbf{W})$ is nonsingular and chosen as described in the main text. Only $N_{\mathbf{W}} = 500$ Monte-Carlo samples were required to produce the curve for the reduced system of equations, representing the $N \rightarrow \infty$ limit of the full system, approximated by the noisy curve generated using $N = 5000$ agents for the full system. (c) demonstrates similar agreement for the case of heterogeneous agents in $D = 4$, where the system is evolved at $K = 1.7$ from the uniform incoherent distribution as the initial condition. $N = N_{\mathbf{W}} = 10^6$ was used for numerical integration of the two curves. Note how the reduced equations capture the transient behavior of the Instability-Mediated Resetting phenomenon (introduced in Chapter 4). Since the initial finite-size noise is different in the two cases, in order to make the curves for the full system and the reduced equations lie on each other, we shift them in time to align them. See text for further details of initial conditions used.

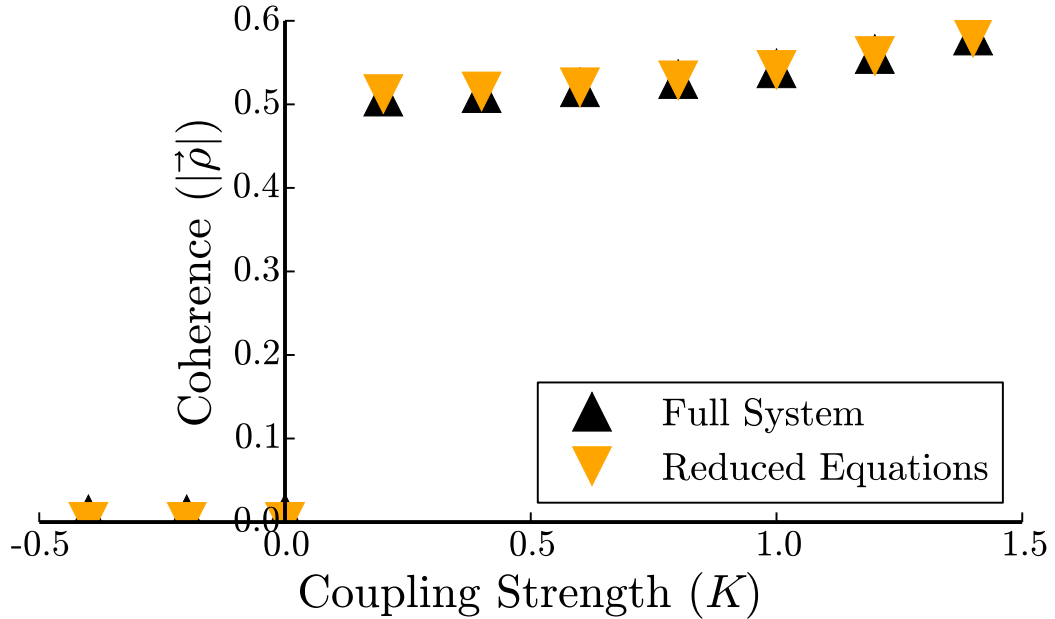


Figure 5.2: A simulation of the phase transition to coherence via numerical integration of Eq. (5.2) for ρ given by Eq. (5.19) representing the full system dynamics with $N = 5000$ (shown in the black triangular markers), and via numerical integration of Eq. (5.15) representing the dynamics on the invariant manifold with $N_{\mathbf{W}} = 500$ (shown as the orange inverted triangles) for $D = 3$. For each value of K , the system is evolved until $|\rho|$ reaches an equilibrium. Note the close agreement between the time asymptotic values of $|\rho|$ at all values of K . The distribution $G(\mathbf{W})$ was chosen as described earlier for heterogeneous agents.

in two dimensions has been demonstrated and discussed in Ref. [18]).

Chapter 4 demonstrated that the Kuramoto model generalized to even dimensions $D \geq 4$ exhibits the unusual behavior of Instability-Mediated Resetting: If the coupling strength K is increased abruptly while remaining below the critical coupling strength for the onset to coherence, the Kuramoto model displays a short burst of coherence (see Ref. Chapter 4 for further details). This is illustrated by the results shown in Fig. 5.1(c). In Fig. 5.1(c) the initial conditions for the σ_i in the full system simulation were chosen independently to be uniformly random over

the sphere $|\boldsymbol{\sigma}|=1$. For the reduced equations, initial conditions for $\boldsymbol{\alpha}$ were chosen similar to the earlier discussion on heterogeneous agents, i.e., uniform on a sphere of radius 0.01, corresponding to an approximately uniform distribution of $f(\boldsymbol{\sigma}, \eta, t)$ in $\boldsymbol{\sigma}$. Figure 5.1(c) demonstrates that the dynamics of Eq. (5.15), representing the dynamics on the invariant manifold described by Eq. (5.14) (shown in the dashed orange curve), accurately captures these short bursts of coherence, further demonstrating the capability of Eq. (5.15) in capturing the transient dynamics of the Kuramoto model generalized to higher dimensions.

To demonstrate the applicability of Eq. (5.15) in improving theoretical understanding of such systems, we present an example of a stability analysis of the Kuramoto model generalized to three dimensions via a study of the dynamics on the reduced manifold Eq. (5.14). In particular, we study the stability of the completely incoherent state for a system of heterogeneous agents, wherein the initial condition of each agent $\boldsymbol{\sigma}_i$ is to be distributed independently and uniformly over the sphere $|\boldsymbol{\sigma}|=1$. In the $N \rightarrow \infty$ limit this is the distribution $F(\boldsymbol{\sigma}, \eta, t) = g(\eta)/(4\pi)$ corresponding to setting $|\boldsymbol{\alpha}|=0$ in Eq. (5.14). [In the context of the stability analysis presented in Sec. 3.3.2 of Chapter 3, we are considering the case of $p=0$]. Thus we are interested in the stability analysis of Eq. (5.15) about $|\boldsymbol{\alpha}|=0$. Performing a first order expansion of Eq. (5.15) for $|\boldsymbol{\alpha}|\ll 1$,

$$\partial\boldsymbol{\alpha}(\mathbf{W}, t)/\partial t = \boldsymbol{\rho}(t)/2 + \mathbf{W}\boldsymbol{\alpha}(\mathbf{W}, t). \quad (5.20)$$

Assuming $\boldsymbol{\alpha}(\mathbf{W}, t) = \boldsymbol{\alpha}(\mathbf{W})e^{st}$, we obtain

$$\boldsymbol{\alpha}(\mathbf{W}) = \frac{1}{2}(s\mathbf{1} - \mathbf{W})^{-1}\boldsymbol{\rho}. \quad (5.21)$$

Note that in the limit of $|\boldsymbol{\alpha}| \ll 1$, Eq. (5.19) can be written as

$$\boldsymbol{\rho} = \left(\frac{4K}{3}\right) \int d\mathbf{W} G(\mathbf{W}) \boldsymbol{\alpha}(\mathbf{W}). \quad (5.22)$$

Multiplying Eq. (5.21) by $(4/3)G(\mathbf{W})$ and integrating, we obtain

$$\boldsymbol{\rho} = \frac{2K}{3} \int (s\mathbf{1} - \mathbf{W})^{-1} \boldsymbol{\rho} d\mathbf{W}. \quad (5.23)$$

Note that in three dimensions the linear transformation $\mathbf{W}\boldsymbol{\sigma}$ can be represented as the cross product $\boldsymbol{\omega} \times \boldsymbol{\sigma}$. Without loss of generality we may choose a basis that block-diagonalizes \mathbf{W} , corresponding to the choice of $\boldsymbol{\omega} = \omega\hat{z}$ and

$$\mathbf{W} = \omega \begin{pmatrix} 0 & -1 & 0 \\ 1 & 0 & 0 \\ 0 & 0 & 0 \end{pmatrix}.$$

Thus,

$$(s\mathbf{1} - \mathbf{W})^{-1} = \begin{pmatrix} \frac{s}{s^2 + \omega^2} & \frac{\omega}{s^2 + \omega^2} & 0 \\ \frac{-\omega}{s^2 + \omega^2} & \frac{s}{s^2 + \omega^2} & 0 \\ 0 & 0 & \frac{1}{s} \end{pmatrix}.$$

This can now be inserted into Eq. (5.23), and written in a basis independent format

as

$$\boldsymbol{\rho} = \int G(\boldsymbol{\omega}) \frac{2K}{3} \left(\frac{(\boldsymbol{\rho} \cdot \hat{\boldsymbol{\omega}})\hat{\boldsymbol{\omega}}}{s} + \frac{\boldsymbol{\omega} \times \boldsymbol{\rho}}{s^2 + \omega^2} + \frac{s}{s^2 + \omega^2} (\boldsymbol{\rho} - (\boldsymbol{\rho} \cdot \hat{\boldsymbol{\omega}})\hat{\boldsymbol{\omega}}) \right) d\boldsymbol{\omega}. \quad (5.24)$$

We choose the distribution $G(\boldsymbol{\omega})$ to be an *isotropic* distribution (i.e., a distribution that is invariant to orthogonal transformations) which can hence be written as $G(\boldsymbol{\omega})d\boldsymbol{\omega} = g(\omega)U(\hat{\boldsymbol{\omega}})d\omega d\hat{\boldsymbol{\omega}}$, where $U(\hat{\boldsymbol{\omega}}) = 1/(4\pi)$ represents the isotropic distribution of rotation directions, and $g(\omega)$ is the distribution of the magnitudes of rotation (see Chapter 3 for further discussion on the choice of this distribution and its implications). Integrating over the rotation directions $\hat{\boldsymbol{\omega}}$ in Eq. (5.24) gives us

$$1 = \frac{2K}{3} \left(\frac{1}{3s} + \frac{2s}{3} \int \frac{g(\omega)d\omega}{s^2 + \omega^2} \right), \quad (5.25)$$

which is identical to the result obtained in Chapter 3. As discussed in Chapter 3, the above equation implies that in the limit of small K ,

$$s = 2K/9, \quad (5.26)$$

indicating that this completely incoherent state loses stability at $K = 0$. Thus using Eq. (5.15) allows us to perform the stability analysis of a state easily without having to solve the partial differential equation of the dynamics of the distribution of agents in both $\boldsymbol{\sigma}$ and t as was necessary in Chapter 3.

5.4.3 Other Examples

Extensions appropriate to various contexts may be studied using Eq. (5.14).

For example, each of the agents in the model described above could have a bias towards a particular subspace, such as birds in a flock that have a preference to align parallel to the surface of the Earth. In this case, the common field of such a system is then defined similar to Eq. (5.17) as

$$\boldsymbol{\rho}(\boldsymbol{\eta}, t) = K[(1 - c)\mathbf{z} + c\boldsymbol{\Pi}\mathbf{z}], \quad (5.27)$$

where $\boldsymbol{\Pi}$ is the operator that projects onto the preferred subspace (e.g., if \hat{x} , \hat{y} and \hat{z} are unit vectors in rectangular coordinates with \hat{z} being vertical, then $\boldsymbol{\Pi} = \hat{x}\hat{x}^T + \hat{y}\hat{y}^T$ would represent the preference to align to a horizontal surface), and $0 \leq c \leq 1$ models the strength of the preference. Writing \mathbf{z} using Eq. (5.18), along with Eq. (5.15) then represents the reduced equations for this problem.

Another extension to the Kuramoto model that is often studied is the Kuramoto-Sakaguchi model [88]. In this model the $\sin(\theta_j - \theta_i)$ coupling term of the Kuramoto model is replaced with $\sin(\theta_j - \theta_i + \delta)$. A possible generalization of this to higher dimensions, is represented by defining $\boldsymbol{\rho}$ as $\boldsymbol{\rho} = K\mathbf{R}\mathbf{z}$, where \mathbf{R} is a given rotation matrix (for $D = 2$, \mathbf{R} is the two-dimensional rotation matrix that rotates vectors by an angle of δ).

Another D -dimensional generalization whose analysis can be facilitated by the ansatz Eq. (5.14) is the consideration of time delay, $\boldsymbol{\rho}(t) = K\mathbf{z}(t - \tau)$, as studied

for $D = 2$ in Ref. [26].

Also, we note that interactions between multiple communities of Kuramoto-like agents has received attention due to a variety of applications (e.g. Refs. [87, 97, 98]), as well as the presence of interesting dynamics, such as chimera states [87]. For example, for the case of homogenous natural rotations of \mathbf{W}_ξ within each community ξ ,

$$\partial_t \boldsymbol{\alpha}_\xi = \frac{1}{2}(1 + |\boldsymbol{\alpha}_\xi|^2) \boldsymbol{\rho}_\xi - (\boldsymbol{\rho}_\xi \cdot \boldsymbol{\alpha}_\xi) \boldsymbol{\alpha}_\xi + \mathbf{W}_\xi \boldsymbol{\alpha}_\xi, \quad (5.28)$$

where the subscript ξ denotes quantities applying to community ξ . For a case of generalizing the Kuramoto model, we define the order parameter \mathbf{z}_ξ for community ξ as the average orientation of that community, and take $\boldsymbol{\rho}_\xi$ to be

$$\boldsymbol{\rho}_\xi = \sum_{\xi'} K_{\xi, \xi'} \mathbf{z}_{\xi'},$$

with $K_{\xi, \xi'}$ representing the coupling between community ξ and ξ' . The order parameters \mathbf{z}_ξ can be written in terms of $\boldsymbol{\alpha}_\xi$ using Eq. (5.18) by writing the distribution of rotations for the community ξ as $\delta(\mathbf{W} - \mathbf{W}_\xi)$.

The Kuramoto model with the order parameter defined as Eq. (5.16) is the globally-coupled Kuramoto model, wherein each agent is coupled to every other agent. In two dimensions, network-based interaction of agents in Kuramoto-like models have been solved for by an application of the ansatz Eq. (5.5) for a wide range of network topologies, via a mean-field approach [47]. An analogous analysis will apply for our generalized ansatz, Eq. (5.14), for network-based interactions of

D -dimensional Kuramoto-like units.

5.5 Discussion and Conclusions

There are some strong differences between the case $D = 2$ and the case of $D > 2$ that must be considered in general. In the case of $D = 2$, making the additional assumption that $g(\eta)$ is a suitable analytic distribution of the scalar parameter η (e.g., a Lorentzian distribution is often employed), allows the integral in Eq. (5.18) to be performed via a contour integral, and hence requiring the dynamics of $\alpha(\eta)$ according to Eq. (5.15) to be calculated for only one or a few particular complex values of η [18]. In $D = 2$ this implies that many problems of the form Eq. (5.1) with heterogeneous η_i reduce to a system of a small number of ordinary differential equations in the $N \rightarrow \infty$ limit. For our generalization to higher dimension (where η is now a vector parameter with at least two components), we are unable to straightforwardly employ contour integration. Thus, while Eq. (5.14) represents a strong reduction in the dimensionality of the dynamics as compared to the full system in the $N \rightarrow \infty$ limit, i.e., Eq. (5.3), it is still not a ‘low-dimensional system’ in the sense of Ref. [18], since we must still calculate the dynamics of $\alpha(\eta, t)$ as a function of the vector parameter η (as opposed to integrating η away via, e.g., a Lorentzian assumption for $g(\eta)$).

For the case of homogenous systems, i.e., where $g(\eta)$ is the Dirac-delta function, the dynamics of the full system Eq. (5.2) reduces to the single D dimensional differential equation Eq. (5.15). For the particular case of the Kuramoto model

generalized to higher dimensions in the manner given in Sec. 5.4.1, this exactly reproduces recent results by Lohe [91] for the case of a finite number of homogenous agents derived in the context of a generalization of the Watanabe-Strogatz (WS) transform [99,100]. In 2014 Tanaka [92] considered a generalization of the Kuramoto model with higher dimensional *complex* vectors. In this setup (which is different from ours) he derived an extension of the Ott-Antonsen method in the context of a generalized WS transform. In 2008, Pikovsky and Rosenblum [101] demonstrated that there is a relationship between the WS transform and the Ott-Antonsen ansatz in the case of the original ($D = 2$ in our notation) Kuramoto model. It is possible that similar relationships may exist between our generalization of the Ott-Antonsen ansatz Eqs. (5.14), (5.15) and the generalization of the WS transform described in Refs. [91,92] — we leave the study of this relationship to future work.

In conclusion, we have developed a technique to tackle the generalization of several Kuramoto-like systems into higher dimensions. While our analysis has only demonstrated the existence of an invariant manifold to the dynamics of Eq. (5.3), from numerical experiments we observe for all examined examples of systems given Eq. (5.2) with a continuous distribution $g(\eta)$ that this manifold is attracting. That is, initial conditions set up not satisfying Eq. (5.14) appear to be rapidly attracted towards this invariant manifold. While, in the case of $D = 2$, it has been shown analytically that, for a broad class of models of the form given by Eq. (5.1), this manifold is a global attractor of the dynamics [19], proof of attraction for $D > 2$ remains an open problem. Given the wide applicability of Eq. (5.1) and its rich variety of dynamical phenomena, we expect that the generalization to higher

dimensions, Eq. (5.2), may be a useful model system, applicable to diverse situations of interest, while remaining amenable to analysis via the methods developed in this chapter.

Chapter 6: Conclusions

The Kuramoto Model has been the subject of intense study over the last few decades. This stems from the simplicity of the model allowing for detailed mathematical study, while supporting complex dynamical behavior. In this thesis we have discussed extensions of the Kuramoto model that allow for applications in new setups, while remaining accessible to rigorous analysis.

In Chapter 2, we studied an extension of the Kuramoto model that describes the dynamics of large networks of theta neurons. We used the Ott-Antonsen ansatz to derive a set of reduced equations that exactly describe the dynamics of the collective behavior of the neurons in the network in the infinite size limit. The dynamics described by these reduced equations were found to be in close agreement with the full network of neurons in all cases. Thus, this reduced system of equations allowed us to efficiently study system, including the effect of the network topology in terms of the degree distribution and assortativity. In terms of the range of dynamical behavior, we showed that the network of neurons displays three phases: resting states, asynchronously firing states and synchronously firing states, the first two of which appear as a fixed point for the order parameter, while the third appears as a limit cycle for the order parameter. Remarkably, in networks with a skewed

degree distribution, the synchronously firing state was found to only occur in networks with neutral or weak assortativity — moderate amounts of assortativity or disassortativity pushed the network into asynchronously firing state instead.

In Chapter 3, we generalize the Kuramoto model to arbitrary dimensions, describing a system of interacting, orientable units, whose state is completely described by D -dimensional unit vectors. This is a natural generalization to consider when studying agents whose state is higher than two dimensional, such as swarming drones, flocking birds, opinion dynamics, classical D -dimensional spins, and several others. One of the main results discussed in the chapter is that the nature of the phase transition has a strong dependence on the dimensionality of the system. Odd-dimensional generalizations of the Kuramoto model display a non-hysteretic, discontinuous phase transition to coherence that occurs as the coupling strength increases through zero. In contrast, even-dimensional generalizations (including the standard Kuramoto model) display a continuous phase transition to coherence at a positive critical coupling strength. To further motivate the application of our results on swarming and flocking behavior we extended our model to describe extended-body agents; this extension continued to demonstrate the remarkably different behavior in odd and even dimensions, indicating that our results apply not just to the Kuramoto model, but more generally to aligning agents in two and three dimensions.

Chapter 4 discusses the particular case of even dimensional generalizations to the Kuramoto model. Unlike the case of the standard ($D = 2$) Kuramoto model, we showed that for even $D \geq 4$ there are an infinite number of time-independent distributions of agents (defining the manifold \mathcal{M}) that correspond to the completely

incoherent distribution (i.e., having $|\rho|=0$) in the infinite system-size limit. Further, we showed that the distributions on this manifold have varying critical coupling strengths K_c , lying in the range $K_c^{(-)} < K_c < K_c^{(+)} = 2K_c^{(-)}$, and conversely, for each K_c within the range $K_c^{(-)} < K_c < K_c^{(+)}$ there is a distribution that loses its stability at that coupling strength. These properties result in transitions within the $|\rho|=0$ manifold as the coupling strength is varied through this range, which can be observed as short-lived macroscopic bursts in the value of $|\rho|$. After each such transition the critical coupling strength is *reset* to a higher value, via a process that we termed as Instability-Mediated Resetting. We showed that via this process the critical coupling strength is continually reset as the coupling strength is increased, until it attains the maximum possible value of $K_c^{(+)}$ at which point the macroscopic phase transition to coherence is observed. Thus, via the results in this chapter we reconcile the critical coupling strength as calculated from stability of the incoherent states of the generalized Kuramoto model (resulting in a range of critical couplings in $[K_c^{(-)}, K_c^{(+)})$) and the critical coupling strength as calculated from the existence of stable coherent states (resulting in a single critical coupling of $K_c^{(+)}$, corresponding to the value we calculate in Chapter 3).

In Chapter 5, we develop a method to analyze the generalized Kuramoto model and other Kuramoto-like systems. Analogous to the Ott-Antonsen ansatz for the standard Kuramoto model [18], we showed the existence of an invariant manifold to the dynamics of the wide generalization of the Kuramoto model (described in Eq. (5.2)) in the infinite size limit. Unlike the standard Kuramoto model, however, we were unable to show that this invariant manifold was attracting. Nonetheless, our

numerical experiments have suggested that this manifold is attracting, and thus our results describing the dynamics on this manifold are important in describing the Kuramoto-like models that we have considered.

Thus, in this thesis, we have constructed models that build on an underlying framework of the Kuramoto model, while describing new and interesting dynamics. Our models describe dynamics that include spiking neurons, flocking birds, opinion dynamics, classical spins, and several other systems, owing to the general classes of models that we have set up. Further, using the mathematical tools and techniques that we have devised, we can perform a detailed analysis, leading to theoretical insights into these systems and new scientific understanding in a wide variety of physical, biological and social systems.

Appendix A: Additional proofs pertinent to Chapter 3

A.1 Equation for fixed points of agents

We here present a derivation of Eq. (3.11). In what follows in this appendix, we write the fixed point solution of the i^{th} agent, i.e., σ_i^F in Eq. (3.9) as simply σ . We also similarly drop the index i from μ_i and $\hat{\omega}_i$ for simplicity of notation.

Taking the second term on the left-hand side of Eq. (3.11) to the right-hand side and considering the square of the norm of both sides, we obtain

$$[1 - (\hat{\rho} \cdot \sigma)^2] = [1 - (\hat{\omega} \cdot \sigma)^2] \mu^2. \quad (\text{A.1})$$

Also, dotting Eq. (3.9) with $\hat{\omega}$ we obtain

$$\hat{\rho} \cdot \hat{\omega} = (\hat{\rho} \cdot \sigma)(\hat{\omega} \cdot \sigma) \quad (\text{A.2})$$

Using Eq. (A.2) to replace the term $(\hat{\omega} \cdot \sigma)$ in Eq. (A.1) we obtain

$$1 - (\hat{\rho} \cdot \sigma)^2 = \left(1 - \frac{(\hat{\rho} \cdot \hat{\omega})^2}{(\hat{\rho} \cdot \sigma)^2}\right) \mu^2. \quad (\text{A.3})$$

Thus we have

$$1 - (\hat{\rho} \cdot \sigma)^2 = \mu^2 - \frac{(\hat{\rho} \cdot \hat{\omega})^2}{(\hat{\rho} \cdot \sigma)^2} \mu^2 = 0, \quad (\text{A.4})$$

which is a quadratic equation in $(\hat{\rho} \cdot \sigma)^2$, whose solution is Eq. (3.10). For $K > 0$ the positive solution Eq. (3.10) will be stable, as is argued in the text. Equation (3.9) dotted with $\hat{\rho}$ gives

$$[1 - (\hat{\rho} \cdot \sigma)^2] + \mu \hat{\rho} \cdot (\hat{\omega} \times \sigma) = 0. \quad (\text{A.5})$$

This can be rewritten using Eq. (A.1) as

$$\hat{\omega} \cdot [\mu \hat{\omega} - \mu(\hat{\omega} \cdot \sigma)\sigma + \sigma \times \hat{\rho}] = 0. \quad (\text{A.6})$$

Keeping $\hat{\omega}$ fixed, we can independently choose K , and hence μ . Thus the term in Eq. (A.6) in the square brackets must be independently zero.

$$\mu \hat{\omega} - \mu(\hat{\omega} \cdot \sigma)\sigma + \sigma \times \hat{\rho} = 0. \quad (\text{A.7})$$

Using Eq. (A.2) again we obtain

$$\hat{\rho} \times \sigma = \mu(\hat{\omega} - \xi\sigma), \quad (\text{A.8})$$

where

$$\xi = \frac{\hat{\rho} \cdot \hat{\omega}}{\hat{\rho} \cdot \sigma}. \quad (\text{A.9})$$

Since the solution to $\mathbf{a} \times \mathbf{b} = \mathbf{c}$, is $\mathbf{b} = (\mathbf{c} \times \mathbf{a})/|\mathbf{a}|^2 + t\mathbf{a}$ for any t ,

$$\boldsymbol{\sigma} = ((\hat{\boldsymbol{\omega}} \times \hat{\boldsymbol{\rho}}) - \xi(\boldsymbol{\sigma} \times \hat{\boldsymbol{\rho}}))\mu + t\hat{\boldsymbol{\rho}}. \quad (\text{A.10})$$

Dotting both sides of Eq. (A.10) with $\hat{\boldsymbol{\rho}}$, we see that $t = \hat{\boldsymbol{\rho}} \cdot \boldsymbol{\sigma}$, which was solved for earlier, resulting in Eq. (3.10). We now go back to Eq. (A.10) and use Eq. (A.8) to obtain

$$\boldsymbol{\sigma} = (\mu(\hat{\boldsymbol{\omega}} \times \hat{\boldsymbol{\rho}}) + \mu^2\xi(\hat{\boldsymbol{\omega}} - \xi\boldsymbol{\sigma})) + t\hat{\boldsymbol{\rho}}, \quad (\text{A.11})$$

which can be rearranged to give

$$\boldsymbol{\sigma} = \frac{1}{1 + \xi^2\mu^2} [\mu(\hat{\boldsymbol{\omega}} \times \hat{\boldsymbol{\rho}}) + \xi\mu^2\hat{\boldsymbol{\omega}} + t\hat{\boldsymbol{\rho}}], \quad (\text{A.12})$$

with $t = \hat{\boldsymbol{\rho}} \cdot \boldsymbol{\sigma}$ and ξ according to Eq. (A.9). This completes our derivation of Eq. (3.11)

A.2 Simplification of continuity equation

In this appendix we give a derivation of Eq. (3.27) from Eq. (3.25). We present this proof in arbitrary dimensions, where we rewrite Eq. (3.26) as

$$\mathbf{v} = K[\boldsymbol{\rho} - (\boldsymbol{\sigma} \cdot \boldsymbol{\rho})\boldsymbol{\sigma}] + \mathbf{W}\boldsymbol{\sigma}, \quad (\text{A.13})$$

where \mathbf{v} is defined on the $(D-1)$ -dimensional surface of the unit sphere \mathcal{S} embedded in D dimensions. To simplify the continuity equation for the flow along the surface

\mathcal{S} , i.e., Eq. (3.25), we first extend the velocity flow field to the entire space \mathbb{R}^D by allowing $\boldsymbol{\sigma}$ to be a general D -vector (rather than restricting it to a unit vector). We then write the continuity equation using the regular divergence defined over the entire space, and demonstrate that this reduces to Eq. (3.27) when considered on the surface \mathcal{S} .

We write $\boldsymbol{\sigma} = r\hat{\mathbf{r}}$. Let the velocity flow field as extended to \mathbb{R}^D be

$$\mathbf{v}_\sigma = \mathbf{W}\hat{\mathbf{r}} + K[\boldsymbol{\rho} - \hat{\mathbf{r}}(\boldsymbol{\rho} \cdot \hat{\mathbf{r}})], \quad (\text{A.14})$$

$$= \mathbf{W}\boldsymbol{\sigma}/r + K[\boldsymbol{\rho} - \boldsymbol{\sigma}(\boldsymbol{\rho} \cdot \boldsymbol{\sigma})/r^2]. \quad (\text{A.15})$$

Note that this extension to \mathbb{R}^D can be performed in multiple ways and does not affect our final result. Since $\hat{\mathbf{r}} \cdot \mathbf{v}_\sigma = 0$, this flow field maintains the surfaces of spheres centered at $r = 0$ as invariant manifolds. We then extend the distribution $f(\boldsymbol{\sigma}, t)$, that was defined on the surface \mathcal{S} , to the entire space \mathbb{R}^D as

$$\mathcal{F}(\hat{\mathbf{r}}, r, \mathbf{W}, t) = f(\hat{\mathbf{r}}, \mathbf{W}, t)\delta(r - 1), \quad (\text{A.16})$$

where $\delta(\cdot)$ is the Dirac delta function. We can write the continuity equation for the flow in \mathbb{R}^D as

$$\begin{aligned} 0 &= \partial_t \mathcal{F} + \boldsymbol{\nabla} \cdot [\mathbf{v}_\sigma \mathcal{F}], \\ &= \partial_t \mathcal{F} + \mathbf{v}_\sigma \cdot \boldsymbol{\nabla} \mathcal{F} + \mathcal{F} \boldsymbol{\nabla} \cdot \mathbf{v}_\sigma. \end{aligned} \quad (\text{A.17})$$

We express $\nabla\mathcal{F}$ as

$$\nabla\mathcal{F} = \frac{1}{r}\nabla_{\mathcal{S}}\mathcal{F} + \hat{\mathbf{r}}\frac{\partial\mathcal{F}}{\partial r}, \quad (\text{A.18})$$

where $\nabla_{\mathcal{S}}\mathcal{F}$ is the component of the gradient of \mathcal{F} along the surface \mathcal{S} , as has been described in the main text. Since $\mathbf{v}_{\sigma} \cdot \hat{\mathbf{r}} = 0$, and $\nabla \cdot \mathbf{W}\boldsymbol{\sigma} = 0$, we can simplify Eq.

(A.17) to

$$\begin{aligned} \partial_t\mathcal{F} + (1/r)\{\mathbf{W}\boldsymbol{\sigma}/r + [\boldsymbol{\rho} - \boldsymbol{\sigma}(\boldsymbol{\rho} \cdot \boldsymbol{\sigma})/r^2]\} \cdot \nabla_{\mathcal{S}}\mathcal{F} \\ + \mathcal{F}\nabla \cdot [\boldsymbol{\rho} - \boldsymbol{\sigma}(\boldsymbol{\rho} \cdot \boldsymbol{\sigma})/r^2] = 0. \end{aligned} \quad (\text{A.19})$$

Now,

$$\begin{aligned} \nabla \cdot \left[\boldsymbol{\rho} - \frac{\boldsymbol{\sigma}(\boldsymbol{\rho} \cdot \boldsymbol{\sigma})}{r^2} \right] &= -\nabla \cdot \left(\frac{\boldsymbol{\sigma}(\boldsymbol{\rho} \cdot \boldsymbol{\sigma})}{r^2} \right), \\ &= - \left[\frac{\boldsymbol{\rho} \cdot \boldsymbol{\sigma}}{r^2} \nabla \cdot \boldsymbol{\sigma} + \boldsymbol{\sigma} \cdot \nabla \frac{\boldsymbol{\rho} \cdot \boldsymbol{\sigma}}{r^2} \right], \\ &= -\frac{\boldsymbol{\sigma} \cdot \boldsymbol{\rho}}{r^2}(D-1). \end{aligned}$$

Also note that

$$[\boldsymbol{\rho} - \boldsymbol{\sigma}(\boldsymbol{\rho} \cdot \boldsymbol{\sigma})/r^2] \cdot \nabla_{\mathcal{S}}\mathcal{F} = \boldsymbol{\rho} \cdot \nabla_{\mathcal{S}}\mathcal{F},$$

since $\boldsymbol{\sigma} \cdot \nabla_{\mathcal{S}}\mathcal{F} = 0$ by the definition of $\nabla_{\mathcal{S}}\mathcal{F}$. Thus, Eq. (A.19) simplifies to

$$\frac{\partial\mathcal{F}}{\partial t} + \frac{1}{r}(\mathbf{W}\hat{\mathbf{r}} + \boldsymbol{\rho}) \cdot \nabla_{\mathcal{S}}\mathcal{F} - (D-1)\mathcal{F}\hat{\mathbf{r}} \cdot \boldsymbol{\rho}. \quad (\text{A.20})$$

Integrating the above equation over r from $1-\epsilon$ to $1+\epsilon$ for small ϵ , gives the desired result Eq. (3.27).

A.3 Critical coupling constant for even dimensions

We now determine K_c for even $D = 2\Lambda$ as that value of K such that $|\boldsymbol{\rho}| \rightarrow 0$ with $|\boldsymbol{\rho}| \neq 0$ as $K \rightarrow K_c$ from above. For notational simplicity, we write $\rho = |\boldsymbol{\rho}|$. As discussed earlier in Sec. 3.3.3, \mathbf{W} can be written as $\mathbf{W} = \mathbf{R}^T \mathbf{D} \mathbf{R}$, where \mathbf{R} is an orthogonal matrix, and \mathbf{D} is a block-diagonal matrix with the j^{th} block being a 2×2 antisymmetric matrix with nonzero entries ω_j and $-\omega_j$ for all $j \in \{1, \dots, \Lambda\}$. By construction, we choose $G(\mathbf{W})$ to be a distribution invariant to rotation, and hence we can rewrite $G(\mathbf{W})$ as

$$G(\mathbf{W}) = g(\{\omega_i\})U[\mathbf{R}], \quad (\text{A.21})$$

where $\{\omega_i\} = \{\omega_1, \omega_2, \dots, \omega_\Lambda\}$ represents the set of associated frequencies for each of the 2×2 blocks of \mathbf{D} , with $g(\{\omega_i\})$ representing the joint distribution of these frequencies, and $U[\mathbf{R}]$ representing the uniform distribution of orthogonal matrices (corresponding to the Haar measure on the group of orthogonal matrices). We then write Eq. (3.41) as,

$$\rho^2 = \int_{\mathbf{R}} \int_{\Gamma} \gamma(\{\omega_i\}, \{\rho_i\}) g(\{\omega_i\}) d\omega_1 \dots d\omega_\Lambda U[\mathbf{R}] d\mathbf{R}. \quad (\text{A.22})$$

Recall that ρ_k^2 is the sum of the squares of the magnitudes of component $2k - 1$ and component $2k$ of $\boldsymbol{\rho}$ in the basis that block-diagonalized \mathbf{W} , corresponding to the components of $\boldsymbol{\rho}$ that are acted on by the k^{th} block of \mathbf{W} .

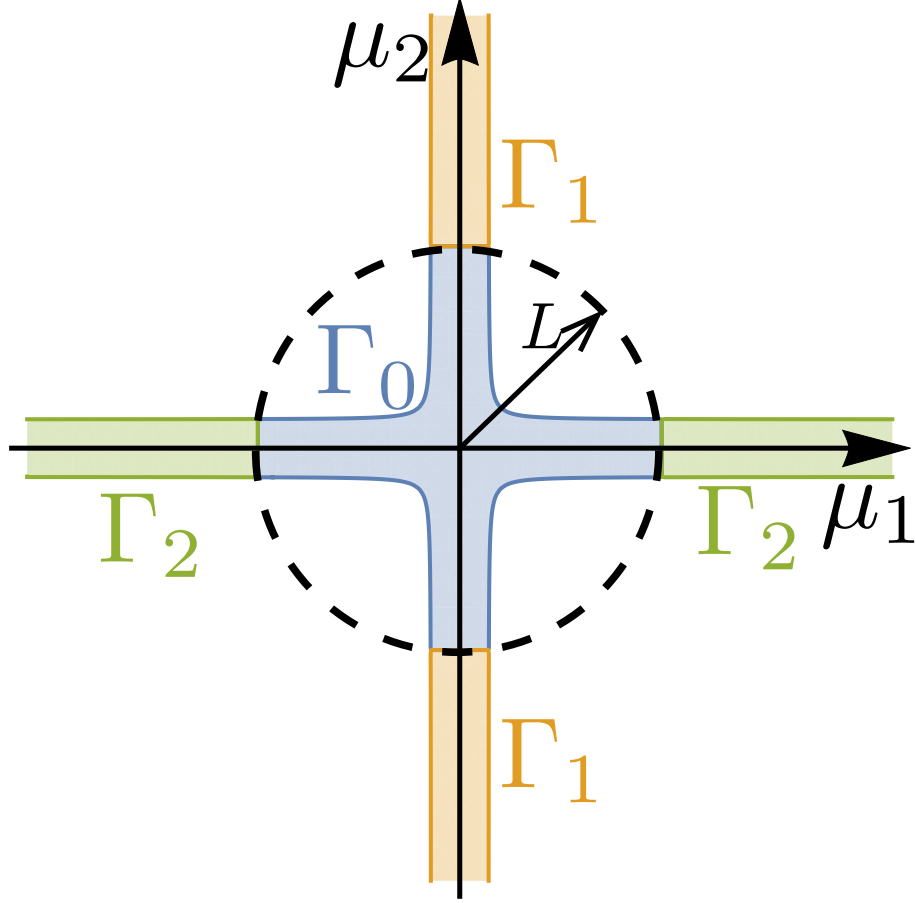


Figure A.1: The shaded regions (in blue, green and orange) correspond to the domain Γ in which $\sum_k 1/\mu_k^2 > 1$ for the case of $D = 4$ ($\Lambda = 2$) in the $\{\mu_1, \mu_2\}$ -space. The subdomain Γ_0 , shown in blue, is the part of Γ inside the circle of radius L ; and the subdomains Γ_i are the parts of the domain Γ that lie outside Γ_0 which do not contain the μ_i axis (Γ_1 is shown in orange, and Γ_2 in green). The width of the strips in Γ far away from the origin is 1, hence the volume of the subdomain Γ_0 will scale as $\mathcal{O}(L^{\Lambda-1})$ for large L .

Define $\mu_i = \omega_i/(K\rho_i)$. In $\{\mu_i\}$ -space, Γ is the region $\sum_k 1/\mu_k^2 > 1$, shown in Fig. A.1.

Then

$$\rho^2 = \int_{\mathbf{R}} \int_{\Gamma} \gamma g(\{\mu_i K \rho_i\}) K^\Lambda \rho_1 d\mu_1 \dots \rho_\Lambda d\mu_\Lambda U[\mathbf{R}] d\mathbf{R}. \quad (\text{A.23})$$

We next define a quantity $L \gg 1$ by choosing $L \sim \mathcal{O}(\rho^{-1/2})$. Since we are interested in $\rho \rightarrow 0$, $L \rightarrow \infty$. Taking motivation from the shape of the domain Γ

shown in Fig. (A.1), we express Γ as the disjoint union of $\Gamma_0, \Gamma_1, \dots, \Gamma_\Lambda$, where Γ_0 is the component of Γ within the dashed circle of radius L in Fig. A.1, and for $j \geq 1$, Γ_j is the region for which $|\mu_j| \lesssim 1$ and $|\mu_k| \geq L$ for all $k \neq j$.

Note that the left-hand side of Eq. (3.41) is ρ^2 , hence we can ignore terms on the right-hand side of order smaller than $\mathcal{O}(\rho^2)$. We now show that the contribution from Γ_0 is of a smaller order than this. By construction, in the subdomain Γ_0 , $|\mu_i| \leq L$, and hence $\mu_i K \rho_i \sim \mathcal{O}(\sqrt{\rho}) \rightarrow 0$ as $\rho \rightarrow 0$. Further, $\gamma = \boldsymbol{\rho} \cdot \boldsymbol{\sigma}^F \leq \rho$. Thus the contribution \mathcal{I}_{Γ_0} to the integral in Eq. (A.23) from the subdomain Γ_0 will be

$$\begin{aligned} \mathcal{I}_{\Gamma_0} &\lesssim \int_{\Gamma_0} \rho g(0, \dots, 0) K^\Lambda \rho_1 d\mu_1 \dots \rho_\Lambda d\mu_\Lambda \\ &\sim \mathcal{O}[\rho^{\Lambda+1} \text{Volume}(\Gamma_0)]. \end{aligned}$$

Since $L \gg 1$, the volume of Γ_0 will scale as $\mathcal{O}(L^{\Lambda-1}) \sim \mathcal{O}(\rho^{-(\Lambda-1)/2})$. Thus $\mathcal{I}_{\Gamma_0} \sim \mathcal{O}(\rho^{(\Lambda+3)/2})$, which for $D > 2$ is negligible compared to ρ^2 and the contributions to the integrals in Eq. (A.23) from the subdomains Γ_j . Since K_c for $D = 2$ is already known (e.g. Ref. [16]), we focus on the cases $D \geq 4$, and hence will ignore the contribution from the subdomain Γ_0 . By symmetry, each Γ_i will give the same contribution. Hence, without loss of generality, we will look at the contribution from the subdomain Γ_1 , and will append a factor of Λ . We will also only look at $\mu_i > 0$

and will hence append a factor of 2^Λ .

$$\rho^2 = \Lambda 2^\Lambda \int_{\mathbf{R}} \int_{\mu_1=0}^1 \int_{\mu_2=L}^\infty \cdots \int_{\mu_\Lambda=L}^\infty \gamma g(\{\mu_i K \rho_i\}) K^\Lambda \rho_1 d\mu_1 \dots \rho_\Lambda d\mu_\Lambda U[\mathbf{R}] d\mathbf{R}$$

Going back to Eq. (3.37), we rewrite it as

$$\sum_k \frac{1}{\gamma^2/\rho_k^2 + \mu_k^2} = 1. \quad (\text{A.24})$$

In the subdomain Γ_1 , $\mu_i \gg \mu_1$ for all $i \geq 2$, and thus we can use the above equation in the small ρ_1 approximation,

$$1 \cong \frac{1}{\gamma^2/\rho_1^2 + \mu_1^2}, \quad (\text{A.25})$$

$$\gamma \cong \sqrt{\rho_1^2(1 - \mu_1^2)}. \quad (\text{A.26})$$

Also, $\mu_1 < 1$ implies $\mu_1 K \rho_1 \sim \mathcal{O}(\rho) \rightarrow 0$ as $\rho \rightarrow 0$. Thus,

$$\rho^2 = \Lambda 2^\Lambda K^\Lambda \int_{\mathbf{R}} \int_{\mu_2=L}^\infty \cdots \int_{\mu_\Lambda=L}^\infty \int_{\mu_1=0}^1 \rho_1 \sqrt{1 - \mu_1^2} d\mu_1 g(0, \{\mu_i K \rho_i\}_{i=2}^\Lambda) \rho_1 \dots \rho_\Lambda d\mu_2 \dots d\mu_\Lambda U[\mathbf{R}] d\mathbf{R}. \quad (\text{A.27})$$

We then change variables back to ω_i for each of the μ_i integrals for $i = 2 \dots \Lambda$, and explicitly evaluate the integral over μ_1 . The lower limits of the integrals change from L to $LK\rho_i$ which goes to zero in the limit of small ρ , since $L \sim \mathcal{O}(\rho^{-1/2})$. Thus

$$\begin{aligned}
\rho^2 &= \Lambda 2^\Lambda K \frac{\pi}{4} \int_{\mathbf{R}} \int_0^\infty \dots \int_0^\infty g(0, \{\omega_i\}_{i=2}^\Lambda) \rho_1^2 \\
&\quad d\omega_2 \dots d\omega_\Lambda U[\mathbf{R}] d\mathbf{R}, \\
&= \Lambda 2^\Lambda K \frac{\pi}{4} \int_{\mathbf{R}} \rho_1^2 \frac{\tilde{g}(0)}{2^{\Lambda-1}} U[\mathbf{R}] d\mathbf{R}, \tag{A.28}
\end{aligned}$$

where

$$\tilde{g}(0) = 2^{\Lambda-1} \int_0^\infty \dots \int_0^\infty g(0, \{\omega_i\}_{i=2}^\Lambda) d\omega_2 \dots d\omega_\Lambda, \tag{A.29}$$

equivalent to the definition given earlier in Eq. (3.44). Since $U[\mathbf{R}]$ is the uniform distribution, thus by symmetry

$$\begin{aligned}
\Lambda \int_{\mathbf{R}} \rho_1^2 U[\mathbf{R}] d\mathbf{R} &= \int_{\mathbf{R}} \sum_k^\Lambda \rho_k^2 U[\mathbf{R}] d\mathbf{R} \\
&= \int_{\mathbf{R}} \rho^2 U[\mathbf{R}] d\mathbf{R} \\
&= \rho^2 \tag{A.30}
\end{aligned}$$

Inserting Eqs. (A.29) and (A.30) into Eq. (A.28) gives us

$$\rho^2 = 2^\Lambda K_c \frac{\pi}{4} \rho^2 \frac{\tilde{g}(0)}{2^{\Lambda-1}}.$$

Since we are in the limit of small but *nonzero* ρ , we can cancel ρ^2 from both sides to obtain the desired result in Eq. (3.42)

Appendix B: Additional proof pertinent to Chapter 5

B.1 Proof of Eq. (5.15)

Inserting the form of $f(\boldsymbol{\sigma}, \eta, t)$ from Eq. (5.14) into Eq. (5.9) we obtain

$$\begin{aligned} & [(D-1)(1-|\boldsymbol{\alpha}|^2)^{D-2}] \{ (1+|\boldsymbol{\alpha}|^2-2\boldsymbol{\alpha}\cdot\boldsymbol{\sigma})(-2\boldsymbol{\alpha}\cdot\partial_t\boldsymbol{\alpha}) \\ & - (1-|\boldsymbol{\alpha}|^2)(2\boldsymbol{\alpha}\cdot\partial_t\boldsymbol{\alpha}-2\boldsymbol{\sigma}\cdot\partial_t\boldsymbol{\alpha}) \\ & + (1-|\boldsymbol{\alpha}|^2)[2(\boldsymbol{\alpha}\cdot\boldsymbol{\rho})-(\boldsymbol{\rho}\cdot\boldsymbol{\sigma})(1+|\boldsymbol{\alpha}|^2)-2\boldsymbol{\sigma}\cdot W\boldsymbol{\alpha}] \} = 0. \end{aligned} \quad (\text{B.1})$$

Remarkably, the explicit D dependence of the differential equation cancels out, and a differential equation involving only terms that are linear and constant in $\boldsymbol{\sigma}$ remains.

For this equation to be identically zero for each direction $\boldsymbol{\sigma}$, the linear and constant terms must independently be zero. From the constant term we obtain

$$\begin{aligned} & (1+|\boldsymbol{\alpha}|^2)(-2\boldsymbol{\alpha}\cdot\partial_t\boldsymbol{\alpha}) - (1-|\boldsymbol{\alpha}|^2)(2\boldsymbol{\alpha}\cdot\partial_t\boldsymbol{\alpha}) \\ & + (1-|\boldsymbol{\alpha}|^2)(2(\boldsymbol{\alpha}\cdot\boldsymbol{\rho})) = 0, \end{aligned}$$

which simplifies to

$$\boldsymbol{\alpha}\cdot\partial_t\boldsymbol{\alpha} = (1/2)(1-|\boldsymbol{\alpha}|^2)(\boldsymbol{\rho}\cdot\boldsymbol{\alpha}), \quad (\text{B.2})$$

or alternately

$$\partial_t|\boldsymbol{\alpha}| = \left(\frac{1-|\boldsymbol{\alpha}|^2}{2|\boldsymbol{\alpha}|} \right) (\boldsymbol{\rho}\cdot\boldsymbol{\alpha}). \quad (\text{B.3})$$

From the $\boldsymbol{\sigma}$ dependent portion we get

$$\boldsymbol{\sigma} \cdot [2\boldsymbol{\alpha}(2\boldsymbol{\alpha} \cdot \partial_t \boldsymbol{\alpha}) + (1 - |\boldsymbol{\alpha}|^2)(2\partial_t \boldsymbol{\alpha}) - k(1 - |\boldsymbol{\alpha}|^2)(1 + |\boldsymbol{\alpha}|^2)\boldsymbol{\rho} - 2(1 - |\boldsymbol{\alpha}|^2)W\boldsymbol{\alpha}] = 0.$$

Since $\boldsymbol{\sigma}$ is allowed to be in any direction, we can cancel out the $\boldsymbol{\sigma}$ and obtain a vector equation that must be satisfied. To further simplify this vector expression, we write

$$\partial_t \boldsymbol{\alpha} = \partial_t (|\boldsymbol{\alpha}| \hat{\boldsymbol{\alpha}}) = |\boldsymbol{\alpha}| \partial_t \hat{\boldsymbol{\alpha}} + \hat{\boldsymbol{\alpha}} \partial_t |\boldsymbol{\alpha}|, \text{ where } \hat{\boldsymbol{\alpha}} \text{ is a unit vector in the direction of } \boldsymbol{\alpha}.$$

We can then use Eqs. (B.2) and (B.3) to simplify the expression to obtain

$$\partial_t \hat{\boldsymbol{\alpha}} = \left(\frac{1 + |\boldsymbol{\alpha}|^2}{2|\boldsymbol{\alpha}|} \right) (\boldsymbol{\rho} - (\boldsymbol{\rho} \cdot \hat{\boldsymbol{\alpha}})\hat{\boldsymbol{\alpha}}) + W\hat{\boldsymbol{\alpha}}. \quad (\text{B.4})$$

Equations (B.3) and (B.4) can then be combined to obtain Eq. (5.15).

Bibliography

- [1] Arthur T Winfree. Biological rhythms and the behavior of populations of coupled oscillators. *Journal of theoretical biology*, 16(1):15–42, 1967.
- [2] Yoshiki Kuramoto. Self-entrainment of a population of coupled non-linear oscillators. In *International symposium on mathematical problems in theoretical physics*, pages 420–422. Springer, 1975.
- [3] Yoshiki Kuramoto. *Chemical oscillations, waves, and turbulence*. Springer, 1984.
- [4] Motohisa Osaka. Modified kuramoto phase model for simulating cardiac pacemaker cell synchronization. *Applied Mathematics*, 8(09):1227, 2017.
- [5] B. Ermentrout. An adaptive model for synchrony in the firefly *Pteroptyx malaccae*. *Journal of Mathematical Biology*, 29(6):571–585, jun 1991.
- [6] John Buck and Elisabeth Buck. Mechanism of Rhythmic Synchronous Flashing of Fireflies. *Science*, 159(3821), 1968.
- [7] TM Antonsen Jr, RT Faghiih, M Girvan, E Ott, and J PlatiG. External periodic driving of large systems of globally coupled phase oscillators. *Chaos: An Interdisciplinary Journal of Nonlinear Science*, 18(3):037112, 2008.
- [8] Lauren M. Childs and Steven H. Strogatz. Stability diagram for the forced Kuramoto model. *Chaos: An Interdisciplinary Journal of Nonlinear Science*, 18(4):043128, dec 2008.
- [9] Juan A Acebrón, Luis L Bonilla, Conrad J Pérez Vicente, Félix Ritort, and Renato Spigler. The kuramoto model: A simple paradigm for synchronization phenomena. *Reviews of modern physics*, 77(1):137, 2005.
- [10] B. A. Carreras, V. E. Lynch, I. Dobson, and D. E. Newman. Complex dynamics of blackouts in power transmission systems. *Chaos: An Interdisciplinary Journal of Nonlinear Science*, 14(3):643–652, sep 2004.

- [11] Adilson E. Motter, Seth A. Myers, Marian Anghel, and Takashi Nishikawa. Spontaneous synchrony in power-grid networks. *Nature Physics*, 9(3):191–197, feb 2013.
- [12] Seth A Marvel and Steven H Strogatz. Invariant submanifold for series arrays of Josephson junctions. *Chaos: An Interdisciplinary Journal of Nonlinear Science*, 19, 2009.
- [13] Bihui Zhu, Johannes Schachenmayer, Minghui Xu, F Herrera, Juan G Restrepo, Murray J Holland, and Ana Maria Rey. Synchronization of interacting quantum dipoles. *New Journal of Physics*, 17(8):083063, 2015.
- [14] J. Pantaleone. Stability of incoherence in an isotropic gas of oscillating neutrinos. *Physical Review D*, 58(7):073002, aug 1998.
- [15] Steven Strogatz. *Sync: The emerging science of spontaneous order*. Penguin UK, 2004.
- [16] Steven H Strogatz. From kuramoto to crawford: exploring the onset of synchronization in populations of coupled oscillators. *Physica D: Nonlinear Phenomena*, 143(1):1–20, 2000.
- [17] Edward Ott. *Chaos in dynamical systems*. Cambridge university press, 2002.
- [18] Edward Ott and Thomas M Antonsen. Low dimensional behavior of large systems of globally coupled oscillators. *Chaos: An Interdisciplinary Journal of Nonlinear Science*, 18(3):37113, 2008.
- [19] Edward Ott and Thomas M Antonsen. Long time evolution of phase oscillator systems. *Chaos: An interdisciplinary journal of nonlinear science*, 19(2):23117, 2009.
- [20] Edward Ott, Brian R Hunt, and Thomas M Antonsen Jr. Comment on Long time evolution of phase oscillator systems[Chaos 19, 023117 (2009)]. *Chaos: An Interdisciplinary Journal of Nonlinear Science*, 21(2):25112, 2011.
- [21] Carlo R Laing. The dynamics of chimera states in heterogeneous kuramoto networks. *Physica D: Nonlinear Phenomena*, 238(16):1569–1588, 2009.
- [22] Tanushree B. Luke, Ernest Barreto, and Paul So. Complete Classification of the Macroscopic Behavior of a Heterogeneous Network of Theta Neurons. *Neural Computation*, 25(12):3207–3234, dec 2013.
- [23] Arkady Pikovsky and Michael Rosenblum. Partially integrable dynamics of hierarchical populations of coupled oscillators. *Physical review letters*, 101(26):264103, 2008.
- [24] Diego Pazó and Ernest Montbrió. Existence of hysteresis in the kuramoto model with bimodal frequency distributions. *Physical Review E*, 80(4):046215, 2009.

- [25] Diego Pazó and Ernest Montbrió. Low-Dimensional Dynamics of Populations of Pulse-Coupled Oscillators. *Physical Review X*, 4(1):011009, jan 2014.
- [26] Wai Shing Lee, Edward Ott, and Thomas M Antonsen. Large coupled oscillator systems with heterogeneous interaction delays. *Physical review letters*, 103(4):044101, 2009.
- [27] JL Van Hemmen and WF Wreszinski. Lyapunov function for the kuramoto model of nonlinearly coupled oscillators. *Journal of Statistical Physics*, 72(1-2):145–166, 1993.
- [28] Tatsuya Uezu, Tomoyuki Kimoto, Shuji Kiyokawa, and Masato Okada. Correspondence between phase oscillator network and classical xy model with the same infinite-range interaction in statics. *Journal of the Physical Society of Japan*, 84(3):033001, 2015.
- [29] Dhagash Mehta, Noah S Daleo, Florian Dörfler, and Jonathan D Hauenstein. Algebraic geometrization of the kuramoto model: Equilibria and stability analysis. *Chaos: An Interdisciplinary Journal of Nonlinear Science*, 25(5):053103, 2015.
- [30] Francesca Collet and Wioletta Ruszel. Synchronization and spin-flop transitions for a mean-field xy model in random field. *Journal of Statistical Physics*, 164(3):645–666, 2016.
- [31] Kevin P O’Keefe, Hyunsuk Hong, and Steven H Strogatz. Oscillators that sync and swarm. *Nature Communications*, 8(1):1504, 2017.
- [32] Rodolphe Sepulchre, Derek Paley, and Naomi Leonard. Collective motion and oscillator synchronization. In *Cooperative control*, pages 189–205. Springer, 2005.
- [33] Amanda Chicoli and Derek A Paley. Probabilistic information transmission in a network of coupled oscillators reveals speed-accuracy trade-off in responding to threats. *Chaos: An Interdisciplinary Journal of Nonlinear Science*, 26(11):116311, 2016.
- [34] Sarthak Chandra, David Hathcock, Kimberly Crain, Thomas M Antonsen, Michelle Girvan, and Edward Ott. Modeling the network dynamics of pulse-coupled neurons. *Chaos: An Interdisciplinary Journal of Nonlinear Science*, 27(3):033102, 2017.
- [35] Sarthak Chandra, Michelle Girvan, and Edward Ott. Continuous versus discontinuous transitions in the d-dimensional generalized kuramoto model: Odd d is different. *Physical Review X*, 9(1):011002, 2019.
- [36] Sarthak Chandra and Edward Ott. Observing microscopic transitions from macroscopic bursts: Instability-mediated resetting in the incoherent regime of

- the d-dimensional generalized kuramoto model. *Chaos: An Interdisciplinary Journal of Nonlinear Science*, 29(3):033124, 2019.
- [37] Sarthak Chandra, Michelle Girvan, and Edward Ott. Complexity reduction ansatz for systems of interacting orientable agents: Beyond the kuramoto model. *Chaos: An Interdisciplinary Journal of Nonlinear Science*, 29(5):053107, 2019.
- [38] Donald C Michaels, Edward P Matyas, and Jose Jalife. Mechanisms of sinoatrial pacemaker synchronization: a new hypothesis. *Circulation Research*, 61(5):704–714, 1987.
- [39] Kurt Wiesenfeld, Pere Colet, and Steven H Strogatz. Frequency locking in josephson arrays: Connection with the kuramoto model. *Physical Review E*, 57(2):1563, 1998.
- [40] István Z. Kiss, Yumei Zhai, and John L. Hudson. Emerging Coherence in a Population of Chemical Oscillators. *Science*, 296(5573), 2002.
- [41] Leon Glass and Stuart A Kauffman. The logical analysis of continuous, nonlinear biochemical control networks. *Journal of Theoretical Biology*, 39(1):103–129, 1973.
- [42] Maximino Aldana and Philippe Cluzel. A natural class of robust networks. *Proceedings of the National Academy of Sciences*, 100(15):8710–8714, 2003.
- [43] Mahmoud M. Abdulrehem and Edward Ott. Low dimensional description of pedestrian-induced oscillation of the Millennium Bridge. *Chaos: An Interdisciplinary Journal of Nonlinear Science*, 19(1):013129, mar 2009.
- [44] Ernest Montbrió, Diego Pazó, and Alex Roxin. Macroscopic Description for Networks of Spiking Neurons. *Physical Review X*, 5(2):021028, jun 2015.
- [45] Carlo R Laing. Derivation of a neural field model from a network of theta neurons. *Physical Review E*, 90(1):010901, 2014.
- [46] Zhixin Lu, Kevin Klein-Cardena, Steven Lee, Thomas M Antonsen, Michelle Girvan, and Edward Ott. Resynchronization of circadian oscillators and the east-west asymmetry of jet-lag. *Chaos: An Interdisciplinary Journal of Nonlinear Science*, 26(9):094811, 2016.
- [47] Juan G Restrepo and Edward Ott. Mean-field theory of assortative networks of phase oscillators. *EPL (Europhysics Letters)*, 107(6):60006, 2014.
- [48] Erik Andreas Martens, E Barreto, SH Strogatz, E Ott, P So, and TM Antonsen. Exact results for the kuramoto model with a bimodal frequency distribution. *Physical Review E*, 79(2):026204, 2009.

- [49] Gilad Barlev, Thomas M Antonsen, and Edward Ott. The dynamics of network coupled phase oscillators: An ensemble approach. *Chaos*, 21(2):025103, 2011.
- [50] Per Sebastian Skardal, Juan G Restrepo, and Edward Ott. Frequency assortativity can induce chaos in oscillator networks. *Physical Review E*, 91(6):060902, 2015.
- [51] Diego Pazó and Ernest Montbrió. From quasiperiodic partial synchronization to collective chaos in populations of inhibitory neurons with delay. *Physical Review Letters*, 116(23):238101, 2016.
- [52] Javier Roulet and Gabriel B Mindlin. Average activity of excitatory and inhibitory neural populations. *Chaos: An Interdisciplinary Journal of Nonlinear Science*, 26(9):093104, 2016.
- [53] G Bard Ermentrout and Nancy Kopell. Parabolic bursting in an excitable system coupled with a slow oscillation. *SIAM Journal on Applied Mathematics*, 46(2):233–253, 1986.
- [54] Bard Ermentrout. Type i membranes, phase resetting curves, and synchrony. *Neural Computation*, 8(5):979–1001, 1996.
- [55] Eugene M Izhikevich. Class 1 neural excitability, conventional synapses, weakly connected networks, and mathematical foundations of pulse-coupled models. *IEEE Transactions on Neural Networks*, 10(3):499–507, 1999.
- [56] Alan L Hodgkin. The local electric changes associated with repetitive action in a non-medullated axon. *The Journal of Physiology*, 107(2):165, 1948.
- [57] Christoph Börgers and Nancy Kopell. Synchronization in networks of excitatory and inhibitory neurons with sparse, random connectivity. *Neural computation*, 15(3):509–538, 2003.
- [58] Mark EJ Newman. Assortative mixing in networks. *Physical review letters*, 89(20):208701, 2002.
- [59] Patric Hagmann, Leila Cammoun, Xavier Gigandet, Reto Meuli, Christopher J Honey, Van J Wedeen, and Olaf Sporns. Mapping the structural core of human cerebral cortex. *PLoS Biology*, 6(7):e159, 2008.
- [60] Stephan Bialonski and Klaus Lehnertz. Assortative mixing in functional brain networks during epileptic seizures. *Chaos*, 23(3):033139, 2013.
- [61] Elham Barzegaran, Amir Joudaki, Mahdi Jalili, Andrea O Rossetti, Richard S Frackowiak, and Maria G Knyazeva. Properties of functional brain networks correlate with frequency of psychogenic non-epileptic seizures. *Frontiers in Human Neuroscience*, 6, 2012.

- [62] Willem de Haan, Yolande AL Pijnenburg, Rob LM Strijers, Yolande van der Made, Wiesje M van der Flier, Philip Scheltens, and Cornelis J Stam. Functional neural network analysis in frontotemporal dementia and alzheimer’s disease using eeg and graph theory. *BMC Neuroscience*, 10(1):1, 2009.
- [63] Sara Teller, Clara Granell, Manlio De Domenico, Jordi Soriano, Sergio Gómez, and Alex Arenas. Emergence of assortative mixing between clusters of cultured neurons. *PLoS Computational Biology*, 10(9):e1003796, 2014.
- [64] Jacob G Foster, David V Foster, Peter Grassberger, and Maya Paczuski. Edge direction and the structure of networks. *Proceedings of the National Academy of Sciences*, 107(24):10815–10820, 2010.
- [65] Juan G Restrepo, Edward Ott, and Brian R Hunt. Approximating the largest eigenvalue of network adjacency matrices. *Physical Review E*, 76(5):056119, 2007.
- [66] LF Abbott and Carl van Vreeswijk. Asynchronous states in networks of pulse-coupled oscillators. *Physical Review E*, 48(2):1483, 1993.
- [67] D Hansel and G Mato. Existence and stability of persistent states in large neuronal networks. *Physical Review Letters*, 86(18):4175, 2001.
- [68] Arkady Pikovsky, Michael Rosenblum, and Jürgen Kurths. *Synchronization: a universal concept in nonlinear sciences*, volume 12. Cambridge university press, 2003.
- [69] Tamás Vicsek and Anna Zafeiris. Collective motion. *Physics Reports*, 517(3-4):71–140, 2012.
- [70] Nicholas A Christakis and James H Fowler. The collective dynamics of smoking in a large social network. *New England journal of medicine*, 358(21):2249–2258, 2008.
- [71] Reza Olfati-Saber. Swarms on Sphere: A Programmable Swarm with Synchronous Behaviors like Oscillator Networks. In *Proceedings of the 45th IEEE Conference on Decision and Control*, pages 5060–5066. IEEE, 2006.
- [72] Jiandong Zhu. Synchronization of Kuramoto model in a high-dimensional linear space. *Physics Letters A*, 377(41):2939–2943, dec 2013.
- [73] MA Lohe. Non-abelian kuramoto models and synchronization. *Journal of Physics A: Mathematical and Theoretical*, 42(39):395101, 2009.
- [74] Zhi-Ming Gu, Ming Zhao, Tao Zhou, Chen-Ping Zhu, and Bing-Hong Wang. Phase synchronization of non-abelian oscillators on small-world networks. *Physics Letters A*, 362(2-3):115–119, 2007.

- [75] H Eugene Stanley. Phase transitions and critical phenomena. *Clarendon, Oxford*, 9, 1971.
- [76] ML Mehta and N Rosenzweig. Distribution laws for the roots of a random antisymmetric hermitian matrix. *Nuclear Physics A*, 109(2):449–456, 1968.
- [77] John Buck and Elisabeth Buck. Synchronous fireflies. *Scientific American*, 234(5):74–85, 1976.
- [78] Bruno Eckhardt, Edward Ott, Steven H Strogatz, Daniel M Abrams, and Allan McRobie. Modeling walker synchronization on the millennium bridge. *Physical Review E*, 75(2):021110, 2007.
- [79] Nima Moshtagh and Ali Jadbabaie. Distributed Geodesic Control Laws for Flocking of Nonholonomic Agents. *IEEE Transactions on Automatic Control*, 52(4):681–686, apr 2007.
- [80] Jiandong Zhu, Jinhu Lu, and Xinghuo Yu. Flocking of Multi-Agent Non-Holonomic Systems With Proximity Graphs. *IEEE Transactions on Circuits and Systems I: Regular Papers*, 60(1):199–210, jan 2013.
- [81] Wei Wang and Jean-Jacques E Slotine. On partial contraction analysis for coupled nonlinear oscillators. *Biological Cybernetics*, 92:38–53, 2005.
- [82] Reza Olfati-Saber. Swarms on Sphere: A Programmable Swarm with Synchronous Behaviors like Oscillator Networks. In *Proceedings of the 45th IEEE Conference on Decision and Control*, pages 5060–5066. IEEE, 2006.
- [83] Steven H Strogatz and Renato E Mirollo. Stability of incoherence in a population of coupled oscillators. *Journal of Statistical Physics*, 63(3-4):613–635, 1991.
- [84] Jacques Faraut. *Analysis on Lie Groups: An Introduction*. Cambridge Studies in Advanced Mathematics. Cambridge University Press, 2008.
- [85] Shun Yamaguchi, Hiromi Isejima, Takuya Matsuo, Ryusuke Okura, Kazuhiro Yagita, Masaki Kobayashi, and Hitoshi Okamura. Synchronization of Cellular Clocks in the Suprachiasmatic Nucleus. *Science*, 302(5649), 2003.
- [86] Seung-Yeal Ha, Eunhee Jeong, and Moon-Jin Kang. Emergent behaviour of a generalized Viscek-type flocking model. *Nonlinearity*, 23(12):3139–3156, dec 2010.
- [87] Daniel M Abrams, Rennie Mirollo, Steven H Strogatz, and Daniel A Wiley. Solvable model for chimera states of coupled oscillators. *Physical review letters*, 101(8):084103, 2008.
- [88] Hidetsugu Sakaguchi and Yoshiki Kuramoto. A soluble active rotator model showing phase transitions via mutual entertainment. *Progress of Theoretical Physics*, 76(3):576–581, 1986.

- [89] Bertrand Ottino-Löffler and Steven H. Strogatz. Volcano transition in a solvable model of frustrated oscillators. *Phys. Rev. Lett.*, 120:264102, Jun 2018.
- [90] Jiandong Zhu. High-dimensional Kuramoto model limited on smooth curved surfaces. *Physics Letters A*, 378(18-19):1269–1280, mar 2014.
- [91] MA Lohe. Higher-dimensional generalizations of the watanabe–strogatz transform for vector models of synchronization. *Journal of Physics A: Mathematical and Theoretical*, 51(22):225101, 2018.
- [92] Takuma Tanaka. Solvable model of the collective motion of heterogeneous particles interacting on a sphere. *New Journal of Physics*, 16(2):023016, 2014.
- [93] Johan Markdahl and Jorge Goncalves. Global convergence properties of a consensus protocol on the n-sphere. In *Decision and Control (CDC), 2016 IEEE 55th Conference on*, pages 3487–3492. IEEE, 2016.
- [94] Wei Li and Mark W Spong. Unified cooperative control of multiple agents on a sphere for different spherical patterns. *IEEE Transactions on Automatic Control*, 59(5):1283–1289, 2014.
- [95] Ali Jadbabaie, Nader Motee, and Mauricio Barahona. On the stability of the kuramoto model of coupled nonlinear oscillators. In *American Control Conference, 2004. Proceedings of the 2004*, volume 5, pages 4296–4301. IEEE, 2004.
- [96] Alain Sarlette and Rodolphe Sepulchre. Consensus optimization on manifolds. *SIAM Journal on Control and Optimization*, 48(1):56–76, 2009.
- [97] Ernest Barreto, Brian Hunt, Edward Ott, and Paul So. Synchronization in networks of networks: The onset of coherent collective behavior in systems of interacting populations of heterogeneous oscillators. *Physical Review E*, 77(3):036107, 2008.
- [98] Ernest Montbrió, Jürgen Kurths, and Bernd Blasius. Synchronization of two interacting populations of oscillators. *Physical Review E*, 70(5):056125, 2004.
- [99] Shinya Watanabe and Steven H Strogatz. Integrability of a globally coupled oscillator array. *Physical review letters*, 70(16):2391, 1993.
- [100] Shinya Watanabe and Steven H Strogatz. Constants of motion for superconducting josephson arrays. *Physica D: Nonlinear Phenomena*, 74(3-4):197–253, 1994.
- [101] Arkady Pikovsky and Michael Rosenblum. Dynamics of heterogeneous oscillator ensembles in terms of collective variables. *Physica D: Nonlinear Phenomena*, 240(9-10):872–881, 2011.